



THE UNIVERSITY
of ADELAIDE

Faculty of Engineering, Computer and Mathematical Sciences
School of Mechanical Engineering

Performance of Petrodiesel and
Biodiesel Fuelled Engines:
A Fundamental Study of Physical and Chemical Effects

Author

Gary Cai

Supervisors

Prof. John Abraham

Prof. Bassam Dally

Dr. Zhao Tian

Dr. Emmanuel Motheau

28th January 2016

Acknowledgements

Firstly, I would like express my gratitude to my principal supervisor, Prof. John Abraham for his support, understanding, and guidance throughout my studies. His leadership and zeal is infectious, and it has spurred me forward.

I am thankful to Dr. Zhao Tian, Prof. Bassam Dally, and Mr. Yi Li for directing me onto this road of computational fluid dynamics. From working with Dr. Zhao Tian on the final year project, and internship under the tutelage of Mr. Yi Li on HVAC nozzles, my interest in CFD has grown day by day.

I am grateful for the support of my colleagues during my research. In particular, Xiao Chen, and Yinli Liu for their camaraderie and friendship.

I also want to thank the members of Prof. Abraham's research group at Purdue University, especially May Yen, for their support and help in my work, and their hospitality during my visit to Purdue in mid-2014 as a visiting scholar.

My family, especially my parents, have been of superb support, not only during my research. They have guided me throughout my life with correct morals and right principles, and made me who I am now.

I would like to express my gratitude for the support given by the School of Mechanical Engineering at the University of Adelaide. In particular, I thank Prof. Anthony Zander, Billy Constantine, Sophie Chen and Fei Gao.

Finally, but definitely not last, I thank my Patient Wife™, Chengyu Chang, for her love and support. She has been my inspiration and I love her greatly.

Table of Contents

Nomenclature	ix
Abstract	xiv
Declaration of Originality	xv
1 Introduction	1
1.1 Objectives.....	8
1.2 Thesis Outline	8
2 Literature Review	10
2.1 Introduction.....	10
2.2 Non-reacting/Reacting Diesel Jets	10
2.3 Modelling of Petrodiesel and Biodiesel	14
2.3.1 <i>Surrogates for Petrodiesel</i>	15
2.3.2 <i>Surrogates for Biodiesel</i>	16
2.4 Pollutant Formation Pathways	18
2.4.1 <i>NO</i>	18
2.4.2 <i>Soot</i>	20
2.5 Biodiesel Fuel Research.....	26
2.6 Summary	31
3 Computational Methods	32
3.1 Introduction.....	32
3.2 Flamelet Model	32
3.2.1 <i>Theory</i>	32
3.2.2 <i>Governing Equations</i>	33
3.3 Multi-Dimensional Engine Model	36
3.3.1 <i>Gas-phase Governing Equations</i>	37
3.3.2 <i>Turbulence Model</i>	39
3.3.3 <i>Turbulence-Flame Interaction Model</i>	39
3.3.4 <i>Pollutant Modelling</i>	40
3.3.5 <i>Residence Time Tracking</i>	41
4 Biodiesel Feedstock Effects on Spray Structure	42
4.1 Introduction.....	42
4.2 Feedstock Selection.....	42
4.2.1 <i>Molar Mass, Critical Temperature, and Specific Heat</i>	43

4.2.2	<i>Vapour Pressure</i>	44
4.2.3	<i>Thermal conductivity</i>	45
4.2.4	<i>Liquid Density</i>	45
4.2.5	<i>Viscosity</i>	46
4.2.6	<i>Surface Tension</i>	46
4.2.7	<i>Sauter Mean Diameter</i>	47
4.3	Results and Discussion.....	47
4.3.1	<i>Liquid-phase Penetration</i>	47
4.3.2	<i>Gas-phase Penetration</i>	51
4.3.3	<i>Mixture Fraction Distribution</i>	52
4.4	Summary	53
5	Limit Phenomena	55
5.1	Introduction	55
5.2	Background	55
5.3	Influence of Strain on Pollutants.....	57
5.4	Summary and Conclusions.....	61
6	Soot Formation Reaction Pathway Analysis	63
6.1	Introduction	63
6.2	304-Species TBS Mechanism	63
6.3	Reaction Pathway Analysis.....	65
6.4	Summary and Conclusions.....	70
7	Two-Equation Soot Model Formulation	71
7.1	Introduction	71
7.2	General Formulation of Two-Equation Soot Models.....	71
7.3	Computational Method.....	72
7.4	The Proposed Two Equation Soot Model	75
7.4.1	<i>Soot Inception</i>	76
7.4.2	<i>Surface Growth</i>	76
7.4.3	<i>Coagulation</i>	77
7.4.4	<i>Oxidation by O₂</i>	77
7.4.5	<i>Oxidation by OH</i>	78
7.5	Sensitivity Analysis of the Model	78
7.5.1	<i>Addressing Soot Oxidation in Lean Mixtures</i>	81
7.6	Conclusion and Summary	84

8	Modelling Diesel Sprays with Two-Equation Soot Model	85
8.1	Introduction	85
8.2	Computational Conditions	85
8.3	Other Soot Models Considered	86
8.3.1	<i>Leung et al Two-Equation Soot Model</i>	86
8.3.2	<i>Kinetics-based Soot Model</i>	87
8.4	Results and Discussion.....	88
8.5	Summary and Conclusions.....	91
9	Biodiesel and Diesel Sprays	93
9.1	Introduction	93
9.2	Computational Conditions	93
9.3	Results and Discussion.....	94
9.4	Reacting Jet	97
9.5	Summary and Conclusions.....	99
10	Summary, Conclusions, and Future Work	101
10.1	Summary and Conclusions	101
10.2	Future Work	104
	References.....	106
	Appendix A: Combustion Characteristics of Surrogate Fuels	120
	Appendix B: Extra Species in the 304-Species TBS Mechanism.....	124
	Biography	125
	List of Publications	126

List of Tables

Table 1.1: Properties of #2 diesel compared with those of biodiesel.	5
Table 1.2: Fatty acid methyl ester composition of biodiesel fuels (Goering, 1982). Given in weight %	6
Table 4.1: Each of the seven feedstocks approximated (weight %) to be consisting of the three major FAMES.	44
Table 4.2: Some of the properties employed in the spray calculations.	50
Table 5.1: Ignition and extinction limits for the fuel surrogates.	57
Table 5.2: Soot formation characteristics for HEP253, TBS214 and TBS304.....	60
Table 5.3: NO formation characteristics for HEP253, TBS214 and TBS304.	61
Table 6.1: Reaction pathway analysis for the formation of A1	69
Table 7.1: Values of constants selected for sensitivity study.	78
Table 7.2: Model constants.....	83
Table 8.1: Computational conditions for the n-heptane spray. Parameter changed in each case in bold and underlined.	86
Table 9.1: Constant-volume chamber conditions for the reacting jet study.	94
Table A.1: Adiabatic flame temperature (K) at 1 atm for reactant temperature of 298 K. ...	120
Table A.2: Adiabatic flame temperature (K) at 40 atm for reactant temperature of 1000 K.	121

List of Figures

Figure 1.1: World crude oil consumption compared to production (EIA, 2013).	1
Figure 1.2: Extraction of various fuels from crude oil (Chevron, 1998).	2
Figure 1.3: World crude oil consumption by sector (IEA, 2014).	3
Figure 1.4: World transportation consumption based on fuel (EIA, 2012).	3
Figure 1.5: Transesterification process of a vegetable oil feedstock to biodiesel.	4
Figure 1.6: Chemical structure of oleic acid, $C_{18}H_{34}O_2$	4
Figure 2.1: Conceptual drawing of a non-reacting diesel spray	11
Figure 2.2: Non-dimensional axial penetration with respect to non-dimensional time for vaporising and non-vaporising sprays at different ambient densities (Bajaj et al., 2011).	12
Figure 2.3: Ignition and extinction S-curve.	13
Figure 2.4: Conceptual illustration of a combustng diesel-jet (Dec, 1997).	14
Figure 2.5: PAH build-up via the hydrogen-abstraction carbon-addition mechanism (Frenklach and Wang, 1994).	20
Figure 2.6: Stages of soot formation and growth (Bockhorn, 1994).	21
Figure 2.7: Simulated and measured PAH concentration of a turbulent flame (Kohler et al., 2012).	26
Figure 2.8: Primary oxidation pathway of a typical biodiesel fuel (Herbinet et al., 2008).	27
Figure 3.1: Conceptual illustration of flamelets.	33
Figure 3.2: Conceptual drawing of diffusion flamelets.	35
Figure 3.3: Computational grid used in REC.	37
Figure 4.1: Biodiesel production by region.	42
Figure 4.2: Critical Temperature (K) with respect to FAME chain length (Sales-Cruz et al., 2010).	43
Figure 4.3: Log-scale vapour pressure (kPa) with respect to $(1/T)$. Data taken from Yuan and Hansen (2005).	44
Figure 4.4: Thermal conductivity for FAMEs plotted against temperature (Annaken, 2011).	45
Figure 4.5: Liquid density of FAMEs with respect to temperature (Annaken, 2011).	45
Figure 4.6: Dynamic viscosity of FAMEs with respect to temperature (Annaken, 2011).	46
Figure 4.7: Surface tension of each FAME with respect to temperature (Annaken, 2011).	47
Figure 4.8: Liquid penetration of the biodiesel fuels and the soybean-derived biodiesel measurement from Nerva et al. (2012). Ambient temperature of 900 K (a) above, 1000 K (b) below.	48

Figure 4.9: Vapour pressure of the biodiesel fuels. Vertical axis is in log-scale. Temperature equivalent ranges from 373.15 K to 3073.15 K. Vapour pressure (kPa) at selected temperatures (K) shown in the inset table, along with the mean and standard deviation.	50
Figure 4.10: Vapour penetration of the biodiesel fuels compared to the soybean-derived measurement from Nerva et al. (2012) and an analytical curve.	52
Figure 4.11: Mixture fraction contours of the biodiesel fuels at 4 ms after the start of injection. 900 K cases (a) above and 1000 K cases (b) below. Feedstocks: castor, corn, palm, rapeseed, soybean, sunflower and tallow represented by (1) to (7). Lower cut-off fo.....	53
Figure 5.1: Temperature evolution of a diesel surrogate, n-heptane, at (a) χ of 59 s^{-1} , and (b) χ of 1542 s^{-1}	56
Figure 5.2: Soot volume fraction rising continuously over time for the petrodiesel surrogate mechanism at a χ of 5 s^{-1}	58
Figure 5.3: Soot volume fraction at various χ for a) HEP253, and b) TBS214.	59
Figure 5.4: NO species concentration at various strain rates for a) HEP253 and b) TBS214.	61
Figure 6.1: Creation of a 214-species biodiesel mechanism.	64
Figure 6.2: Time evolution of soot volume fraction for TBS 214 and TBS304.	64
Figure 6.3: a) Soot volume fraction and b) NO concentration for the three fuel surrogates. ...	65
Figure 6.4: C ₂ H ₂ concentration for the three fuel surrogate mechanisms.	66
Figure 6.5: A1 concentration for the three fuel surrogate mechanisms.	66
Figure 6.6: Plots for temperature, soot volume fraction, and acetylene, A4 and A1 mass fraction.	67
Figure 6.7: Reaction pathway of critical species that affects the formation of A1.	70
Figure 7.1: Volume fraction of soot (a), and mass fraction of (b) A1, (c) C ₂ H ₂ , (d) C ₂ H ₃ in the diffusion flame.	74
Figure 7.2: Predicted soot volume fraction for varying values of $L\alpha_1$, $E\alpha_1$, $L\alpha_2$, $E\alpha_2$, $L\alpha_3$ and $L\alpha_4$ as listed in Table 2 are shown in (a)-(f), respectively. The line types are identified in (a).	79
Figure 7.3: Predicted soot volume fractions with the preliminary set of constants in the two-equation model compared with the predictions of the ABF model.	81
Figure 7.4: Soot volume fraction when (a) $L\alpha_3$ is increased for the diesel surrogate, (b) $L\alpha_2$ increased with a constant $L\alpha_3$, and (c) $L\alpha_4$ increased with a constant $L\alpha_2$ and $L\alpha_3$. (a2), (b2) and (c2) show zoomed region of $Z = 0 - 0.15$	82
Figure 7.5: Soot volume fraction predicted by the two-equation soot model compared to the ABF soot model for χ_{st} of a) 5/s and b) 10/s.	83

Figure 8.1: Temperature contours for the nine cases at 4 ms ASI with (a) – (i) representing Cases 1 – 9, respectively.....	89
Figure 8.2: Soot volume fraction contour for the nine cases at 4 ms ASI.....	89
Figure 8.3: Soot volume fraction with respect to axial distance at the centreline for Cases 1, 5, 6, and 9 at 4 ms ASI with (a) - (d) representing them, respectively. Soot is normalised in each case independently.....	90
Figure 8.4: Soot volume fraction comparison between measured data (a), ABF kinetics soot mechanism (b), CYA soot model (c), LLJ soot model (d). Cases 1, 5, 6, 7 and 9 are compared. Measured data is from Engine Combustion Network (www.sandia.gov/ecn/).	92
Figure 9.1: Non-reacting and reacting liquid penetration plotted against time. 900 K ambient (a,b) and 1000 K ambient (c,d). Non-reacting (a,c), reacting (b,d).	95
Figure 9.2: Spray penetration as a function of time when the spray tip is identified as the location where the mixture fraction is (a) 0.0025, and (b) 1E-6.	96
Figure 9.3: Mixture fraction contour plots of the computed non-reacting jets. Ambient temperature of 900 K is plotted above (a,b) and 1000 K below (c,d). Biodiesel cases left, diesel cases right. Stoichiometric mixture fraction is emphasised by thick line. Contour ranges from 0.0025 – 0.1.	97
Figure 9.4: Temperature contour plots of the computed reacting jets. Ambient temperature of 900 K is plotted above (a,b) and 1000 K below (c,d). Biodiesel cases left, diesel cases right. Temperature ranges from 1,900 – 2,300 K.....	98
Figure 9.5: Soot volume fraction contour plots of the computed reacting jets. Ambient temperature of 900 K is plotted above (a,b) and 1000 K below (c,d). Biodiesel cases left, diesel cases right.	98
Figure 9.6: Predicted (a) soot volume fraction compared to measured data (b). Proceeding downwards, sprays are: 1000 K diesel, 1000 K biodiesel, 900 K diesel, 900 K biodiesel. Measured data taken from work of Nerva et al. (2012).....	99
Figure A.1: Adiabatic flame temperature (K) at 1 atm and initial temperature of 298 K.	121
Figure A.2: Adiabatic flame temperature (K) at 40 atm and initial temperature of 1000 K. .	121
Figure A.3: S_L (cm/s) of the diesel and biodiesel fuel surrogates with respect to ϕ at 1 atm and initial temperature of 298 K.....	122
Figure A.4. S_L (cm/s) of the diesel and biodiesel fuel surrogates with respect to ϕ at 40 atm and initial temperature of 1000 K.....	123

Nomenclature

Upper-Case Roman

A, B, C	Variable in Antoine equation
C	Progress variable
C_{st}	Progress variable at stoichiometric
$C_{\epsilon 1}, C_{\epsilon 2}, C_{\mu}$	k – ϵ turbulence model constant
C_{χ}	Average scalar dissipation rate constant
D	Mass diffusivity
Da	Damköhler number
D_e	Effective diffusivity
E	Extinction limit
E_a	Activation energy
E_{a1}, E_{a2}	Semi-empirical soot model sub-model exponential terms
I	Ignition limit
K_A, K_B, K_T, K_Z	Nagle and Strickland-Constable oxidation sub-model constant
L	Characteristic length
$L_{a1} \dots L_{a4}$	Semi-empirical soot model sub-model linear terms
M_1	First soot moment
$M_{c(s)}$	Molecular weight of carbon atom
N	Soot number density
N_j	Soot number density for j particles
P	Pressure
P_{H_2O}	Partial pressure of water
P_{O_2}	Partial pressure of oxygen
P_{OH}	Partial pressure of hydroxide
P_v	Vapour pressure
R	Universal gas constant
$R_1 \dots R_5$	Leung et al. (1995) semi-empirical soot model source terms
S	Soot surface area
T	Local temperature
T_a	Adiabatic flame temperature
T_c	Critical temperature
T_u	Unburnt fuel temperature
V_u	Volume of domain

W_{C_2}	Molecular weight of C_2
Y_F	Mass fraction of fuel species
Y_i	Mass fraction of species, i
Y_{N_2}	Mass fraction of nitrogen
Y_{O_2}	Mass fraction of oxygen
Z	Mixture fraction
Z_F	Mass fraction of all elements from fuel stream
Z_i	Mixture fraction of species, i
Z_O	Mass fraction of all elements from oxidiser stream
Z_{st}	Stoichiometric mixture fraction
\tilde{Z}''^2	Variance of mixture fraction

Lower-Case Roman

c_p	Specific heat capacity of species, i
c	Specific heat
d	Nozzle diameter
d_c	Mean soot diameter
f_m	Mass fraction
f_v	Soot volume fraction
h_g	Total gas-phase enthalpy per unit mass
h_i	Specific enthalpy of species, i
j_{ia}	Diffusion mass flux of species, i
k	Thermal conductivity
k	Turbulent kinetic energy
m_f	Mass of soot formed
m_{fi}	Mass of fuel burnt
m_j	Soot particle mass of j particles
m_{lt}	Mass of liquid fuel in domain
m_o	Mass of soot oxidised
m_s	Overall mass of soot
\dot{q}_R	Power lost by radiation
t	Time
\mathbf{u}	Reynolds-averaged mean gas-phase velocity vector
\dot{w}_i	Chemical kinetic source term

Upper-Case Greek

α	Fenimore and Jones oxidation rate parameter
ΔP	Injection pressure
ϕ	Scalar variable

Lower-Case Greek

$\alpha_1 \dots \alpha_4$	Semi-empirical soot equation mass source terms
β_1, β_2	Semi-empirical soot equation number source terms
γ	Surface tension
λ_e	Effective thermal conductivity
λ_i	Thermal conductivity of species, i
λ_l	Laminar thermal conductivity
λ_t	Turbulent thermal conductivity
μ_e	Effective viscosity
μ_l	Laminar viscosity
μ_t	Turbulent viscosity
ν	Kinematic viscosity
ν_F	Reaction coefficients of fuel species
ν_{N_2}	Reaction coefficients of nitrogen
ν_{O_2}	Reaction coefficients of oxygen
ν_T	Turbulent viscosity
ρ	Density
ρ_a	Ambient density
$\rho_{c(s)}$	Soot density
ρ_g	Gas-phase density
ρ_i	Partial density of species, i
ρ_l	Fuel density
ρy_s	Species density of soot
$\sigma_k, \sigma_\epsilon$	k – ϵ turbulence model constant
τ	Turbulent stress tensor
χ	Scalar dissipation rate
χ_{ext}	Extinction scalar dissipation rate

χ_{ign}	Ignition scalar dissipation rate
$\tilde{\chi}$	Average scalar dissipation rate
ω	Angular velocity
$\tilde{\omega}_\varphi$	Fávre-averaged source terms
$\dot{\omega}_\varphi$	Instantaneous source terms

Symbols

erf	Error function
-------	----------------

Abbreviations

<i>A1</i>	Benzene
<i>A2</i>	Naphthalene
<i>A3</i>	Phenanthrene
<i>A4</i>	Pyrene
<i>ASI</i>	After start of injection
<i>CI</i>	Compression-ignition
<i>CYA</i>	Cai, Yen and Abraham
<i>DLFC</i>	Diffusion Laminar Flamelet Code
<i>EIA</i>	U.S. Energy Information Administration
<i>FAME</i>	Fatty acid methyl ester
<i>HACA</i>	Hydrogen-abstraction carbon-addition
<i>HEP</i>	Heptane
<i>JSR</i>	Jet-stirred reactor
<i>LHV</i>	Lower heating value
<i>LLJ</i>	Leung, Lindstedt, and Jones
<i>LLNL</i>	Lawrence Livermore National Laboratory
<i>MB</i>	Methyl butanoate
<i>MD</i>	Methyl decanoate
<i>MD9D</i>	Methyl-9-decenoate
<i>OppDif</i>	Opposed-flow diffusion flame
<i>PAH</i>	Polycyclic aromatic hydrocarbons
<i>PDF</i>	Probability density function
<i>PPM</i>	Parts per million
<i>PSR</i>	Perfectly-stirred reactor

<i>RANS</i>	Reynolds-averaged Navier-Stokes
<i>REC</i>	Reciprocating Engine Code
<i>RXN</i>	Reaction
<i>SMD</i>	Sauter-mean diameter
<i>TBS</i>	Ternary biodiesel surrogate

Abstract

In this work, biodiesel and petrodiesel combustion is studied under conditions that represent those in an engine at top-dead-centre. The primary focus of this study is on improving the understanding of biodiesel feedstock properties on spray structure, understanding the effect of strain on soot formation in biodiesel and petrodiesel combustion using a kinetics-based soot model, developing a simplified soot model that can model soot formation in both biodiesel and petrodiesel combustion, and applying the model to study soot formation in sprays. The differences in feedstock properties primarily affect the liquid phase penetration. It is shown that liquid penetration is influenced by entrainment rate, vapour pressure, and the average droplet size, in decreasing order of influence. The vapour-phase penetration and mixture fraction distribution in the sprays are not significantly influenced by the changes in feedstock properties.

Kinetic mechanisms for the oxidation of surrogate fuels for biodiesel and diesel and for soot formation are employed in the study. A one-dimensional flamelet code is employed to investigate the response of the soot formation to changes in scalar dissipation rate. The soot formation in biodiesel combustion is found to be more sensitive to changes in scalar dissipation rate. This suggests that increasing turbulence in a biodiesel-fuelled engine is likely to have a greater impact on soot emissions than in a petrodiesel-fuelled engine. Through a reaction pathway analysis, it is found that the differences in soot are on account of differences in the concentration of the aromatic species. Critical kinetic pathways and important species responsible for soot formation are identified for the fuels.

Having identified the critical species and pathways, a semi-empirical two-equation soot model is developed to model soot in both hydrocarbon diesel and biodiesel combustion. Results from the kinetic soot formation model are employed to calibrate the constants of the semi-empirical model. To the best knowledge of the author, this is the first soot model formulated that can model soot formation in the combustion of both fuels. The semi-empirical model is implemented in an in-house Reynolds-averaged Navier Stokes (RANS) multi-dimensional spray code and employed to predict soot in biodiesel and diesel sprays. The computed spray results are compared with available measurements in the literature. Compared to the performance of another well-validated semi-empirical two-equation soot model, the soot model developed in this work is shown to better predict soot in both biodiesel and diesel sprays.

Declaration of Originality

This work contains no material which has been accepted for the award of any other degree or diploma in any university or other tertiary institution to Gary Cai. To the best of my knowledge and belief, contains no material previously published or written by another person, except where due reference has been made in the text.

I give consent to this copy of my thesis, when deposited in the University Library, being made available for loan and photocopying, subject to the provisions of the Copyright Act 1968. I also give permission for the digital version of my thesis to be made available on the web, via the University's digital research repository, the Library catalogue, the Australasian Digital Theses program (ADTP) and also through web search engines.

Signed

Gary Cai

1 Introduction

Ever since the start of the industrial era, the world population has been increasingly dependent on crude oil. In addition to the use of crude oil for energy production, humans are reliant on it for many other uses, such as: production of plastics, lubricants, household goods. In fact, it is hard to imagine the modern world without crude oil. This ever increasing demand is not only due to the increasing world population, but also from an increased access of a larger proportion of the populace to products that require crude oil. It has been predicted that half of the global demand for crude oil will come from China alone (IEA, 2015) within the next five years, and this demand is projected to continue into the year 2040. Figure 1.1 shows the worldwide production rate of crude oil compared to consumption. It has been suggested that peak crude oil extraction has been surpassed (Hirsch, 2006), but new supplies are being identified all the time, and fracking, especially in the USA, has dramatically increased oil supply (Chew, 2014; White et al., 2014). Hence, the thinking that peak oil has been reached is largely discredited. In fact, as this thesis is being written, oil prices continue to plunge on world markets because of oversupply.

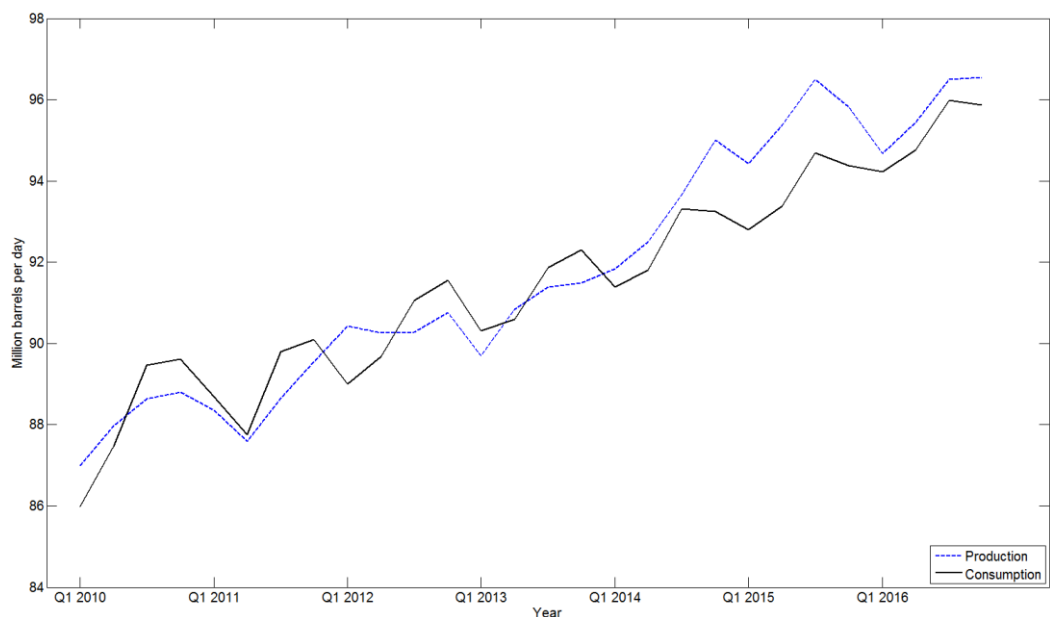


Figure 1.1: World crude oil consumption compared to production (EIA, 2013).

Traditionally, petrodiesel fuel is produced via fractional distillation of crude oil (Chevron, 2007). As the crude oil is sent to a distillation column and heated, different fuels are extracted. The lighter fuels such as propane and butane are extracted from the top, and progressively denser fuels, such as gasoline and petrodiesel, are extracted from lower down the column. Many processes take place to extract, purify, and optimise the oil to meet government emissions standards (Chevron, 2007). Figure 1.2 shows an example of this complex process.

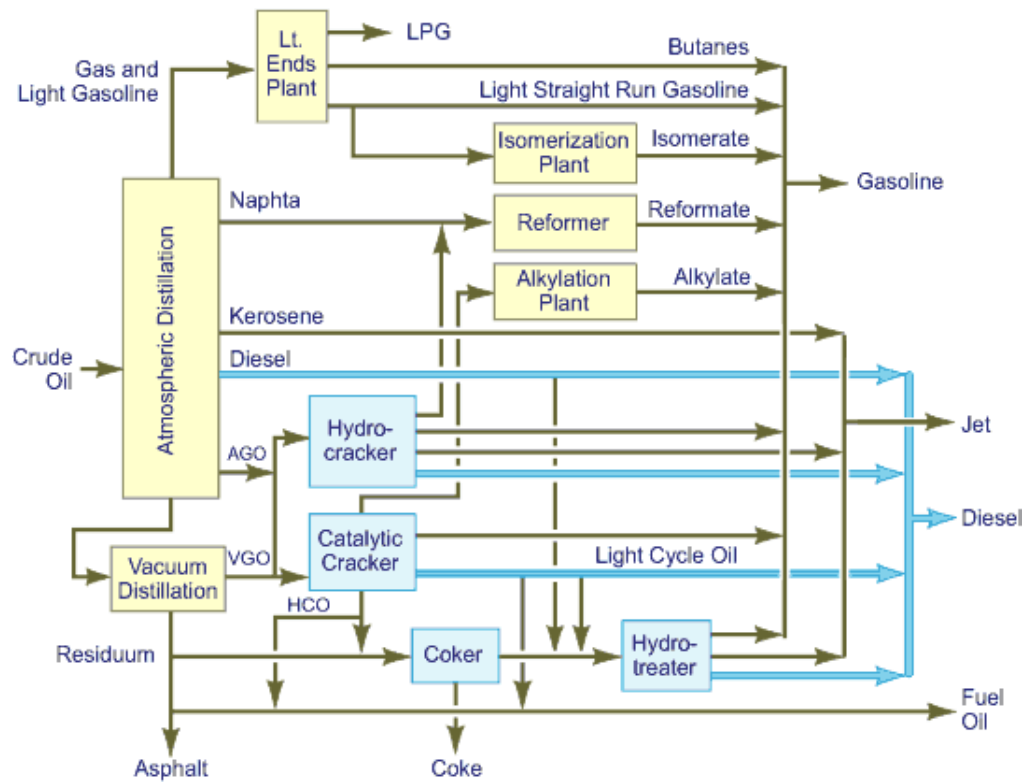


Figure 1.2: Extraction of various fuels from crude oil (Chevron, 1998).

Even if the supply of oil keeps up with demand, the reliance on crude oil has come at a cost to the natural environment and human health. In addition to the increased air pollution from the burning of petroleum products, the production of crude oil has had a negative impact on natural landscape and wildlife habitats (EoE, 2010), either by clearing land for extraction sites, or by greenhouse gases trapping increasing amounts of energy, causing the climate shift. (Pacala and Socolow, 2004). The unanticipated effects of increased crude oil consumption are numerous. Polluting emissions such as nitric oxides and particulate matter have been shown to cause serious health issues (Speizer et al., 1980; Scheepers and Vermeulen, 2012). The warming of the climate increases the sea level through the release of frozen water, causing a serious risk to the lives of people in island nations, or lands which lie below the water belt, such as the Netherlands (MoI and E, 2015). In addition, the warming of oceans increases its acidity through trapped CO₂, causing distress to water-based life, which may in turn, affect the human food chain (Cheung et al., 2010).

As a direct response to the gradual reduction in supply, increase in demand, and harmful by-products of crude oil, governments are responding by seeking viable alternatives. Figure 1.3 shows the global crude oil consumption in 2012, broken down by sector. Clearly, much of the consumption of crude oil is in the transportation sector. Figure 1.4 shows the breakdown of consumption by fuels derived from crude oil. It can be seen that petroleum and diesel fuel are the two widely used fuels. This is followed by jet fuel used in aircraft. This should come as no

surprise; gasoline and diesel fuel are two most commonly used fuels for road transportation. Targeting a reduction in crude oil usage, by reducing gasoline and diesel fuel use, would have the greatest positive effect.

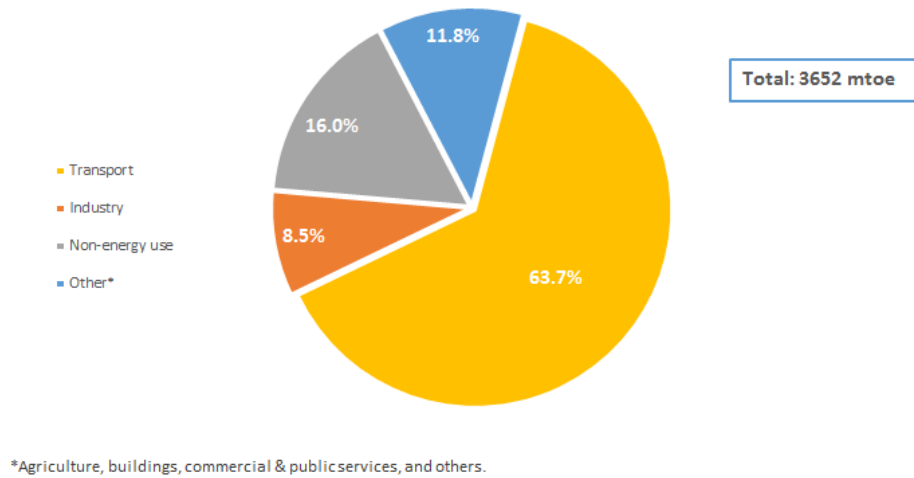


Figure 1.3: World crude oil consumption by sector (IEA, 2014).

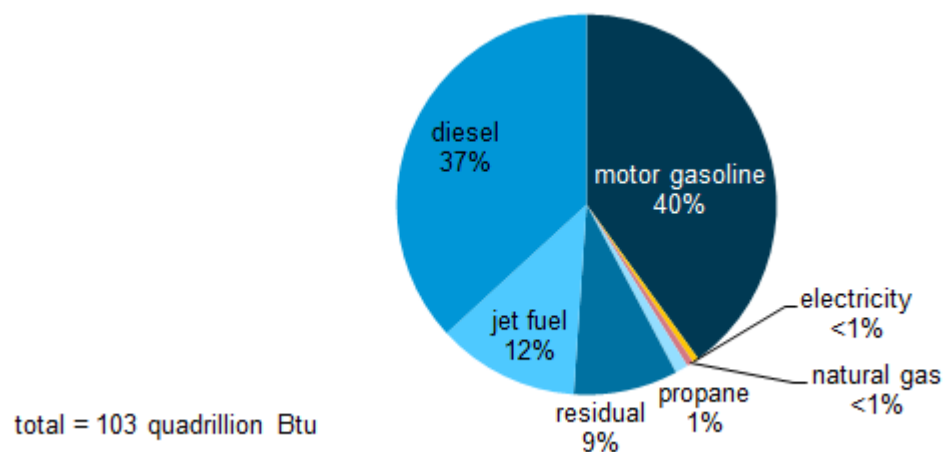


Figure 1.4: World transportation consumption based on fuel (EIA, 2012).

While there have been many alternative power sources proposed for road transportation, such as hydrogen fuel cells and electrical batteries, they do not generally meet the basic requirements of modern road transportation. These requirements include:

1. Having an energy density similar to current petro-based fuels (this affects the range of the vehicle),
2. the ability to recharge the on-board storage to full capacity quickly,
3. and an infrastructure to be economically viable.

The energy sources mentioned above do not meet all of the requirements. Hydrogen fuel cells, lack the infrastructure and has low energy density, and electrical batteries have low energy density and cannot be recharged quickly. These sources can only be stop-gap solutions. However, there is an attractive fuel that can replace petrodiesel fuel with little modification to the current technology and infrastructure: biodiesel.

As can be inferred from its name, biodiesel is made of bio-organic material. Although ‘diesel’ is in the name, there is no petrodiesel fuel component in biodiesel. Rather, biodiesel is a type of biofuel that can be produced from various feedstocks such as vegetable oils, waste cooking oil, beef tallow, and even algae. The vegetable oils themselves are not suitable as a replacement for petrodiesel due to their higher viscosity (Demirbas, 2002). Thus, the feedstocks have to undergo a chemical process called transesterification (Demirbas, 2002). This process is illustrated in Figure 1.5 for a vegetable oil. The triglyceride is extracted from the feedstock and each mole is reacted with three moles of alcohol, usually methanol, with the aid of a catalyst. This forms glycerol and three moles of the resulting fatty acid methyl ester (FAME).

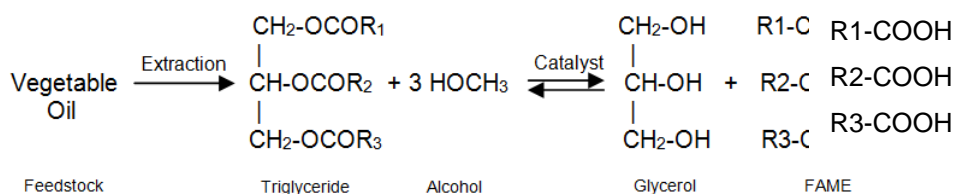


Figure 1.5: Transesterification process of a vegetable oil feedstock to biodiesel.

It is the FAMES that make up biodiesel fuel. A commonly seen FAME, oleic acid ($\text{C}_{18}\text{H}_{34}\text{O}_2$), is shown in Figure 1.6. All FAMES that make up biodiesel fuels contain the R-COOH subgroup, shown in the dashed circle. This subgroup is the differentiating factor between biodiesel and typical petrodiesel. Unlike petrodiesel which consist of hydrocarbons, biodiesel is an oxygenated fuel.

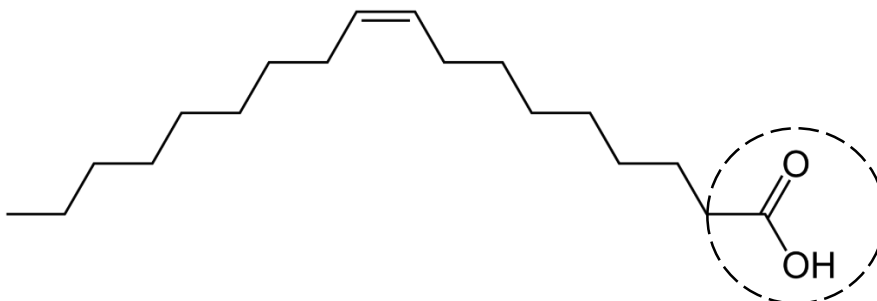


Figure 1.6: Chemical structure of oleic acid, $\text{C}_{18}\text{H}_{34}\text{O}_2$.

Depending on the feedstock from which the biodiesel fuel is sourced, the fuel will have different properties due to the different lipid chain lengths that make up each feedstock. For

example, biodiesel derived from coconut oil will have different properties from that derived from corn oil. Table 1.1 shows the FAME composition of biodiesels based on their feedstock source. Each feedstock results in different proportions and combinations of FAMES. In Table 1.1, oleic acid is also referred to as C18:1 as it has 18 carbon atoms and 1 double bond. As can be seen, castor-derived biodiesel consists of mostly oleic acid, whereas palm-derived biodiesel has a majority of palmitic and oleic acid. Table 1.2 summarises the physical properties of soy-derived biodiesel compared to #2 petrodiesel.

From Table 1.2, it can be seen that most properties, other than viscosity, of biodiesel are similar to those of #2 diesel. This makes biodiesel suitable as a replacement fuel for conventional petrodiesel. The significantly higher viscosity of biodiesel will lead to larger drops, for example. This may affect the combustion characteristics of biodiesel when compared to diesel. Biodiesel can substitute diesel fuel in current diesel engines without any engine modification. In addition to fulfilling the three requirements listed above, this means biodiesel can easily replace petrodiesel fuel. Overall, biodiesel has many attractive properties. Compared to conventional petrodiesel, it has lower particulate matter and aldehyde emissions (Peng et al., 2007) when used in a diesel engine. Due to its production from organic matter, biodiesel production can reduce carbon emissions on a life-cycle basis. When grown locally, biodiesel can increase the national energy security. This is balanced out by a slight increase in NOx emissions. Overall, biodiesel fully satisfies the three requirements needed by alternative fuels for use in the transportation sector.

Table 1.1: Properties of #2 diesel compared with those of biodiesel.

Parameter	#2 Diesel	Soy-derived Biodiesel
Density at 288 K (kg.m ⁻³)	843	877
Density expected @ 373 K (kg.m ⁻³)	766	823
Kinematic viscosity at 313 K (mm ² .s ⁻¹)	2.35	3.98
Lower heating value (MJ.kg ⁻¹)	43.0	37.4
C/H and C/O mass ratios	6.53 and ∞	6.48 and 7.05
Cetane number	46	51
Z _{st} (21% O ₂)	0.063	0.08

Table 1.2: Fatty acid methyl ester composition of biodiesel fuels (Goering, 1982). Given in weight %.

	Lauric C12:0	Myristic C14:0	Palmitic C16:0	Palmitoleic C16:1	Stearic C18:0	Oleic C18:1	Linoleic C18:2	Linolenic C18:3	Arachidic C20:0	Gondoic C20:1	Behenic C22:0	Erucic C22:1	Lignoceric C24:0
Castor	-	-	1.38	-	1.11	91.42	4.84	0.56	0.25	0.42	-	-	-
Corn	-	-	11.81	0.12	2.13	27.35	57.74	0.63	0.34	0.33	-	-	0.14
Palm	0.37	1.13	42.39	0.17	4.2	40.91	9.97	0.29	0.29	0.16	-	-	0.05
Rapeseed	-	0.04	4.07	0.23	1.55	62.24	20.61	8.72	0.87	1.09	0.27	0.71	-
Soybean	0.08	0.12	11.44	0.16	4.14	23.47	53.46	6.64	0.33	0.22	0.27	0.07	0.13
Sunflower	-	0.04	6.26	0.06	3.93	20.77	67.75	0.15	0.23	0.13	0.7	-	0.26

Due to the attractive properties, environmentally-friendly production cycle, and ease of introduction into the current transportation infrastructure, biodiesel fuel is being actively researched in the scientific community. There are numerous experimental studies investigating biodiesel emissions (Wu et al., 2011; Zhang and Fang, 2011; Nerva et al., 2012) and many that model biodiesel sprays in engines (Wang et al., 2010; Som et al., 2010; Mancaruso et al., 2011; Chen et al., 2013). However, there are inconsistencies between studies. For example, it is not clear if the NO_x increases or decreases from biodiesel engines (Mueller et al., 2009). It is important to recognise three important factors:

1. The different studies are carried out in different engine types, such as road, marine, locomotive and even industrial engines. This changes other variables that would affect the performance/emissions characteristics of biodiesel.
2. In addition, many variables are inter-connected, making it hard to interpret results. Even if these differences did not exist, the phasing of ignition and combustion with volume change are not maintained constant between studies.
3. Finally, as pointed out above, there is a difference in the properties between biodiesel fuels from different feedstocks. The difficulty in interpreting engine test data at a fundamental level have motivated researchers to measure spray combustion characteristics in optically-accessible constant-volume chamber (Genzale et al., 2010; Wang et al., 2010; Nerva et al., 2012).

Engine optimization is still dependent on cut-and-try experimental tests. In recent years, however, multi-dimensional modelling of the fluid flow, sprays, and combustion in engines has reduced the extent of testing. Modelling has many benefits. For example, parameters in multi-dimensional models can be altered easily, as compared to measurements, such as nozzle diameter and ambient O_2 mole fraction. Effects of their changes can be quickly studied. Alternatively, modelling has the ability to isolate spray/combustion characteristics. The ability of multidimensional engine models to help the engine designer is dependent on the accuracy of the sub-models that are employed. While significant effort has been put into developing models for petrodiesel engines, the same effort has not been made in developing models for biodiesel engines. In the case of sub-models for NO_x formation, the mechanism is fairly well-understood under high temperature high pressure operating conditions in engines. NO_x is primarily formed through the thermal route (Sun et al., 2010) and secondarily through the prompt mechanism (McCormick et al., 2003). The situation is different with regard to models for soot formation. In fact, accurate models do not exist even for conventional petrodiesel engines. Within the

context of multi-dimensional engines, not only must the model be accurate, it must also be simple.

The kinetic soot formation mechanisms are generally based on the hydrogen-abstraction carbon-addition (HACA) mechanism (Frenklach and Wang, 1991;1994). These kinetic models are, however, computationally intensive. Simple models based on an empirical understanding of soot formation and oxidation (Hiroyasu and Kadota, 1989), and two-equation semi-empirical soot models (Leung et al., 1991) have been formulated and employed in engine simulations (Abraham, 2013). None of the simpler models have been developed for biodiesel engine combustion. In fact, there is a lack of fundamental understanding in how soot is formed in biodiesel fuel combustion. The work in this thesis is motivated by a desire to improve this understanding and develop simplified models.

1.1 Objectives

The objectives of this work are the following:

1. Understand the impact of variations in turbulent strain on the combustion of petrodiesel and biodiesel in fundamental studies.
2. Identify the chemical kinetic pathways to the formation of soot in biodiesel combustion.
3. Develop simplified models for soot.
4. Apply the simplified models for soot to biodiesel spray combustion.
5. Investigate how non-reacting spray characteristics are affected by varying the biodiesel feedstock.

1.2 Thesis Outline

The remaining of this thesis will be divided into 9 chapters. They are listed below and consist of:

Chapter 2 presents a literature review of the topics relevant to this thesis. Non-reacting and reacting sprays in compression-ignition diesel engines, and ways to model them are discussed. The state-of-the-art of pollutant formation in the form of soot and NO, and in their modelling, is then presented. Then, the progress of biodiesel fuel combustion in diesel engines, and its difference compared to petrodiesel is briefly discussed.

Chapter 3 presents a detailed discussion of the in-house computational methods used in this thesis. First, a 1-dimensional flamelet code is presented. This flamelet code was used in the

study of sensitivity of soot to changes in scalar dissipation rate, the reaction pathway analysis, and the development of the semi-empirical two-equation soot model. Then, an in-house Reynolds-Average Navier-Stokes (RANS) multi-dimensional spray code is discussed. The spray code was used for all spray modelling.

In Chapter 4, non-reacting sprays of biodiesel fuel sourced from 7 different feedstocks are compared. The liquid-phase and vapour-phase penetration, and mixture fraction distribution of the fuels from these feedstocks are compared.

Chapter 5 discussed the effect of limit phenomena on diesel and biodiesel fuels. In particular, its effect on soot formation.

Chapter 6 builds upon the understanding of the limit phenomena and presents the formation of a reaction pathway analysis. In this analysis, a better understanding of the difference in soot formation between petrodiesel and biodiesel is established. A pathway of critical species that differentiate soot formation in the two fuels is presented.

Chapter 7 extends the knowledge of the critical species into developing a semi-empirical two-equation soot model. In this soot model, inception is modelled by the vinyl radical and surface growth by acetylene.

Chapter 8 validates the semi-empirical two-equation soot model by modelling soot formation of n-heptane, a petrodiesel surrogate, in 9 reacting spray cases of varying conditions. In the study, the soot model is compared to a kinetics-based soot mechanism, and another well validated semi-empirical two-equation soot model.

Chapter 9 compares modelled non-reacting/reacting sprays to measurement data for both diesel and biodiesel fuel. The results of the developed soot model are compared to measured data of soot from diesel and biodiesel reacting sprays.

Finally, Chapter 10 closes with a summary and conclusion of the thesis work.

2 Literature Review

2.1 Introduction

This chapter will briefly review spray and combustion characteristics of diesel and biodiesel sprays and engines. The literature review will start with an introduction to non-reacting/reacting diesel jets in Section 2.2. This is followed by a discussion of the current progress in modelling them in Section 2.3. Pollutant formation pathways, especially soot and NO, are expanded upon in Section 2.4. Section 2.5 reviews the progress in biodiesel fuel research and its comparison to diesel fuel. The literature review will close with a summary in Section 2.6.

2.2 Non-reacting/Reacting Diesel Jets

Diesel engines are attractive as prime movers because their higher compression ratio results in higher thermal efficiency, by as much as 30%, relative to petrol engines. In a typical diesel injection compression ignition (DICI) engine the liquid diesel fuel is directly injected into the cylinder at high injection pressure, typically 1500 bar or higher, into a chamber where the gas is at high pressure, typically greater than 40 bar, and high temperature, typically around 900 – 1,200 K (Heywood, 1988). During the process of high pressure injection, hot ambient air is entrained, due to momentum transfer, into the fuel stream near the nozzle, causing partial premixing of fuel and ambient air. The most accepted theory is that the fuel droplets go through two states of atomization: an initial stage where liquid breaks up into ligaments and drops, and a following stage where the ligaments and drops undergo secondary breakup (Abraham, 2013). However, the atomization process is still not well understood. By an axial distance of 50 – 100 nozzle diameters, the fuel is completely vaporised and the liquid penetration of the fuel reaches its maximum value (Siebers, 1998; Abraham and Pickett, 2010). The fuel/air mixture continues to penetrate the cylinder, and a head vortex forms at the leading tip of the spray. Over time, the maximum penetration of the vapour reaches a quasi-steady state distance, and this is known as the vapour penetration length. Figure 2.1 illustrates this spray process through a conceptual drawing.

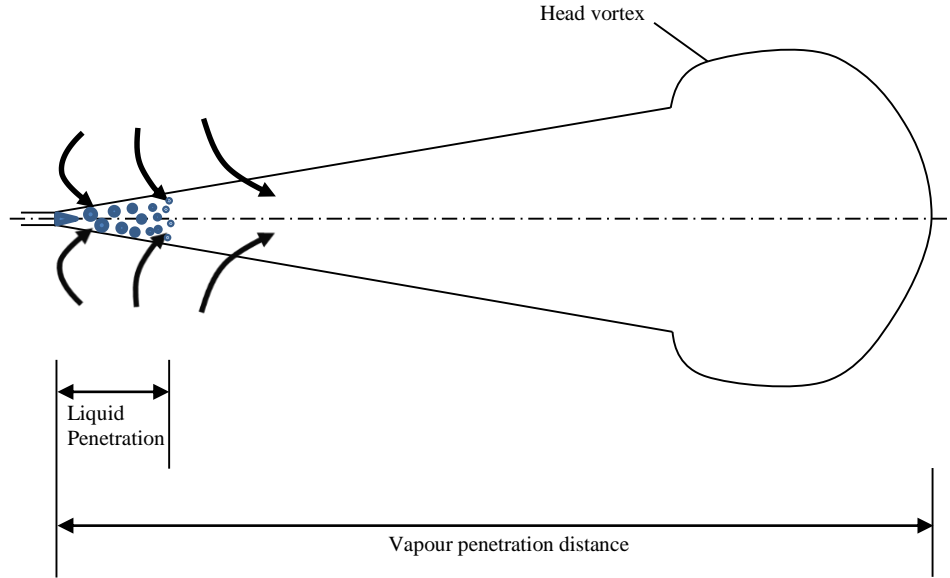


Figure 2.1: Conceptual drawing of a non-reacting diesel spray

In a non-reacting spray, it has been found that the maximum liquid length is directly proportional to the nozzle diameter, and injection pressure has little effect on it. On the other hand, ambient gas density and temperature affect the liquid length greatly, i.e., the higher the ambient gas density or temperature, the shorter the liquid length (Siebers, 1998). The process beyond the liquid length resembles that of a quasi-steady state turbulent gas jet (Hinze, 1975; Schlichting, 2000). It has been found that the vaporisation rate is entrainment controlled (Siebers, 1998). In terms of vapour penetration, it has been found that both non-vaporising and vaporising sprays have similar penetration distances with respect to time, and that the spreading can be modelled either as a vapour fuel jet, or as an incompressible gas jet (Bajaj et al., 2011). Bajaj and co-workers (2011) have also shown that if the vapour penetration distance, x , and time, t , are non-dimensionalised via the following:

$$x^* = \frac{x}{d \sqrt{\frac{\rho_i}{\rho_a}}}, \quad (2.1)$$

$$t^* = \frac{t U_i}{d \sqrt{\frac{\rho_i}{\rho_a}}}, \quad (2.2)$$

where x is the axial vapour penetration distance, d is the nozzle diameter, t is the time after the start of injection (ASI), U_i is the injection velocity, ρ_i and ρ_a are the fuel and ambient density, respectively, then the vapour penetration of all fuels collapse onto a single curve defined by:

$$x_{pen}^2 = 5.796 d (2\Delta P / \rho_a)^{0.5} t, \quad (2.3)$$

Where ΔP is the injection pressure across the nozzle. This is shown in Fig. 2.2. Both vaporising and non-vaporising sprays at ambient densities of 6.8, 14.8, and 28.6 kg/m³ collapse onto a similar curve profile.

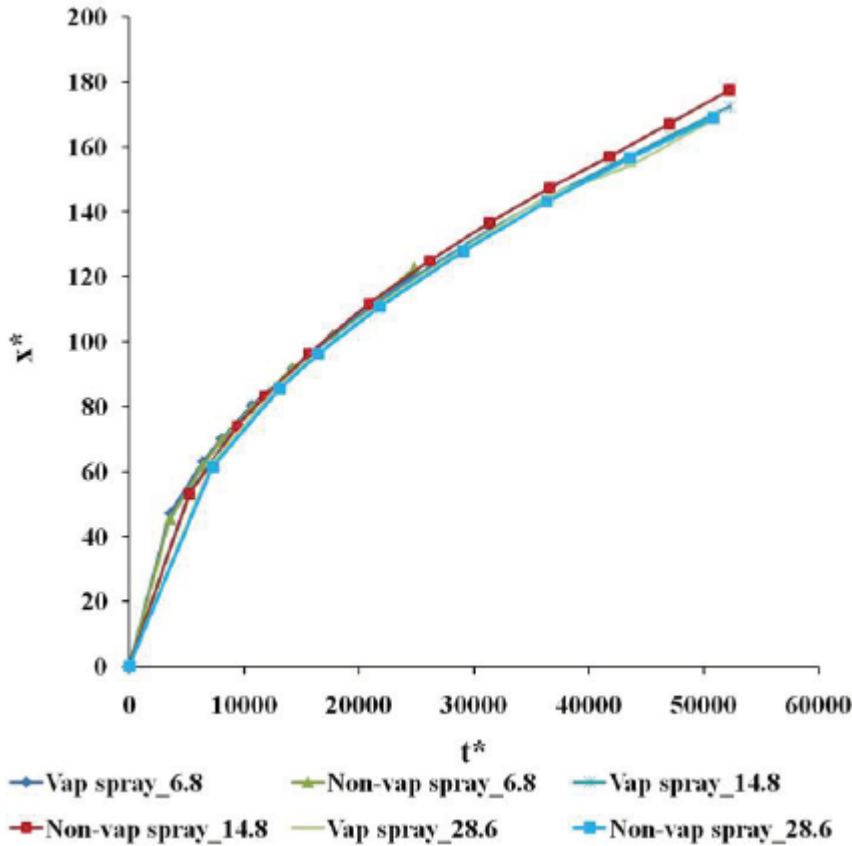


Figure 2.2: Non-dimensional axial penetration with respect to non-dimensional time for vaporising and non-vaporising sprays at different ambient densities (Bajaj et al., 2011)

If the right conditions exist in the chamber, the spray ignites and a flame is formed. Low, medium and high temperature chemistry reactions lead to a runaway reaction that causes ignition (Curran et al., 1998). It has been shown that ignition typically occurs at the tip of the spray (Dec, 1997). The time duration between the start of injection and ignition is deemed the *ignition delay*. Flame kernels also develop along the stoichiometric mixture fraction and quickly merge together to form a continuous flame. Over time, this flame moves upstream along the stoichiometric reaction zone to a certain distance away from the nozzle. This is known as the *lift-off length* (LoL). It is due to the ignition scalar dissipation rate, χ_{ign} , of the flame being overcome by the jet's local χ .

A physical understanding of χ can be obtained by assuming a stable flame. If χ is gradually increased, the increased flow gradient will cause more and more heat to be conducted away from the stoichiometric reaction zone. Beyond a certain χ_{st} , the flame will extinguish due to the heat being carried away faster than it can be produced by reactions. This is known as the extinction scalar dissipation rate. The phenomenon is plotted in the extinction and ignition S-

curve shown in Figure 2.3, which plots the temperature of a flame against the Damkohler number (Da), which is the ratio of the reaction timescale to the convection timescale. An increase in Da corresponds to a decrease in χ .

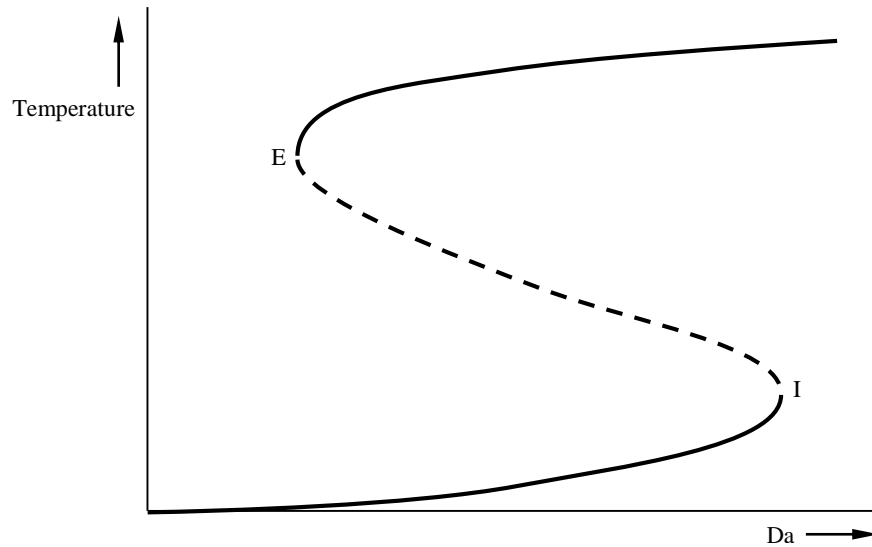


Figure 2.3: Ignition and extinction S-curve.

A stable flame will lie on the top portion of the S-curve in Figure 2.3. An increase in χ (decrease in Da), causes the flame to reduce in peak temperature along the top curve due to heat being carried away, and shift towards point E. Beyond point E, which is the extinction χ , the flame will extinguish. Conversely, if the Da is increased (reduction of χ), then the peak temperature will gradually increase along the lower curve until point I, where auto-ignition occurs. At this point, the temperature swiftly jumps to upper curve. Point I is usually referred to as the ignition limit of a fuel, and is when the heat from reactions just overcomes the effect of loss of energy due to turbulent effects.

Through measurements, it has been found that the LoL is inversely proportional to the ambient temperature, density, and oxygen concentration (Siebers and Higgins, 2001; Siebers et al., 2002). On the other hand, it is directly related to the injection pressure and to the nozzle diameter (Siebers and Higgins, 2001; Pickett et al., 2005). Other work has found that the soot volume fraction formed in a diesel spray is directly proportional to the LoL due to it determining the amount of ambient air that is entrained into the spray (Yen and Abraham, 2014, 2015). Figure 2.4 shows a conceptual illustration of a quasi-steady state developed flame. The liquid fuel is sprayed from the nozzle (on left), and entrains ambient air into the spray. A flame has developed at the leading tip and spreads upstream along the stoichiometric reaction zone to a certain distance away from the nozzle, defining the LoL. In this spray, the fuel/air mixture is highly stratified with some regions rich, other regions lean, and yet other regions flammable. The highest temperature is in the flammable mixture. At the high temperature reaction zone

region surrounding the jet, NO is formed. At the central bulb within the head vortex, soot is produced from polycyclic aromatic hydrocarbons (PAHs) that form upstream, just after the LoL within the spray, as they travel along the flame's centreline downstream (Dec, 1997). In a typical diesel engine, this entire process of injection, ignition and pollutant formation lasts for only a few milliseconds. Thus, the process is highly transient.

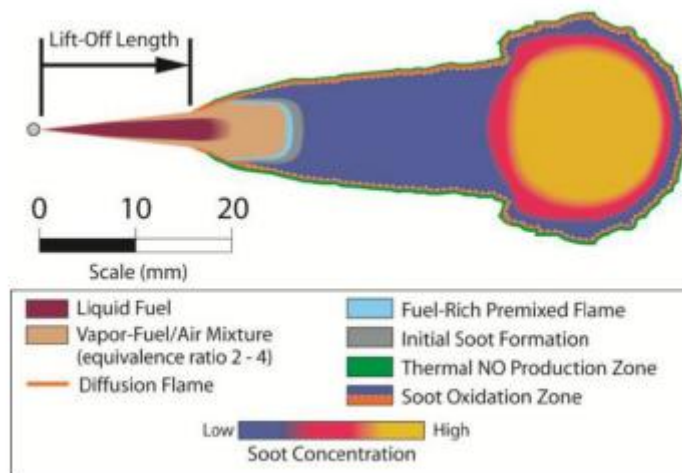


Figure 2.4: Conceptual illustration of a combustng diesel-jet (Dec, 1997).

2.3 Modelling of Petrodiesel and Biodiesel

A typical petrodiesel sample consists of over 100 species (Pitz and Mueller, 2011). It is difficult to represent the fuel with a unique chemical structure when modelling its combustion. Furthermore, many of the species are higher-order hydrocarbons with more than 10 or 12 carbon atoms whose chemical oxidation kinetics has not been fully characterized. Hence, it is necessary to identify surrogates for practical fuels like petrodiesel. While it is unlikely that the surrogate will accurately represent all the physical properties of the actual fuel (Battin-Leclerc, 2008), the expectation is that the surrogate will at least represent the essential physical and chemical properties that are of importance for the problem studied. For example, if the interest is in the formation of soot, then the surrogate chemistry must represent the fuel kinetics that are important in the formation of soot. If the interest is in atomisation, the surrogate must represent the surface tension and viscosity accurately. If ignition is of interest, the surrogate must represent the cetane number accurately. When determining diesel ignitability in an engine, a combination of hexadecane ($C_{16}H_{34}$) and hexamethylnonane ($C_{15}H_{32}$) are used as reference fuels (Murphy et al., 2004). Surrogates are easier to identify for biodiesel than petrodiesel because biodiesel chemical structure can be more easily characterized. (Please see Table 1.1). This does not imply, however, that their chemical oxidation mechanisms are well known.

2.3.1 Surrogates for Petrodiesel

This discussion will initially focus on surrogates that can represent chemical kinetics accurately. Among iso-alkanes, cyclo-alkanes, and monoaromatics which are the primary constituents of petrodiesel, alkane oxidation chemistry is better known than that of the others (Battin-Leclerc, 2008; Pitz and Mueller, 2011). During alkane oxidation, the long-chain hydrocarbons rapidly break down at fairly low temperature into shorter-chain hydrocarbons. Representing this breakdown is not so critical in representing the oxidation. In view of this, shorter-chain alkanes can be used as surrogates. The oxidation kinetics of these alkanes is reasonably well-known.

An important property of petrodiesel that has to be predicted accurately is the ignition delay in the engine. This is, of course, directly related to the oxidation chemistry. The ignition delay for various n-alkanes, from n-heptane (C_7H_{16}) to n-hexadecane ($C_{16}H_{34}$), was computed with 13.5 bar initial pressure at stoichiometric conditions. It was found that there was not much difference between the n-alkanes if ignition delay was the sole consideration (Westbrook et al., 2009). Shen et al. (2009) performed shock tube experiments at room temperature with pressures ranging from 9 to 58 atm. At an equivalence ratio of 0.5, the fuels tested, n-heptane, n-decane, n-dodecane, and n-tetradecane show very small variances in ignition delay as well. The different n-alkanes considered show qualitative and quantitative similarity in ignition characteristics. This is not surprising given the argument earlier that higher-order hydrocarbons break down to lower-order hydrocarbons rapidly during the oxidation process. Hence, the lowest-order hydrocarbon considered can be used as a surrogate if ignition delay is the controlling criterion.

The average chemical formula of petrodiesel which is sometimes given as $C_{12}H_{23}$ (Gogoi and Baruah, 2010), suggests that dodecane ($C_{12}H_{26}$) can be employed as a surrogate. Similarly, n-hexadecane which is one of the reference fuels in cetane number characterization can be employed as a surrogate. In fact, the physical properties of these fuels are similar to those of petrodiesel, and these alkanes, along with tetradecane, have been employed as surrogates in diesel engine simulations when the chemistry is represented by global reaction rates or local equilibrium characteristic time models (Hou and Abraham, 1995; Choi and Reitz, 1999). The oxidation kinetics of these fuels are, however, complex and still being developed. When mechanisms are available, they are generally large and not suitable for large-scale computations. For this reason, much effort has been dedicated to surrogates represented by lower-order hydrocarbons, with overall good results (Shen et al., 2009). In fact, n-heptane has been widely employed as a surrogate for simulating petrodiesel combustion characteristics

(Pitz and Mueller, 2011; Westbrook et al., 2009; Herbinet et al., 2008; Curran et al., 1998). In this work, n-heptane will be employed as the surrogate for petrodiesel.

Curran et al. (1998) have developed a detailed reaction mechanism for n-heptane with 654 species and 2826 reaction steps. This mechanism is fairly large for computational purposes. Hence, several skeletal and reduced mechanisms have been developed using the detailed mechanism as the starting point. One skeletal mechanism contains 160 species and 770 reactions (Seiser et al., 2000) and has been used in studies related to diesel combustion (Gopalakrishnan and Abraham, 2004; Venugopal and Abraham, 2007). Seiser et al. (2000) compared the ignition delay of the 160-species skeletal mechanism to mechanisms with 556 and 282-species at stoichiometric conditions. The mechanism was also compared to simulations run at pressures of 1, 3.2, 13.5, 42, and 100 bar and at initial temperatures of 625, 740, 909, 1176, and 1667 K. Results from shock tube experiments at 3.2, 13.5 and 38 bar were also included (Ciezki and Adomeit, 1993; Minetti et al., 1995). The results showed that the 160-species mechanism matched both the detailed mechanisms and experiments very well. As the 160-species mechanism is small enough to be computationally inexpensive, but offers accurate modelling results, it would be a suitable oxidation mechanism for the surrogate.

2.3.2 Surrogates for Biodiesel

As mentioned in the Introduction, the physical properties of the biodiesel fuel used depend greatly on the feedstock used to produce the FAME. This makes it difficult to select a universal surrogate to represent biodiesel. For example, the typical biodiesel feedstock in US is soybean oil whereas it is rapeseed oil in Europe, and their FAME chains have 16 to 18 carbon atoms (Battin-Leclerc, 2008). As in the case of petrodiesel, the chemical kinetics of these long-chain molecules has not been fully developed and, in rare instances, when they are available, they are too large to be employed in large-scale simulations. Two methyl esters, methyl butanoate ($n\text{-C}_3\text{H}_7\text{C}(=\text{O})\text{OCH}_3$) and methyl decanoate ($n\text{-C}_9\text{H}_{19}\text{C}(=\text{O})\text{OCH}_3$) are the most commonly proposed surrogates (Seshadri *et al.*, 2009). Methyl butanoate (MB) was investigated as a surrogate as it has the oxygenated chemical structure of biodiesel fuel, although it does not have the same number of carbon atoms or molecular weight (Fisher *et al.*, 2000; Brakora *et al.*, 2009). Modelling of MB has shown that it does not replicate the kinetic characteristics of biodiesel fuels as the carbon chain length is shorter than the average of biodiesel (Seshadri *et al.*, 2009; Luo *et al.*, 2012). Sarathy *et al.* (2011) found the NTC behaviour of large carbon chains were misrepresented by MB. Som and Longman (2011) found that the MB surrogate does not predict the flame lift-off and emissions properties of biodiesel

accurately. As an alternative, a methyl decanoate (MD) mechanism has been developed by Sharp *et al.* (2000a, 2000b) that display results closer to biodiesel combustion than MB due in part to the longer carbon chain and having an ester group. Sarathy *et al.* (2011) performed both an opposed-flow diffusion flame (OppDif) experiment and a kinetic modelling simulation of MB. The experiment had 99% pure MD fed from one inlet and an oxidizer mixture of 42.25 % O₂ and remainder N₂ flowing through the other at an overall laminar flow regime. The kinetic modelling was done using an intermediate-sized mechanism using the OppDif code in CHEMKIN (Reaction Design, 2010). It was found that the experimental findings validated the modelling results very well. Further modelling and experiments were done to validate the MD mechanism (Glaude *et al.*, 2010). The experimental set-up consisted of a constant pressure jet-stirred reactor (JSR) running at a constant pressure of 1.06 bar and residence time of 1.5 s under stoichiometric conditions. The modelling was conducted using the perfectly-stirred reactor (PSR) model in CHEMKIN for a 1251-species MD mechanism, assuming a homogeneous isothermal reactor. It was found that the results lead to a good level of agreement, with only slight differences due to the way the mechanism was generated.

However, the mechanisms used for modelling had been too large to become computationally economical. For example, a detailed mechanism consisting of 3299 species and 10806 reactions has been developed by the Lawrence Livermore National Laboratory (LLNL) for the ternary mixture of MD, methyl-9-decenoate (MD9D) and n-heptane (Herbinet *et al.*, 2010). In response, skeletal mechanisms have been produced to reduce the size to 1251 species, mentioned above, or a 648-species 2998-reaction mechanism (Sarathy *et al.*, 2011). However, these are still too large for cheap computational use. Luo *et al.* (2012) has thus developed a smaller skeletal mechanism that consists of 115 species and 460 reactions. The 115-species mechanism retained the three surrogates from the 3299-species detailed mechanism and has physical and chemical properties similar to those of biodiesel. The surrogates were in a mixture of 25% MD, 25% MD9D and the remainder n-heptane. As the fuel mixture consisted of three parts, the tri-component biodiesel surrogate mechanism shall be known henceforth as the ternary biodiesel surrogate X (TBSX), with X being the number of species. Demirbas (2009) proceeded to conduct three validations of the TBS 115. First, the TBS115 was compared to the 3299-species mechanism in terms of ignition delay and in extinction temperatures in a PSR. At ϕ of 0.5, 1 and 2, and pressures of 1, 10 and 100 atm, the TBS115 matched the detailed mechanism very well in all conditions for both ignition delay and extinction temperatures. The TBS was then compared to experimental findings by Herzler *et al.* (2005) and the detailed mechanism at a $\phi = 0.4$ and pressure of 50 bar in a JSR. Again, the results showed that the TBS115 followed the experimental data closely. Lastly, the TBS115

was validated in CI engine conditions in a 3-D constant volume combustion chamber. The experimental data was taken from the Sandia National Laboratories through personal communication. The fuel liquid penetration, vapour penetration, lift-off length and ignition delay were compared. In all cases, it was found that the TBS115 matched experimental findings well. As the TBS115 is small enough to be computationally practical and shows reasonably accurate results, it would be a suitable oxidation mechanism for the surrogate of biodiesel fuel. As in all surrogate mechanisms, however, it is important to point out that the mechanisms may not be applicable in general for all pressure and temperature conditions, and oxidizer mass fractions. This always raises questions about conclusions that are drawn when these mechanisms are employed, especially under engine conditions.

2.4 Pollutant Formation Pathways

Although many pollutants are formed in a typical diesel engine's combustion process, such as carbon monoxide and unburnt hydrocarbons, the two that have received the most research attention are NO_x and soot. NO_x contributes to ozone formation, acid rain and respiratory tract irritation (Speizer et al., 1980). Soot has been reported to lead to harmful health effects, e.g. lung cancer, and it is a potent global warming agent (Dockery et al., 1993; Kittelson, 1998; Siegmann et al., 1998; Tornqvist et al., 2007; Scheepers and Vermeulen, 2012). There is a clear need to further develop engines which generate lower soot and NO_x emissions without compromising the high-efficiency of conventional diesel engines.

2.4.1 NO

There are three main mechanisms for NO formation: thermal, prompt, and N₂O. The thermal mechanism is also known as the Zeldovich mechanism for its discoverer (Zeldovich, 1946). The overall reaction is expressed as:



However, as the name of the mechanism suggests, this reaction is highly endothermic as the N₂ and O₂ bonds are very hard to break. Instead, the oxygen radicals, formed from the dissociation of O₂, react with N₂, instead. This starts a chain propagation mechanism:

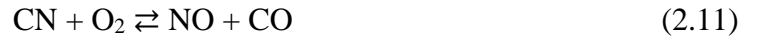


Nitrogen radicals are consumed in the following reaction:

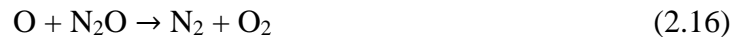


Due to the high level of energy required to break the N_2 triple-bonds, Eq. (5) is rate-limiting. This mechanism occurs only at high temperatures, usually greater than 1,800 K. Due to the high flame temperatures in a diesel spray, this is the most likely path for the formation of NO in petrodiesel and biodiesel sprays.

The second mechanism for NO formation is the prompt mechanism. Discovered by Fenimore (1971), this mechanism occurs at low temperatures and at fuel-rich conditions. Under these conditions, hydrocarbon radicals, in particular, CH, react with N_2 in the following reactions to form NO:



The third mechanism in which NO can form is through the contribution of N_2O (Bowman, 1992), which occurs at low temperatures and high pressures. This mechanism involves the following reaction:



In Eq. (14), M represents a third-body that does not participate in the reaction, but adds energy to the reaction via collision. Due to the conditions of the prompt and N_2O mechanisms, NO does not form in large quantities via these means in a typical diesel engine. The thermal mechanism is the main pathway for NO formation.

Due to the fact that the NO formation mechanism is quite well established, many modelling studies of NO in diesel sprays under engine condition (Agarwal and Assanis, 1997; Gopalakrishnan and Abraham, 2004; Kong et al., 2007; Li and Kong, 2008) utilise the GRI-Mech 3.0 mechanism (Smith et al., 1999). In general, it has been found that the predicted NO matches well with measurements in the engine exhaust.

2.4.2 Soot

In essence, soot is mostly spherical carbon with a diameter ranging between 20 – 30 nm (Haynes and Wagner, 1981). Particles can group together to form large chain structures. After the initial combustion process of fuel, polycyclic aromatic hydrocarbons (PAHs) form. The first such species is benzene (C_6H_6), also known as *A1* due to it being a single aromatic ring. There is still debate as to what most likely pathway is taken for benzene to build up to soot. Although there have been alternative PAH formation pathways proposed in the literature, (Thomas, 1962; Senosiain and Miller, 2007; Shukla and Koshi, 2012), the most widely accepted mechanism is still through hydrogen-abstraction carbon-addition (HACA) (Frenklach and Wang, 1994). This mechanism has been represented in kinetics models (Frenklach and Warnatz, 1987; Kazakov and Frenklach, 1998; Frenklach et al., 1988; Appel et al., 2000). The PAH build-up process via the HACA mechanism is shown in Figure 2.5. Beginning with benzene, a hydrogen atom is abstracted from the aromatic ring to form a cyclic C_6H_5 radical. Carbon, in the form of acetylene (C_2H_2), is added to the reactive site. Hydrogen is abstracted once again, and another acetylene species is added. This forms naphthalene (*A2*). This two-step process is repeated to form larger aromatic species (*A3*, *A4*, etc).

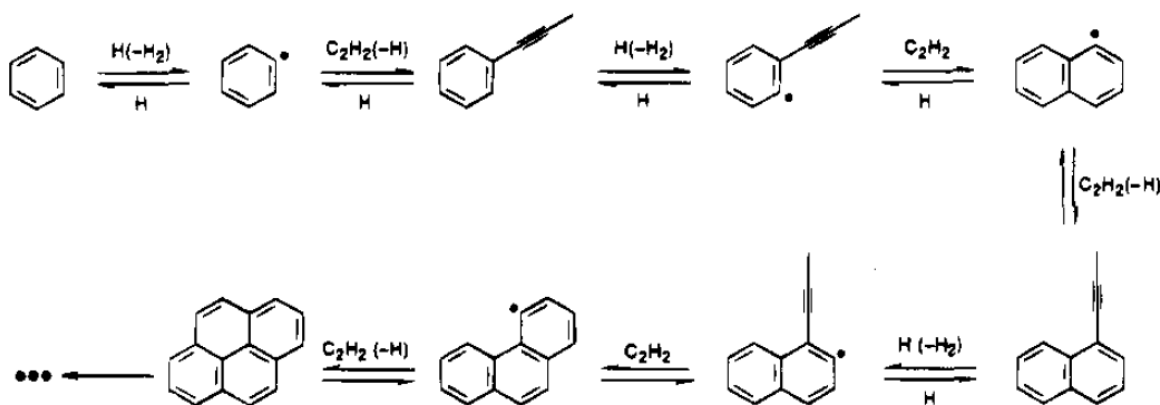


Figure 2.5: PAH build-up via the hydrogen-abstraction carbon-addition mechanism (Frenklach and Wang, 1994).

Once the PAH species builds up to approximately 1.5 nm, the soot formation process transforms from a molecular-basis to a particle-basis (Richter and Howard, 2000). This large PAH is now considered as an *inception species*. Growth can now be due to both chemical addition of PAHs

to the inception species, deemed *surface growth*, or by *coagulation*, where two soot particles collide and merge physically. Figure 2.6 shows the stages of formation of soot.

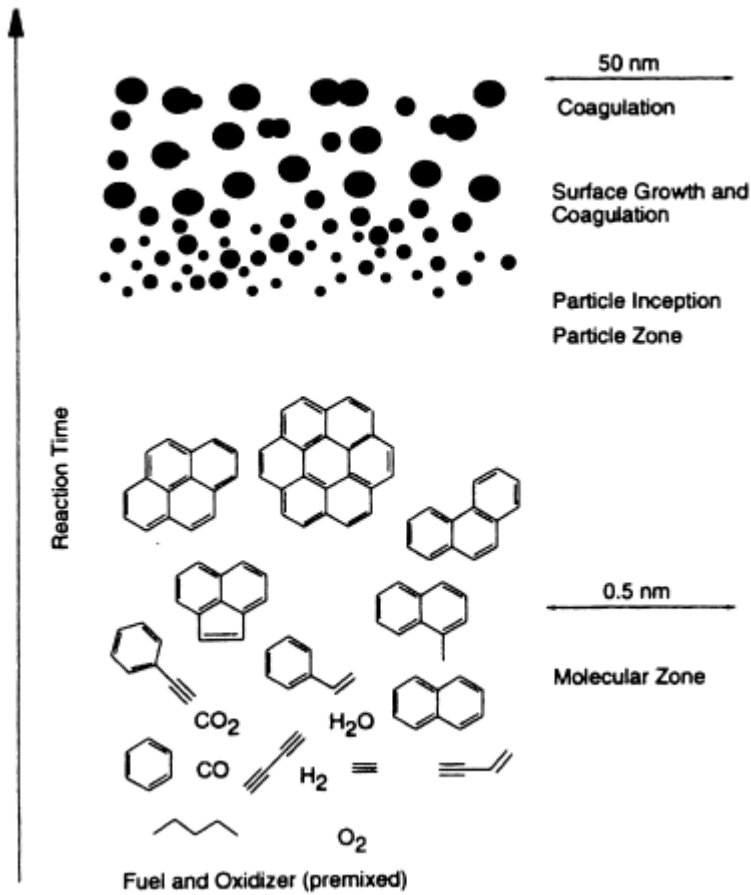


Figure 2.6: Stages of soot formation and growth (Bockhorn, 1994).

The oxidation of soot works against its formation. It is found that the primary pathway of soot oxidation is through O_2 and OH (Kennedy, 1997). In a gas burner set-up, Lee et al. (1962) studied the rates of combustion of soot and, in particular, the stages of oxidation. Using a tri-component hydrocarbon mixture of C_3H_8 , C_2H_4 and C_3H_6 , a semi-empirical relationship between the oxidation rate and partial pressure of oxygen (P_{O_2}) was derived:

$$Oxidation\ rate = 1.085 \times 10^4 \times P_{O_2} \times T^{-1/2} \times \exp\left(\frac{-19,848}{T}\right) \times S, \quad (2.18)$$

where P_{O_2} is the partial pressure of oxygen and T is temperature, and S is the surface area of a typical soot particle. It is defined as:

$$S = \pi \left[\frac{6\rho y_s}{\pi\rho_{c(s)}N} \right]^{2/3} N, \quad (2.19)$$

where ρy_s is the soot volume fraction, $\rho_{c(s)}$ is the density of the soot particle, and N is the soot number density. The Lee et al. (1962) oxidation model was found to lead to results that matched measurements well (Garo et al., 1990; Leung et al., 1991).

Nagle and Strickland-Constable (1962) showed in measurements of graphitic carbon at low to atmospheric oxygen and between 1,100 – 2,500 K, that O_2 attacks two reactive sites. The mechanism proposed is shown below:

$$\text{Oxidation rate} = \frac{12 \times S}{M_{c(s)}} \left[\left(\frac{K_A P_{O_2}}{1 + K_Z P_{O_2}} \right) x + K_B P_{O_2} (1 - x) \right], \quad (2.20)$$

where,

$$x = \frac{P_{O_2} K_T}{P_{O_2} + \frac{K_T}{K_B}}, \quad (2.21)$$

$$K_A = 20 \times \exp\left(\frac{-30,000}{T}\right), \quad (2.22)$$

$$K_B = 4.46 \times 10^{-3} \times \exp\left(\frac{-15200}{T}\right), \quad (2.23)$$

$$K_T = 1.51 \times 10^5 \times \exp\left(\frac{-97000}{T}\right), \quad (2.24)$$

$$K_Z = 21.3 \times \exp\left(\frac{4100}{T}\right), \quad (2.25)$$

In Eq. (2.20) – (2.25), $M_{c(s)}$ is the molecular mass of one carbon atom. The kinetic expression above is based on the assumption that the CO radical is the primary product formed. This oxidation mechanism is well validated and found to replicate oxidation rates well (Lee et al., 1962; Tesner and Tsibulevsky, 1967).

As an alternative to the O_2 oxidation, Fenimore and Jones (1966) developed an OH oxidation mechanism. In their experiments of oxidation of graphite at conditions of P_{O_2} between 0.04 – 0.30 atm and temperatures in the range of 1500 – 1900 K, it was found that changes in P_{O_2} had little effect. The rate of oxidation was found to be significantly higher if than if O_2 oxidation was only considered. Thus, it was postulated that this was due to OH radical attack on graphite. The oxidation rate via OH proposed is given below:

$$\text{Oxidation rate} = 1.63 \times 10^4 \times \alpha \times P_{O_2} \times P_{H_2O} \times T^{-1/2} \times \exp\left(\frac{-37.8}{T}\right), \quad (2.26)$$

where α is 0.1, P_{O_2} is 0.075, and P_{H_2O} is 0.2.

Despite the considerable progress made by the scientific community towards the study of soot, the intricate details of its formation and destruction are still elusive (Richter and Howard, 2000). However, due to the urgent need to reduce soot emissions as a harmful pollutant, or maximise its production in industrial usage, current knowledge about soot formation and oxidation has often been employed to develop engineering models that can be utilised by researchers and engine designers. Such models range in complexity. The simplest models are empirical relations that are developed to match specific experimental conditions. The rate of soot formation and oxidation are each modelled via one equation. Although these models are simple, they provide researchers a quick way to estimate the soot formed in a system. Khan et al. (1971) developed an empirical model to match the soot concentration from a diesel engine exhaust. An alternative empirical soot model from a similar set-up was also developed by Mehta and Das (1992). Perhaps the most widely employed empirical soot model developed for the diesel engine spray was by Hiroyasu and Kadota (1976). The following equation for soot formation and oxidation are employed in the model:

$$\frac{dm_f}{d\theta} = \left(C_g \frac{dm_{fi}}{d\theta} + c_l m_{lt} \right) P \cdot \exp\left(\frac{-10,000}{T}\right) \frac{1}{\omega}, \quad (2.27)$$

where m_f is the mass of soot formed, m_{fi} is the mass of fuel burnt, m_{lt} is the mass of liquid fuel in the domain, P is the domain pressure, ω is the angular velocity.

$$\frac{dm_o}{d\theta} = C_b V_u \frac{6m_f}{\rho_{c(s)} d_c} \cdot P_{O_2} \cdot \exp\left(\frac{-39,300}{RT}\right) \frac{1}{\omega}, \quad (2.28)$$

where m_o is the mass of soot oxidised, V_u is the volume, $\rho_{c(s)}$ is the soot density, d_c is the mean diameter of the carbon particle, and R is the gas constant. In both Eq. (2.24) and (2.25) C_g , C_l , and C_b are constants calibrated to match experimental conditions. The overall soot formation is determined by:

$$\frac{dm_s}{d\theta} = \frac{dm_f}{d\theta} - \frac{dm_o}{d\theta}, \quad (2.29)$$

where m_s is the overall mass of soot formed. This soot model is well studied and, for a simple empirical soot model, can be modified to obtain reasonably accurate predictions of soot (Elkothb, 1982; Faeth, 1983; Kouremenos et al., 1990). However, all the complex soot formation/destruction processes are simplified into only three equations.

A more detailed alternative to the empirical formulation is a semi-empirical soot model. Such models include additional complexity by including sub-models for soot inception, soot surface growth, and coagulation to replicate the chemistry and physics more closely

(Kennedy, 1997). In addition, a semi-empirical soot model does not have to be re-tuned to match individual experimental conditions; it can, in principle, be employed over a wider range of conditions provided the primary fuel is not changed. In most semi-empirical two-equation soot models, two transport equations are employed: one for the soot density or volume fraction, f_v , and the other for the soot number density, N . Source/sink terms contribute to each. An example is shown below:

$$\frac{df_v}{dt} = \textit{Inception} + \textit{Surface Growth} - \textit{Oxidation} , \quad (2.30)$$

$$\frac{dN}{dt} = \textit{Inception} - \textit{Coagulation} , \quad (2.31)$$

where f_v and N represent the soot volume fraction and number density, respectively. Much work is directed at developing two-equation semi-empirical soot models. It has been shown that reasonable accuracy can be achieved with such models while delivering computational speed-up relative to kinetic soot models (Leung et al., 1991; Moss et al., 1995; Lindstedt and Skevis, 1997; Kazakov and Foster, 1998; Tao et al., 2009; Vishwanathan and Reitz, 2010; Farrace et al., 2013; Sukumaran et al., 2013).

As an example of a previous model based on this approach, consider that of Lueng et al. (1991). In their model, soot inception is exponentially dependent on temperature and linearly dependent on acetylene concentration; surface growth is exponentially dependent on temperature, linearly dependent on acetylene concentration and also a function of surface area which is determined from the number density and the density of soot; a separate model for PAH condensation is not included; and soot oxidation is an exponential function of temperature, a function of surface area, and a linear function of oxygen concentration. Their oxidation model is based on the work of Lee et al. (1962) who had assessed it in co-flow methane-air flames. For the number density source terms, soot nucleation increases the number of soot particles and agglomeration decreases the number. Agglomeration is modelled to have a square dependence on the number density and a linear dependence on temperature. The results presented by the authors show good agreement for volume fraction and satisfactory agreement for number densities in ethylene diffusion flames under atmospheric conditions. Another example of a two-equation model is the one proposed by Moss et al. (1995). In their model, source/sink terms for soot volume fraction are nucleation, surface growth, and oxidation and source/sink terms for the number density are nucleation and coagulation. Similar to the model of Leung et al. (1991) soot nucleation is exponentially dependent on temperature and linearly dependent on the concentration of a representative fuel species. In the model by

Moss et al. (1995), the representative fuel species is assumed to be the total of all the hydrocarbons. The activation energy for soot nucleation and surface growth is adopted from Gilyazetdinov (1972) and they are different from those of Leung et al. (1991). Oxidation mechanisms via oxygen and OH use the models of Nagle and Strickland-Constable (1962), and Fenimore and Jones (1967), respectively. This is also different from the approach of Leung et al. (1991). Satisfactory agreement of predicted and measured values in a laminar ethylene diffusion flame has been reported when employing the model (Vishwanathan and Reitz, 2008). These two examples show that there are differences in how the various terms in the two-equation model are formulated and the various constants have to be calibrated. There is no consensus on what the important species and mechanisms are. Nevertheless, these models are powerful engineering tools. While the choice of inception species may vary, e.g. acetylene, benzene, or pyrene, for example, the choice of the surface growth species is usually acetylene. This is in line with the understanding of the HACA mechanism (see Fig. 2.5). Due to their extra considerations, two-equation semi-empirical soot models tend to offer a better prediction of soot compared to the empirical soot models, at higher computational expense.

Soot formation and oxidation have also been modelled by employing detailed kinetic mechanisms. Such models track the formation of soot polycyclic aromatic hydrocarbons (PAHs) kinetically up to a sufficiently large species, such as pyrene (Lindstedt, 1994; Yoshihara et al., 1994; Kazakov et al., 1995). Beyond that, soot is modelled. For example, the kinetic soot model proposed by Frenklach and Wang (1991, 1994), contains a kinetic mechanism consisting of 101 species in 546 reactions. Starting with benzene, reactions follow the HACA mechanism and end with the species pyrene. Such kinetic soot models offer detail and potential accuracy, at the expense of computational economy. In addition, the base fuel kinetics mechanism has to be sufficiently robust to support the soot kinetics soot model. For instance, a 44-species n-heptane kinetics mechanism (Liu et al., 2004) might not contain sufficient number of species to make the kinetics soot model accurate enough compared to a 160-species n-heptane mechanism (Seiser et al., 2000).

In spite of the continuous development of soot models for diesel engines, many issues still plague researchers. Many are on the fundamental level, such as the most likely PAH growth path and how soot is oxidized. In many cases, quantitative predictions are difficult (Kennedy, 1997; Richter and Howard, 2000). Recent work by Kohler et al. (2012) have shown that the simulated PAH peak is far upstream compared to experimental measurements. This is shown in Fig. 2.7. As can be seen, even with the all the work of the scientific community, there

are still fundamental issues where, soot formation is predicted too upstream, or oxidation is over-predicted downstream of the domain.

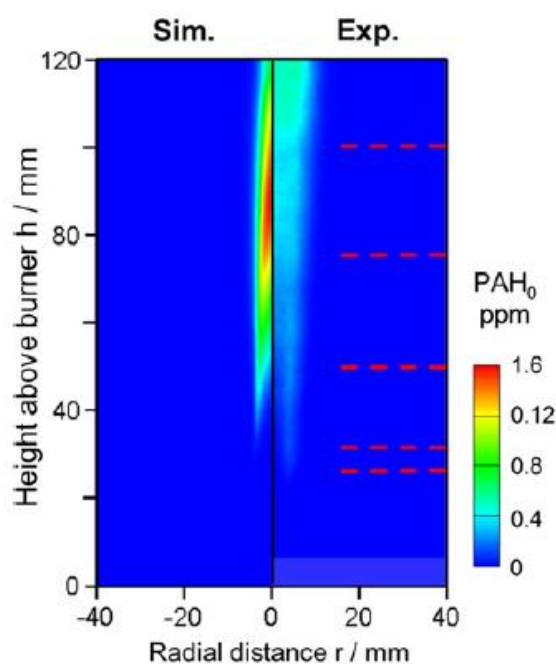


Figure 2.7: Simulated and measured PAH concentration of a turbulent flame (Kohler et al., 2012).

2.5 Biodiesel Fuel Research

As mentioned in the Introduction, biodiesel is fundamentally different from petrodiesel in its chemical structure. Due to it being derived from organic matter, its structure is that of an oxygenated fuel. As such, its breakdown process differs from hydrocarbons, and has been studied to better understand its combustion kinetics (Herbinet et al., 2008; Westbrook et al., 2011; Lai et al., 2011). However, compared to other hydrocarbons, detailed studies into the kinetics of biodiesel are still lacking. In general, the fuel oxidation process is similar to that of other fuels, apart from the intricacies of the $-\text{COOH}$ group. Figure 2.8 illustrates the general steps. At higher temperatures, hydrogen radical abstraction and C – C bond breakup lead to smaller alkyl and ester species (Turns, 1996). Following reactions might be isomerisation or to smaller hydrocarbons. Even further down the line, abstraction with O_2 lead to unsaturated esters, olefins and HO_2 . The olefins break along standard hydrocarbon pathways while the ester group forms alkoxy groups (Herbinet et al., 2008). Throughout the process, the oxygen atoms attached to the original biodiesel fuel never break away. This is due to these bonds being too strong (Feng et al., 2012). This has substantial consequences in pollutant formation of biodiesel fuels.

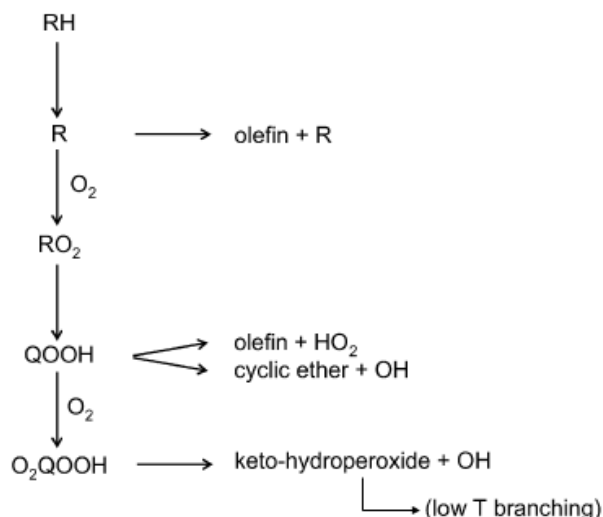


Figure 2.8: Primary oxidation pathway of a typical biodiesel fuel (Herbinet et al., 2008).

Each feedstock results in a biodiesel fuel that contains different compositions of fatty-acid methyl esters (FAMES). These differences, such as carbon chain length, degree of saturation, and isomerisation affect physical and chemical properties to a great extent which, in turn, influence spray and combustion properties (Knothe, 2005; Herbinet et al., 2010). While there have been significant work carried out on hydrocarbon oxidation, there has been less work on oxidation of biodiesel fuels or their surrogates. One detailed mechanism, consisting of a tri-component mixture of n-heptane (C_7H_{16}), methyl decanoate (MD), and methyl-9-decenoate (MD9D), was developed by Herbinet et al. and contains over 3,000 species, and 10,000 reactions (Herbinet et al., 2000). This was expanded to over 4,800 species and 20,000 reactions in an updated work (Westbrook et al., 2011). Mechanisms of such detail are unsuitable for use in multi-dimensional modelling because they add dramatically to computational cost. Alternative biodiesel fuel surrogate mechanisms are based on oxidation of methyl butanoate ($C_5H_{10}O_2$) (Fisher et al., 2000; Brakora et al., 2008; Brakora, 2013). However, as the average composition of the most commonly found FAMES in biodiesel feedstocks is $C_{18}H_{36}O_2$, methyl butanoate (MB) is an unsuitable fuel surrogate for biodiesel modelling in terms of cetane number, lower heating value (LHV) and O:C ratio (Szybist et al., 2007; Lee and Huh, 2013). To attempt to resolve this, Lee and Huh (2013) combined MB with n-heptane to restore the LHV and O:C ratio. In computations in a modelled compression-ignition cylinder, the spray penetration was in agreement with measured data and the Sauter mean diameter (SMD) was found to be larger than for diesel fuel. In addition, due to the lower LHV of biodiesel, it was reported that the peak temperature reduced.

The modelling of biodiesel fuels is challenging because biodiesel fuel may be sourced from a variety of feedstocks, such as soybean, corn, or palm (Yuan et al., 2003). While there have been numerous experimental studies comparing the performance and emissions of diesel

and biodiesel engines, numerical studies that explain the differences in emissions, especially soot, are few. This is because of the challenge of modelling soot in a way that the kinetics differences in the formation and oxidation in diesel and biodiesel sprays can be accurately predicted. A study by Golovitchev and Yang (2009) blended MB with n-heptane and methoxybenzene (C_7H_8O) to better represent the oxidation kinetics of biodiesel fuel. The kinetics model was employed to predict soot in a constant-volume chamber. It was found that predicted soot in biodiesel sprays was lower than in diesel sprays. Kitamura et al. (2001, 2002) employed a kinetics mechanism to model soot via poly-aromatic hydrocarbon (PAH) formation in various oxygenated fuels. It was found that PAH formation in these fuels was reduced as compared to PAH formation in n-heptane oxidation. Recall that n-heptane is often employed as a surrogate for diesel. These studies suggest that kinetics-based soot models can predict the differences in soot in diesel and biodiesel sprays. It has been shown (Cai and Abraham, 2013) that soot formation in biodiesel combustion is not just inhibited because of the existence of fuel-bound oxygen. These O – C bonds are too strong. Rather, due to the strong O – C bonds, the fuel oxidation pathway of biodiesel is altered to favour the formation of alkoxy groups, such as alcohol and aldehyde species. This results in a smaller pool of soot precursors available in biodiesel to form soot, as compared to petrodiesel. This finding was also supported by Feng et al. (2012). It is clear that oxidation process of biodiesel fuel has to be better understood through measurements and enhanced chemical kinetics mechanisms. Current available kinetic models, however, are not practical for industrial applications because they are computationally intensive.

The differences between biodiesel and diesel engine performance have been extensively studied in the literature. Sheehan et al. (2000) replaced petrodiesel in buses with pure biodiesel and found a total life-cycle reduction of petroleum use by 95%. In addition, for every unit for petroleum used, 3.2 units of biodiesel are produced resulting in a net reduction in carbon emissions on a life-cycle basis. This makes biodiesel production an attractive way to increase national energy security and utilise land not suitable for edible crops (Odeh et al., 2011).

Another advantage of biodiesel utilisation lies in its reduced soot emissions. Many studies have reported biodiesel being able dramatically reduce soot emissions by up to 70 % (Graboski and McCormick, 1998; Ma and Hanna, 1999; Krahl et al., 2003; Knothe et al., 2006; Song et al., 2006; Szybist et al., 2007; Lapuerta et al., 2008). In a study by the U.S. National Biodiesel Board using neat biodiesel in three heavy-duty engines, soot emissions reduced by 25%, and unburnt hydrocarbons reduced below what the instruments could measure (Sharp et al., 2000a, 2000b). One reason postulated for the reduction of soot has been that the fuel-bound oxygen facilitates more a complete combustion (Lapuerta et al., 2008), however,

this is now known not to be true. Frijters and Baert (2006) found a positive correlation between oxygen content in various biodiesel blends and particulate emissions. Another factor suggested is the absence of aromatics in biodiesel fuel combustion (Bagley et al., 1998). Absence of aromatics, according to various soot formation pathways proposed, is critical to soot development (Frenklach and Wang, 1991;1994). It has also been suggested that the higher cetane number which results in a shorter ignition delay in biodiesel engines leads to longer duration of combustion which oxidises the soot (Cardone et al., 2002). Ng et al. (2012) performed in-cylinder simulations of biodiesel combustion in a light-duty diesel engine and concluded that the soot formation is dependent on the amount of unsaturated bonds in the fuel and its likelihood to form aromatics. Furthermore, the oxidation of soot depends on its length of exposure to oxidation and the average cylinder temperature. While all the suggested causes of lower soot emissions are plausible, there is no firm agreement on which of the factors are more significant (Lapuerta et al., 2008). Thus, more fundamental studies are needed in the area of soot emission in biodiesel fuels.

In general, the emission of NO_x from biodiesel engines has been reported to be about 10 – 12 % more than from petrodiesel engines (Canakci, 2005). This has been attributed to several fuel properties: the oxygen content in biodiesel, higher cetane number, increased density, and increased combustion temperatures (Anand et al., 2011). However, under certain conditions, particularly retarded fuel injection, it has also been reported that the NO_x emissions are lower from biodiesel engines (Raheman and Phadatare, 2004; Kegl, 2008). This has been attributed to retarded injection resulting in lower peak combustion temperatures in the engine (Machacon et al., 2001; Raheman and Phadatare, 2004). It has also been claimed that there is no statistical significance to the observed differences in NO_x emission data (Song et al., 2006). Methods to reduce NO_x emissions by blending biodiesel with methanol or reformulated biodiesel have been proposed (Hess et al., 2005; Anand et al., 2011). Recently, there have been computational studies to understand the kinetics of NO_x formation in engines (Yang et al., 2012; Zhang et al., 2012). Yang et al. (2012) suggest that the increased NO_x emission from biodiesel combustion was due to the overall leaner conditions in the combustion chamber compared to petrodiesel arising from the fuel-bound oxygen to the mixture ratio. On the other hand, (Zhang et al., 2012) state that the main reason is due to an increase in overall cylinder temperature. It is important to note that none of these studies has identified or focused on the fundamental reason for the differences in NO_x emissions from biodiesel and petrodiesel engines. Much of the discussion has been speculative.

Biodiesel fuels, in general, are known to have a lower heating value than petrodiesel. This is attributed to the chemically bound oxygen (Giakoumis, 2013). This reduction of heating

value results in lower energy density. The general consensus is that substitution of petrodiesel with biodiesel in engines without any modification generate approximately 10 % less power and torque (Giakoumis, 2013). Other studies report reduction in power and torque of 1 – 5 % (Çetinkaya et al., 2005; Lin et al., 2006). Raheman and Phadatare (2004) observed higher rated torque. This was explained by the higher than average density of the liquid fuel. Zhang et al. (2012) found in a computational study that although methyl decanoate and methyl-9-decanoate released similar amounts of heat, methyl decanoate still produced a more powerful engine because of its lower cetane number. Thus, the power output may depend on both ignition timing and heating value of the fuel. As with NO_x and soot emissions, there is no definitive work which shows that biodiesel combustion is fundamentally more efficient than petrodiesel combustion. As a result, reasons given for observed differences in engine performances are often speculative. It is important to understand the difference from a fundamental perspective.

One other factor for consideration is that biodiesel fuel may not be produced from a single feedstock. For example, biodiesel can be derived from palm oil, soybean oil, algae, or even animal tallow. The choice of feedstock is often determined by regional climates and availability. As such, biodiesel produced from palm oil feedstock will have different properties to that made from animal tallow. As discussed in the Introduction, this is due to each feedstock resulting in a biodiesel sample containing a different composition of fatty acid methyl esters (FAMES) (Giakoumis, 2013). The influence of feedstock selection on the biodiesel properties has been studied in the literature. Knothe (2006) discussed the properties of lipid chain lengths ranging from C8:0 to C22:1. In this notation, C22:1 would indicate a lipid chain of 22 carbon atoms with 1 double bond. The melting and boiling points, the cetane number, viscosity, and heat of combustion were compared in that work. The work of Knothe (2006) was extended by Giakoumis (2013), who tabulated the distribution of FAMES for several feedstocks. Properties such as cetane number, heating value, and density were discussed in depth, with a focus on the effects of unsaturation on the properties. It was found that as density increased, the cetane number decreases, and as the degree of unsaturation increased, the heating value increased. Other studies have focused more narrowly on specific properties, such as the thermal properties (Castro et al., 2005), vapour pressure (Yuan et al., 2005; Castellanos Diaz et al., 2012), enthalpy of formation (Lapuerta et al., 2010), and adiabatic flame temperatures (Glaude et al., 2010). Yuan et al. (2003) presented methods for predicting and modelling many physical properties, such as density, surface tension, and latent heat of vaporisation, to an accurate degree of within 1 %. These studies vastly improved the ease of biodiesel fuel modelling. Despite being numerous prior studies on biodiesel spray modelling (Wang et al., 2010; Som et al., 2010; Mancaruso et al., 2011), and many more that compare biodiesel and diesel engine combustion

performance via measurements. However, to the authors' best knowledge, there has not been a study carried out to assess how the feedstock properties themselves affect spray characteristics. More fundamental studies are needed.

2.6 Summary

As the review shows, there are many aspects of biodiesel and diesel combustion, especially the differences between them, which are not well understood. Often the experimental data is contradictory (Majewski and Khair, 2006). This suggests that fundamental studies are critical to understanding the combustion processes. When considering these inconsistencies, it is important to recognise two important factors:

1. Many of the studies are carried out on different engine types, such as road, marine, locomotive and even industrial engines. This changes a wide variety of variables that would affect the performance/emissions characteristics of biodiesel;
2. There is a wide difference in properties between biodiesel fuels made from different feedstocks. Considering blended biodiesel fuel mixtures increases the diversity of properties even further. This would undoubtedly affect the performance/emissions of engines. As can be seen, much work is needed in the area of understanding soot formation, biodiesel combustion, and the effects of biodiesel feedstocks on its combustion.

It is hoped that the work in this thesis will contribute to the development of models that can be employed to aid engine designers develop advanced diesel and biodiesel engines and interpret their performance results. In this regard, the literature review shows that there is no simplified model that is available for predicting soot formation in both petrodiesel and biodiesel sprays. In general, modelling studies of soot formation in biodiesel sprays are few whereas the literature is more extensive in petrodiesel sprays. Comparative studies between the two fuels are, however, primarily experimental in nature. This motivates the modelling studies presented in this thesis.

3 Computational Methods

3.1 Introduction

In this thesis work, two computational models, which were developed in-house using Fortran codes, are employed to achieve the objectives listed in the Introduction. The first is a one-dimensional flamelet model which solves the local unsteady one-dimensional equations for species and energy in a flame. This was used to achieve the first three objectives, listed in Section 1.1. This model will be discussed in Section 3.2. The second model, discussed in Section 3.2, is a multi-dimensional reciprocating engine model, which models non-reacting and reacting sprays in a domain. This was employed to achieve the remaining objectives of this thesis.

3.2 Flamelet Model

3.2.1 Theory

In non-premixed flames, such as those that exist in most regions of the reacting spray in direct-injected diesel engines, the flames are highly wrinkled and stretched due to turbulence. Such flames can be considered to be made up of multiple thin flamelets. However, the chemical process occurs as if it were in a strained laminar flame (Peters, 1984; Peters, 1986). This is due to the chemical timescale being much shorter than the turbulence timescale (Williams, 1985; Peters, 1986). Figure 3.1 illustrates the conceptual picture. Surrounding the spray are highly convoluted flames which appear like a brush in a spatially integrated picture (a), but appears like a highly-convoluted flame in a cross-section (b), which locally can be assumed to be a strained laminar flame (c). Figure 3.1(c) illustrates that the local flame can be modelled as a typical opposed-diffusion flame, where fuel and oxidiser react to form a flame front. The flame exists physically closer to the oxidiser at the stoichiometric mixture fraction. This flame can be modelled by one-dimensional equations for species and energy. This can be done under the following assumptions:

1. The Damkohler number is $\gg 1$. The chemical reaction timescale is considered orders of magnitude smaller than the turbulent mixing timescale.
2. The reaction zone thickness is smaller the Kolmogorov length scale of the characteristic length scale of the flow field. Thus, the reaction zone can be considered to be laminar and the flamelet to be one-dimensional.
3. The flow field can be assumed to be quasi-steady.

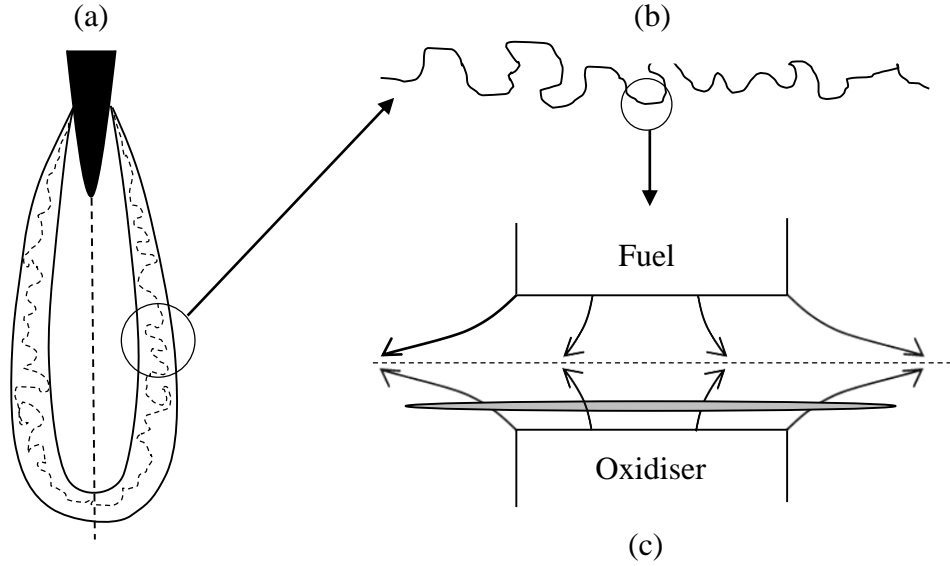


Figure 3.1: Conceptual illustration of flamelets.

3.2.2 Governing Equations

The species and enthalpy balance equations are respectively written as:

$$\rho \frac{\partial Y_i}{\partial t} + \rho v_\alpha \frac{\partial Y_i}{\partial x_\alpha} + \frac{\partial j_{i\alpha}}{\partial x_\alpha} = \dot{w}_i, \quad (3.1)$$

$$\rho \frac{\partial h}{\partial t} + \rho v_\alpha \frac{\partial h}{\partial x_\alpha} - \frac{\partial}{\partial x_\alpha} \left(\frac{\lambda}{c_p} \frac{\partial h}{\partial x_\alpha} \right) = - \frac{\partial}{\partial x_\alpha} \sum_{i=1}^n h_i \left(\frac{\lambda}{c_p} \frac{\partial Y_i}{\partial x_\alpha} + j_{i\alpha} \right) + \frac{\partial p}{\partial t} + \dot{q}_R, \quad (3.2)$$

where Y_i , ρ_i , h_i , λ_i and c_p are the mass fraction, partial density, specific enthalpy, thermal conductivity, and specific heat capacity of the i^{th} species, respectively. p is the pressure, $j_{i\alpha}$ is the diffusion mass flux of the i^{th} species in the x_α direction, \dot{w}_i is the chemical kinetics source term, \dot{q}_R is the power lost via radiation.

In the equations as written above, the Dufour and Soret effects are neglected to simplify the transport properties. Multicomponent diffusion by Fick's law is replaced by a single diffusion coefficient, under the assumption that the Lewis number was unity. This assumption is found to lead to reasonable results for hydrocarbon flames (Mukhopadhyay, 2011; Yen and Abraham, 2014). The diffusion is approximated as follows:

$$j_{i\alpha} = -\rho D \frac{\partial Y_i}{\partial x_\alpha}, \quad (3.3)$$

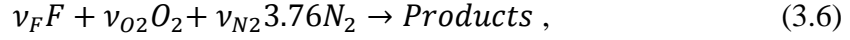
where D is the diffusivity and:

$$\rho D \equiv \frac{\lambda}{c_p}, \text{ due to } Le = 1, \quad (3.4)$$

The mixture fraction (Z) is defined as:

$$Z = \frac{Z_F}{Z_{F,1}} = 1 - \frac{Z_O}{Z_{O,2}}, \quad (3.5)$$

where 1 denotes the fuel source and 2, the oxidiser source in a two-feed system. Z_F and Z_O represent the mass fraction of all elements from the fuel and oxidiser stream, respectively. Thus, Z ranges from 0, for pure oxidiser, to 1, for only fuel. In a typical diesel engine, air is the oxidiser. Thus, for the reaction with air at 21 % oxygen volume fraction, i.e.



where ν_F , ν_{O_2} and ν_{N_2} are the reaction coefficients of the fuel species, oxygen, and nitrogen, respectively, the stoichiometric mixture fraction (Z_{st}) can be defined as

$$Z_{st} = \left[1 + \frac{\nu_{O_2} Y_{O_2} + 3.76 \nu_{N_2} Y_{N_2}}{\nu_F Y_F} \right]^{-1}, \quad (3.7)$$

where Y_F , Y_{O_2} and Y_{N_2} are the fuel, oxygen, and nitrogen mass fractions.

The concept of the mixture fraction can be applied to any chemical element as it is conserved:

$$Z_i = \sum_{j=1}^n \frac{a_{ij} M_j}{M_i} Y_j, \quad (3.8)$$

Equation (3.8) can be substituted into Eq. (3.1) to obtain a new operator based on Z_i :

$$L(Z_i) \equiv \rho \frac{\partial Z_j}{\partial t} + \rho v_\alpha \frac{\partial Z_j}{\partial x_\alpha} + \frac{\partial}{\partial x_\alpha} \left(\rho D \frac{\partial Z_j}{\partial x_\alpha} \right) = - \frac{\partial}{\partial x_\alpha} \sum_{i=1}^n \frac{a_{ij} M_j}{M_i} \left(\rho D \frac{\partial Y_i}{\partial x_\alpha} + j_{i\alpha} \right), \quad (3.9)$$

If Eq. (3.3) is considered, it can be seen that:

$$L(Z) = 0, \quad (3.10)$$

By applying the definition of enthalpy

$$h = \sum_{i=1}^n h_i Y_i, \quad (3.11)$$

$$dh = c_p dT + \sum_{i=1}^n h_i dY_i, \quad (3.12)$$

into Eq. (3.1)-(3.3), the following equation for energy can be derived:

$$L(T) = - \sum_{i=1}^n \frac{h_i}{c_p} \dot{w}_i + \frac{1}{c_p} \left(\frac{\partial p}{\partial t} + \dot{q}_R \right) + \sum_{i=1}^n \frac{c_{pi}}{c_p} \rho D \frac{\partial Y_i}{\partial x_\alpha} \frac{\partial T}{\partial x_\alpha} + \frac{\lambda}{c_p^2} \frac{\partial c_p}{\partial x_\alpha} \frac{\partial T}{\partial x_\alpha}. \quad (3.13)$$

The one-dimensional coordinate direction is assumed to be normal to the flame front. This is illustrated in Figure 3.2. Fuel enters the domain from the nozzle on the left, and oxidiser is entrained from the surroundings. The established visible flame contour is drawn in dotted lines and is usually lifted-off from the nozzle. The wrinkled line represents the thin stoichiometric reaction zone.

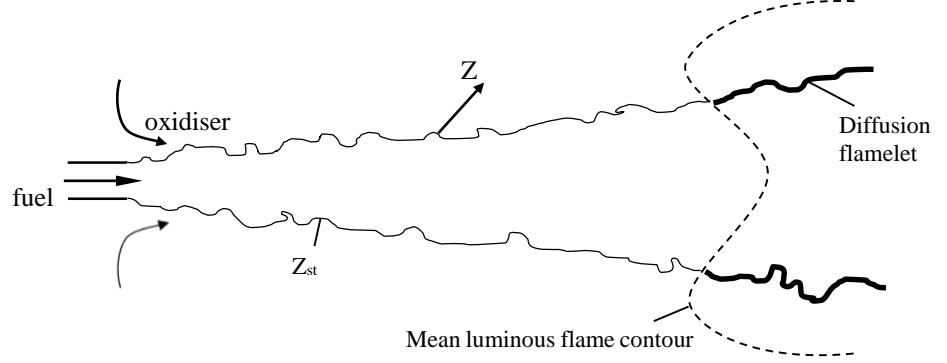


Figure 3.2: Conceptual drawing of diffusion flamelets.

Through a Crocco transformation (Schlichting and Gersten, 2000):

$$\frac{\partial}{\partial t} = \frac{\partial}{\partial \tau} + \frac{\partial Z}{\partial t} \frac{\partial}{\partial Z}, \quad (3.14)$$

where

$$\frac{\partial}{\partial x_1} = \frac{\partial Z}{\partial x_1} \frac{\partial}{\partial Z}; \quad (3.15)$$

thus

$$\frac{\partial}{\partial x_k} = \frac{\partial y}{\partial x_k} + \frac{\partial Z}{\partial x_k} \frac{\partial}{\partial Z}, \quad (k = 2, 3) \quad (3.16)$$

where $Z_2 = x_2, Z_3 = x_3, \tau = t$ as variables for the other two dimensions and time, respectively.

The equations for species and temperature become:

$$\rho \frac{\partial Y_i}{\partial \tau} = \rho D \left(\frac{\partial Z}{\partial x_\alpha} \right)^2 \frac{\partial^2 Y_i}{\partial Z^2} + \dot{w}_i - R(Y_i), \quad (3.17)$$

$$\rho \frac{\partial T}{\partial \tau} = \rho D \left(\frac{\partial Z}{\partial x_\alpha} \right)^2 \frac{\partial^2 T}{\partial Z^2} - \sum_{i=1}^n \frac{h_i}{c_p} \dot{w}_i + \frac{1}{c_p} \left(\frac{\partial p}{\partial t} + q_R \right) - R(T), \quad (3.18)$$

where R is defined as:

$$R = \left(v_2 \frac{\partial}{\partial Z_2} + v_3 \frac{\partial}{\partial Z_3} \right) - \frac{\partial(\rho D)}{\partial x_2} \frac{\partial}{\partial Z_2} - \frac{\partial(\rho D)}{\partial x_3} \frac{\partial}{\partial Z_3} - \rho D \sum_{k=2}^3 \left(2 \frac{\partial Z}{\partial x_k} \frac{\partial^2}{\partial Z \partial Z_k} + \frac{\partial^2}{\partial Z_k^2} \right). \quad (3.19)$$

The flamelet structure is defined by Eqs. (3.17)-(3.18). All terms containing Z_2 and Z_3 in Eq. (3.19) are low order compared to the first term on the right hand side of Eqs. (3.17)-(3.18). Thus, the unsteady flamelet equation can be reduced to:

$$\rho \frac{\partial \phi}{\partial t} = \rho D \left(\frac{\partial Z}{\partial x_\alpha} \right)^2 \frac{\partial^2 \phi}{\partial Z^2} + \dot{\omega}_\phi, \quad (3.20)$$

where ϕ denotes the vector of species mass fraction or temperature, and $\dot{\omega}_\phi$ represents their respective source terms. A new variable can be introduced to signify the effect of the flow field:

$$\chi = 2D \left(\frac{\partial Z}{\partial x_\alpha} \right)^2 = 2D \left[\left(\frac{\partial Z}{\partial x_1} \right)^2 + \left(\frac{\partial Z}{\partial x_2} \right)^2 + \left(\frac{\partial Z}{\partial x_3} \right)^2 \right], \quad (3.21)$$

where χ can be defined as the scalar dissipation rate can be interpreted as the inverse of a characteristic diffusion time. It has the unit of (s^{-1}). Equation (3.20) can be combined with Eq. (3.21) to obtain the following general unsteady flamelet equation:

$$\frac{\partial \phi}{\partial t} = \frac{\chi}{2} \frac{\partial^2 \phi}{\partial Z^2} + \dot{\omega}_\phi. \quad (3.22)$$

In mixing layers, χ may be assumed to be related to Z by an error function profile (Peters, 1984):

$$\chi = \chi_{st} \frac{\exp\{-2[\text{erfc}^{-1}(2Z)]^2\}}{\exp\{-2[\text{erfc}^{-1}(2Z_{st})]^2\}}, \quad (3.23)$$

where χ_{st} represents the scalar dissipation rate at the stoichiometric value. The mixture fraction coordinate is discretised into 51 grid points of varying density. The grid is densest near to the Z_{st} .

3.3 Multi-Dimensional Engine Model

The multi-dimensional engine spray studies are carried out in a Reciprocating Engine Code (REC), an in-house code where the Reynolds-averaged Navier-Stokes (RANS) equations are solved. The code is multi-dimensional and fully compressible. It employs a fully implicit finite volume method that is first-order accurate in time and second-order accurate in space (Magi, 1987). Spatial discretization is set up in moving orthogonal curvilinear coordinates. It has been previously employed for studies of hydrocarbon diesel sprays, including soot (Yen and Abraham, 2014; Bajaj et al., 2011; Bajaj et al., 2013). Turbulence is modelled using the standard k- ϵ model with boundary layers modelled using wall functions (Launder and Spalding, 1974;

Magi and Abraham, 2001). Liquid spray is modelled using the Lagrangian-Drop Eulerian-Fluid (LDEF) model (Dukowicz, 1980; O'Rourke and Bracco, 1980; O'Rourke, 1981). Turbulence/chemistry interactions are modelled using the unsteady flamelet progress variable (UFPV) model employed by Bajaj et al., (2013) which, in turn, is based on the earlier work of Ihme and See (2009).

Special consideration is needed when employing the LDEF model. It is only valid when the liquid volume fraction is less than 1% in computational cells. In addition, the drops need to be homogeneously distributed in the computational space. However, this is not possible in the region just after the nozzle. Thus, to get around this issue, computational cells that are larger than the nozzle diameter are typically employed. These grid sizes are not adequate to resolve the shear layer, and, not surprisingly, lead to results that are often inaccurate (Abraham and Pickett, 2010). The computational grid is shown in Figure 3.3. It is an axisymmetric 1° slice of a domain measuring 5 cm radially by 12 cm axially. The nozzle is located at the origin, and the grid expands away from the origin.

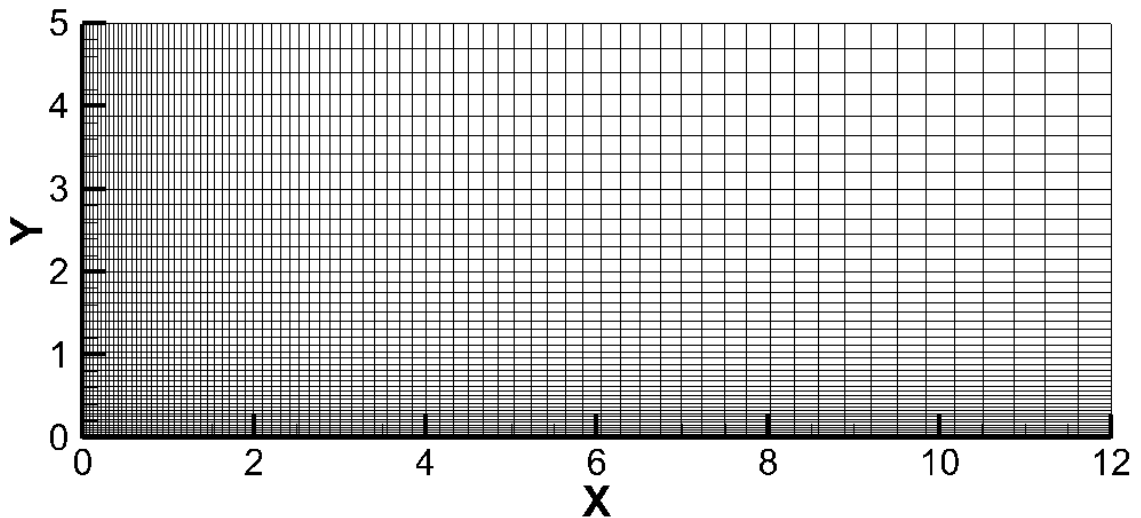


Figure 3.3: Computational grid used in REC.

3.3.1 Gas-phase Governing Equations

The governing equations for the gas-phase are modelled following the Eulerian conservation equations for mass, momentum, energy, species, and equation of state. The Reynolds-averaged equations are as follows:

Conservation of Mass

$$\frac{\partial \rho_g}{\partial t} + \nabla \cdot (\rho_g \mathbf{u}) = 0, \quad (3.24)$$

where \mathbf{u} is the Reynolds-averaged mean gas-phase velocity vector.

Conservation of Momentum

$$\frac{\partial(\rho_g \mathbf{u})}{\partial t} + \nabla \cdot (\rho_g \mathbf{u} \mathbf{u}) + \nabla p = \nabla \cdot \boldsymbol{\tau} , \quad (3.25)$$

where ρ_g is the gas-phase density, and $\boldsymbol{\tau}$ is the turbulent stress tensor. It is related to the strain rates by:

$$\boldsymbol{\tau} = \mu_e \left\{ \nabla \mathbf{u} - \frac{2}{3} (\nabla \cdot \mathbf{u}) \mathbf{I} \right\} + \rho_g k \mathbf{I} , \quad (3.26)$$

which is the linear Newtonian relation. In Eq. (3.26), \mathbf{I} is the identity matrix, k is the turbulent kinetic energy, and μ_e is the effective viscosity. It is defined as:

$$\mu_e = \mu_l + \mu_t , \quad (3.27)$$

where μ_l and μ_t are laminar and turbulent viscosities, respectively.

Conservation of Energy

The conservation of energy is:

$$\frac{\partial \rho_g h_g}{\partial t} + \nabla \cdot (\rho_g h_g \mathbf{u}) = \frac{\partial p}{\partial t} + \mathbf{u} \cdot \nabla p + \nabla \cdot [\lambda_e \nabla T_g] + \boldsymbol{\tau} : \nabla \mathbf{u} , \quad (3.28)$$

where h_g is the total

gas-phase enthalpy per unit mass, and λ_e is the effective thermal conductivity. It is defined as:

$$\lambda_e = \lambda_l + \lambda_t , \quad (3.29)$$

where λ_l and λ_t are the laminar and turbulent thermal conductivities, respectively. The Prandtl number is assumed to be unity.

Conservation of Species

For a species, i , the Reynolds-averaged conservation of species equation is:

$$\frac{\partial \rho_g Y_i}{\partial t} + \nabla \cdot (\rho_g Y_i \mathbf{u}) = \nabla \cdot [\rho_g D_e \nabla Y_i] + (\dot{\rho}_i)_{chem} , \quad (3.30)$$

where Y_i is the local mass fraction of species, i . D_e is the effective diffusivity, which is assumed to be the same for all species. $(\dot{\rho}_i)_{chem}$ is the rate of change of species partial density, ρ_i , due to

chemical reactions. The effective Schmidt number is assumed to be unity. Thus, the effective species diffusivity can be related to the effective viscosity by:

$$\rho_e D_e = (\rho_g D)_l + (\rho_g D)_t = \mu_e, \quad (3.31)$$

3.3.2 Turbulence Model

In the multi-dimensional engine model, the turbulence is modelled by the $k - \epsilon$ model (Launder and Spalding, 1974). The transport equations for turbulent kinetic energy and turbulent dissipation are:

$$\frac{\partial \bar{\rho} \tilde{k}}{\partial t} + \frac{\partial \bar{\rho} \tilde{u}_j \tilde{k}}{\partial x_j} = - \frac{\partial}{\partial x_j} \left[\frac{\bar{\rho} \nu_T}{\sigma_k} \frac{\partial \tilde{k}}{\partial x_i} \right] + 2 \bar{\rho} \nu_T \tilde{S}_{ij} \tilde{S}_{ij} - \bar{\rho} \tilde{\epsilon}, \quad (3.32)$$

$$\frac{\partial \bar{\rho} \tilde{\epsilon}}{\partial t} + \frac{\partial \bar{\rho} \tilde{u}_j \tilde{\epsilon}}{\partial x_j} = - \frac{\partial}{\partial x_j} \left[\frac{\bar{\rho} \nu_T}{\sigma_\epsilon} \frac{\partial \tilde{\epsilon}}{\partial x_i} \right] + C_{\epsilon 1} \bar{\rho} \nu_T \tilde{S}_{ij} \tilde{S}_{ij} - C_{\epsilon 2} \bar{\rho} \frac{\tilde{\epsilon}}{\tilde{k}}, \quad (3.33)$$

respectively, where turbulent viscosity, ν_T is defined as:

$$\nu_T = C_\mu \frac{\tilde{k}^2}{\tilde{\epsilon}}. \quad (3.34)$$

In Eqs. (3.32) - (3.34), the constants C_μ , σ_k , σ_ϵ , $C_{\epsilon 1}$, $C_{\epsilon 2}$ retain their standard values of 0.09, 1.00, 1.30, 1.44, and 1.92, respectively. The model has been applied in prior published studies and has been shown to reproduce measured engine spray results well (Bajaj and Abraham, 2013; Yen and Abraham, 2015).

3.3.3 Turbulence-Flame Interaction Model

REC employs the unsteady flamelet progress variable (UFPV) model to model the turbulence/chemistry interaction (Ihme and See, 2009). In the UFPV model, the chemical source terms are tabulated as a function of three independent parameters, the mixture fraction (Z), the scalar dissipation rate (χ), and a progress variable representing time (C). The chemical source terms are obtained from Eq. (3.22). C is based on temperature, and defined as:

$$C = \frac{T - T_u}{T_a - T_u}, \quad (3.35)$$

where the local temperature T , adiabatic flame temperature T_a , and unburned temperature T_u are dependent on the local mixture fraction Z . Note that tabulating the entries in the library as a function of all values of C at all values of Z generates a very large library. This need for

tabulation can be simplified if an assumption is made that $C(Z)$ can be characterized by the progress variable C_{st} at the stoichiometric mixture fraction. Unlike for χ , an analytical expression does not exist for the $C(Z)$ profile; but, this profile can be obtained from tabulated values of C as a function of Z . Hence, Z , C_{st} , and χ_{st} are the independent parameters in the library. The instantaneous source terms $\dot{\omega}_\varphi$ are tabulated as a function of these independent variables. As indicated earlier, because the simulations are based on the solution of the RANS equations, the averaged source terms are required. These are obtained by convolving the instantaneous variable with the joint probability density function (PDF) of the independent variables, i.e.

$$\tilde{\omega}_\varphi = \iiint \dot{\omega}_\varphi P(Z, C_{st}, \chi_{st}) dZ dC_{st} d\chi_{st}, \quad (3.36)$$

where $\tilde{\omega}_\varphi$ is the Favre averaged source term. In the implementation reported in the literature, the assumption is made that the PDFs of the independent variables are statistically independent of each other. This assumption has been assessed in detail in prior work (Ihme and See, 2010; Mukhopadhyay, 2011). Statistical independence converts the conditional PDFs into their respective marginal PDFs, i.e.

$$\tilde{P}(Z, C_{st}, \chi_{st}) = \tilde{P}(Z) \tilde{P}(C_{st}) \tilde{P}(\chi_{st}), \quad (3.37)$$

where presumed functional forms will be employed to approximate the shapes of the PDFs of the three variables Z , C_{st} and χ_{st} . The β -PDF is employed for Z and δ -PDFs for C_{st} and χ_{st} . In REC, the average scalar dissipation rate is defined as (Jones and Whitelaw, 1982):

$$\tilde{\chi} = C_\chi \frac{\tilde{\epsilon}}{\bar{k}} \tilde{Z}''^2, \quad (3.38)$$

where C_χ is a constant and \tilde{Z}''^2 is the variance of mixture fraction. Throughout this work, C_χ is taken to be 6.5 (Bajaj et al., 2013).

3.3.4 Pollutant Modelling

The formation and destruction of Nitric Oxides (NOx) via thermal, prompt and N₂O pathways are employed from the NO sub-mechanism of GRI-Mech 3.0 (Smith et al., 1999). The focus of this thesis will not be on NOx results. This is due to a lack of quantitative NO measurements in diesel sprays. Soot will be modelled in this body of work via a kinetic soot mechanism and two semi-empirical two-equation soot models. The kinetic mechanism is based

on the work of Appel et al. (2000) and consists of 101 species and 546 steps. It is based on the hydrogen-abstraction carbon-addition (HACA) mechanism, in which benzene (A1) progressively grows by surface addition of acetylene (C₂H₂) until pyrene (A4) is reached (Wang and Frenklach, 1994). (Please refer to Section 2.4.2 for more information.) Pyrene is the largest aromatic species in the kinetic mechanism. Beyond that, the method of moments is used to model the soot volume fraction and number density (Frenklach and Harris, 1986). The soot particle mass is defined as:

$$m_j = jm_1, \quad (3.39)$$

Where j is the number of mass units of each particle and m_1 is the smallest unit of mass in the particle. In the Appel et al. kinetic soot model, it is C₂, due to acetylene being the surface growth species. The number density, being the number of soot particles, is defined as (Gopalakrishnan and Abraham, 2004):

$$N_j = \frac{\rho Y_i}{W_j}, \quad (3.40)$$

where ρ is the density, and Y_i and W_j is the mass fraction and molecular mass of the species i , respectively. Distribution of soot particle sizes is statistically distributed as:

$$M_r = \sum_{j=1}^{\infty} j^r N_j, \text{ where } r = 0, \dots, \infty. \quad (3.41)$$

When $r = 0$, M_0 becomes Eq. (3.39) and is the soot number density. When $r = 1$, M_1 represents the total soot in units of m_1 per unit volume. From this, the soot volume fraction (f_v) can be obtained:

$$f_v = \frac{W_{C_2}}{\rho_{c(s)}} M_1, \quad (3.42)$$

where W_{C_2} is the molecular mass of C₂ and $\rho_{c(s)}$ is the density of soot (taken to be 1.8g/cm³ in this work).

3.3.5 Residence Time Tracking

Unlike temperature and species mass fractions that reach a quasi-steady state over time, soot mass can increase indefinitely over time. Thus, a method is required to track the residence of fuel that has entered into the spray domain. To achieve this, tracer particles are injected alongside the fuel to estimate a residence time for soot and NO calculation. The tracer particles

utilize the Lagrangian-drop Eulerian-fluid (LDEF) approach that is commonly used for sprays (Dukowicz, 1980; O'Rourke, 1981).

4 Biodiesel Feedstock Effects on Spray Structure

4.1 Introduction

In this section, the effects of biodiesel properties due to their feedstocks will be examined in non-reacting sprays. This will seek to answer whether the biodiesel produced from various regions of the world have an actual difference in typical diesel engine conditions. Section 4.2 describes the selection process of the biodiesel feedstocks and their properties. Section 4.3 shows the results of the feedstocks in liquid-phase penetration, vapour-phase penetration, and the mixture fraction distribution. It will also seek to explain the differences. This chapter will end with a summary and conclusion.

4.2 Feedstock Selection

The feedstocks chosen for this study correspond to those from the largest biodiesel production regions of the world. From the U.S. Energy Information Administration (EIA) (2015), these regions are, in descending production volume as of 2012: Europe, Central and South America, Asia and Oceania, and North America. Figure 4.1 shows the trend of increasing production quantity in these regions. The feedstocks selected are the most abundantly produced in that region: rapeseed oil (Europe), castor and sunflower oil (Central and South America), palm oil and tallow (Asia and Oceania), and soybean and corn oil (North America). This gives a wide spectrum of the most commonly produced sources of biodiesel fuels worldwide for comparison.

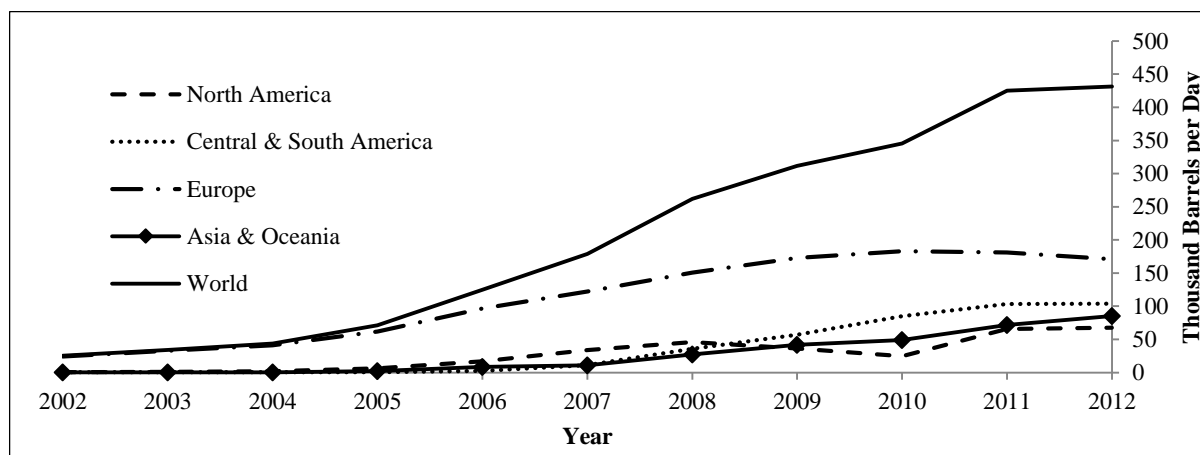


Figure 4.1: Biodiesel production by region.

Referring back to Table 1.2, it can be clearly seen that the proportion of fatty acid methyl esters (FAMES) differs for each feedstock. To compare the feedstocks in the spray, the properties of biodiesel fuel used are modified by changing various properties. A total of eight properties, and the resulting Sauter mean diameter (SMD), are altered. These changes will be elaborated.

4.2.1 Molar Mass, Critical Temperature, and Specific Heat

The molar mass for each feedstock is calculated by only considering the three most abundant FAMES. This represents roughly 90 % of the biodiesel feedstock by mass and is quite a sufficient approximation. Unless otherwise noted, this method will be employed for all remaining property estimations. Only the three major FAMES in each feedstock will be considered.

The critical temperature (T_c) is defined as the minimum temperature needed for a vapour of the substance to be impossible to liquefy. This is regardless how much pressure is applied to the substance. The T_c for each FAME is obtained from the work of Sales-Cruz et al. (2010). The T_c is seen to increase as the lipid chain length increases. Figure 4.2 illustrates this trend. Similar to the molar mass calculation, the T_c for the feedstock is the weighted average of the T_c of each of the three major FAMES.

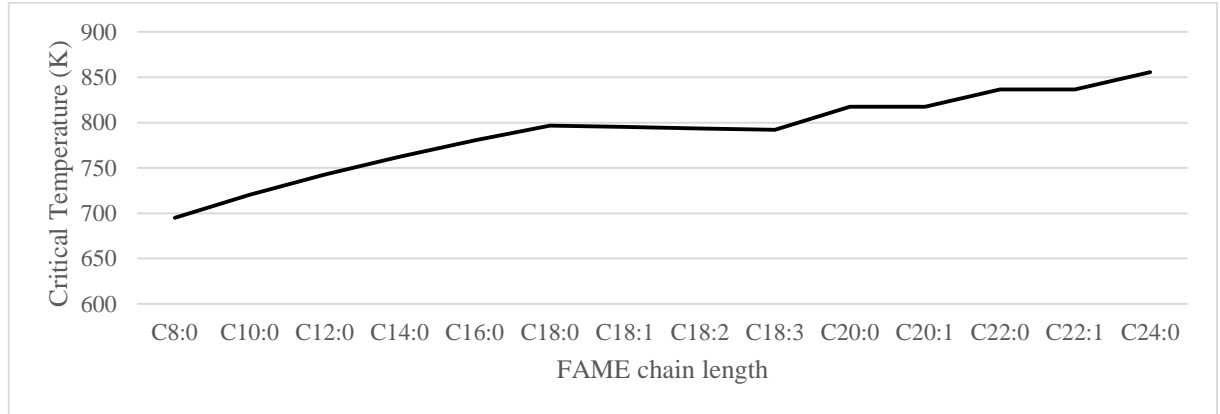


Figure 4.2: Critical Temperature (K) with respect to FAME chain length (Sales-Cruz et al., 2010).

The specific heat (c) is obtained for each FAME from the NIST Standard Reference Database (2015), and weight averaged to the three most abundant FAMES. Table 4.1 shows each feedstock being approximated to its three most major FAME components in terms of weight percentage. In the Table 4.1, C16:0 (palmitic acid) would represent a FAME with 16 carbon atoms, and 0 double bonds. FAMES not seen in Table 4.1 represent a minority proportion in the feedstock, and are not considered in the property estimations. It also shows approximated the molar mass, critical temperature, and specific heat.

Table 4.1: Each of the seven feedstocks approximated (weight %) to be consisting of the three major FAMES.

	C16:0	C18:0	C18:1	C18:2	C22:1	Molar Mass	Critical Temperature (K)	Specific Heat (J/g)
Soybean	0.119		0.259	0.623		279.7	792.5	2.16
Rapeseed			0.255	0.151	0.586	314.1	812.4	2.07
Beef tallow	0.270	0.221	0.563			292.7	834.2	2.40
Corn	0.103		0.335	0.654		306.1	865.7	2.34
Palm	0.475		0.422	0.103		271.4	788.0	2.38
Sunflower		0.0479	0.174	0.778		282.5	794.1	2.1
Castor	0.0141		0.936	0.0496		283.5	794.9	2.058

4.2.2 Vapour Pressure

The vapour pressure of a substance represents its tendency, usually measured in kPa, to vaporise at a certain temperature. The work of Yuan et al. (2005) was referenced for the vapour pressure. These were weight averaged and fitted to the Antoine equation (1888):

$$\log(P_v) = A - B/(T + C), \tag{4.1}$$

where P_v represents the vapour pressure, T is temperature in Kelvin, and A , B , and C are constants. Figure 4.3 shows the logarithmic vapour pressure (kPa) measured against inverse of temperature. As can be seen, the vapour pressures of all seven feedstocks are quite similar. The only major outlier is rapeseed, which has a much lower vapour pressure at low temperatures. However, such temperatures are unlikely to be encountered in a typical diesel engine.

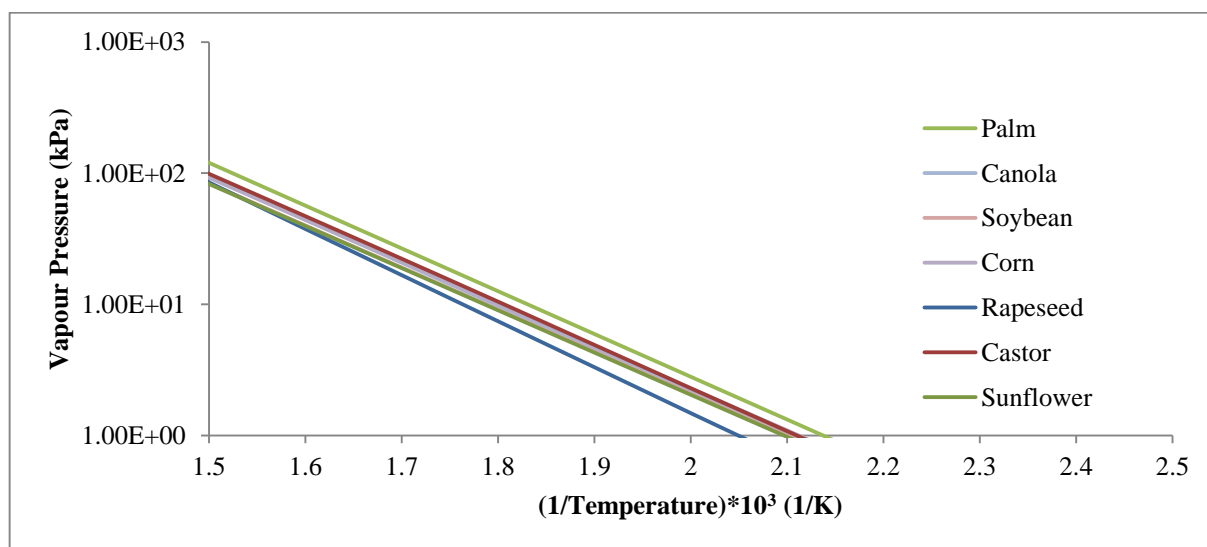


Figure 4.3: Log-scale vapour pressure (kPa) with respect to (1/T). Data taken from Yuan and Hansen (2005).

4.2.3 Thermal conductivity

For thermal conductivity (k), Ullmann's Encyclopedia of Industrial Chemical (Annaken, 2011) is sourced. It decreases with increasing temperature, but overall, larger FAMEs have higher conductivity. Figure 4.4 shows this relationship. As there was no data for C₂₂ FAMEs, the thermal conductivity for the C₂₂:1 FAME was extrapolated.

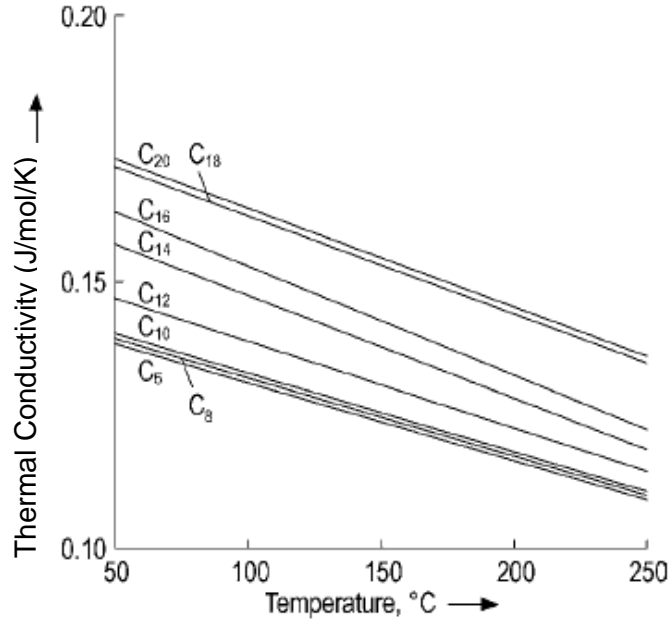


Figure 4.4: Thermal conductivity for FAMEs plotted against temperature (Annaken, 2011).

4.2.4 Liquid Density

Similar to thermal conductivity, data was taken from Ullmann's Encyclopedia of Industrial Chemical (Annaken, 2011). The density was seen to decrease with increasing temperature and larger FAMEs had lower overall density. Figure 4.5 shows the relationships.

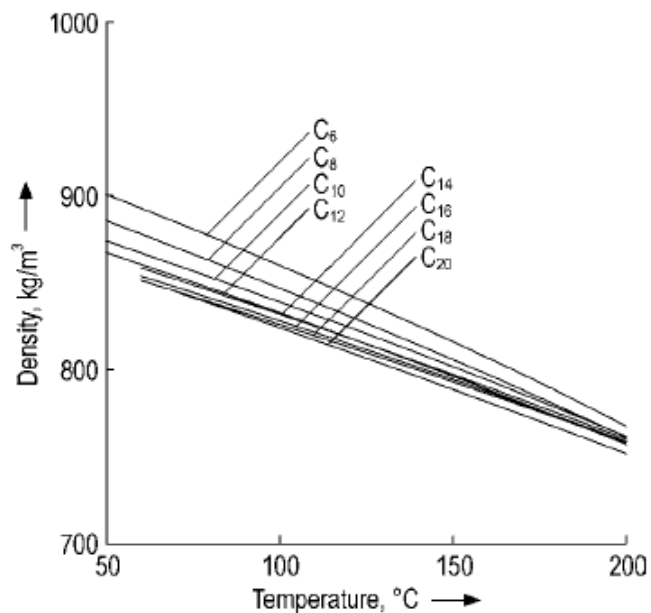


Figure 4.5: Liquid density of FAMEs with respect to temperature (Annaken, 2011).

4.2.5 Viscosity

Ullmann's Encyclopedia of Industrial Chemical (Annaken, 2011) is sourced for dynamic viscosity of each FAME. An exponential curve fit was derived for each curve, and viscosity of the three major FAMES were extracted. Figure 4.6 presents the relationship of viscosity with temperature and FAME size. In general, the viscosity decreases with temperature exponentially and converges at very high temperatures. And as expected, the larger the FAME, the greater the viscosity.

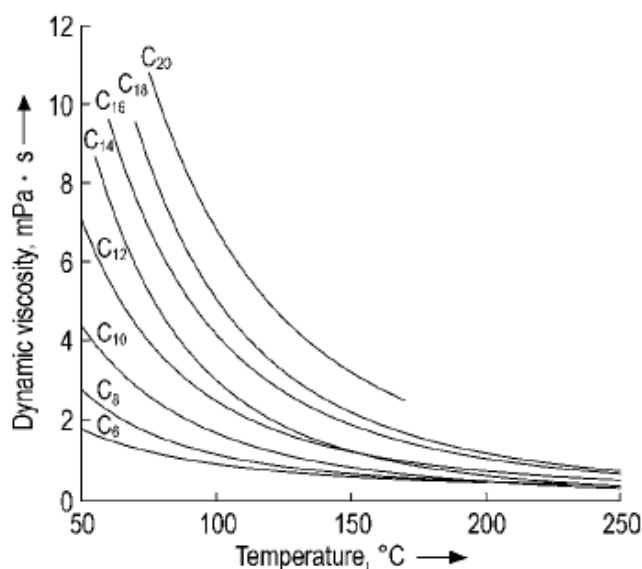


Figure 4.6: Dynamic viscosity of FAMES with respect to temperature (Annaken, 2011).

As these properties vary greatly with temperature, a curve fit is derived for each feedstock based on the curves of each FAME.

4.2.6 Surface Tension

Finally, the surface tension was also considered to differentiate between each feedstock. As temperatures increased, the surface tension decreased linearly. Larger FAMES had generally higher surface tension at each temperature point. Similar to dynamic viscosity, a linear curve-fit was applied to the major FAMES of each of the seven feedstocks. This was then used to determine the estimated surface tension of each feedstock.

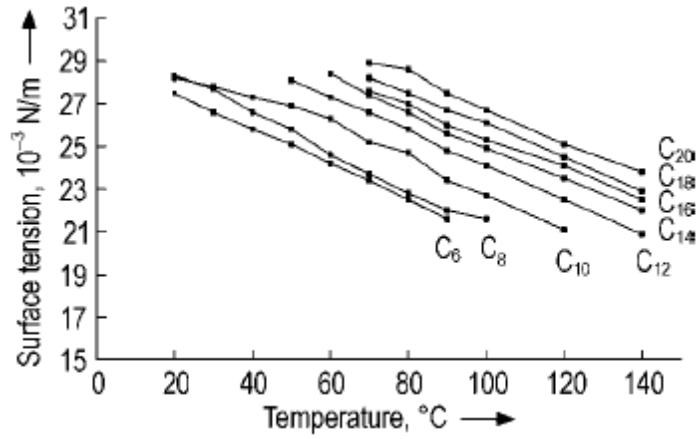


Figure 4.7: Surface tension of each FAME with respect to temperature (Annaken, 2011).

4.2.7 Sauter Mean Diameter

The Sauter mean diameter (SMD) defines an average particle size in a typical spray. It is seen as combination of the properties mentioned in Sections 4.2.1 – 2.2.6. In this work, it is determined based on the equation derived by Elkotb (1982):

$$SMD = 3.08v^{0.385}(\gamma\rho_l)^{0.737}\rho_a^{0.06}\Delta P^{-0.54}, \quad (4.2)$$

where v is the kinematic viscosity, γ is the surface tension, ρ_l and ρ_a are the fuel and air densities, respectively, and ΔP is the injection pressure. In this work, the SMD will vary in ratio with respect to that of soybean, which, has been given a reference SMD of 1 micron. This value of SMD is typical of that of diesel sprays injected at a pressure of 150 MPa into a constant-volume chamber (Abraham and Pickett, 2010).

4.3 Results and Discussion

The results will be presented in three parts below: the liquid penetration, vapor penetration and mixture fraction distribution. For this study, the conditions follow that of those employed in the work of Nerva et al. (2012). The ambient density is 22.8 kg/m^3 , nozzle diameter is $90 \text{ }\mu\text{m}$, injection pressure 150 MPa, and injection duration is 4 ms. Biodiesel fuel is injected at 363 K, and diesel fuel at 373 K. Two ambient temperatures will be tested, 900 K and 1000 K. The only changes considered are in the biodiesel fuel properties to match the various feedstocks.

4.3.1 Liquid-phase Penetration

Figures 4.8(a) and (b) show the computed liquid penetration for the various fuels when the chamber temperature is 900 K and 1000 K, respectively. For reference, the measured data of Nerva et al. (2012) for soybean biodiesel fuel is also shown. In the 900 K case, the measured

liquid penetration of biodiesel from the work of Nerva et al. (2012) stabilized at around 2.1 cm downstream of the nozzle. In the computations, the soybean biodiesel penetration stabilized at around 1.9 cm, which is within 10 % of the measured data. At 1000 K, the corresponding values are 1.67 cm (measured) and 1.5 cm (computed).

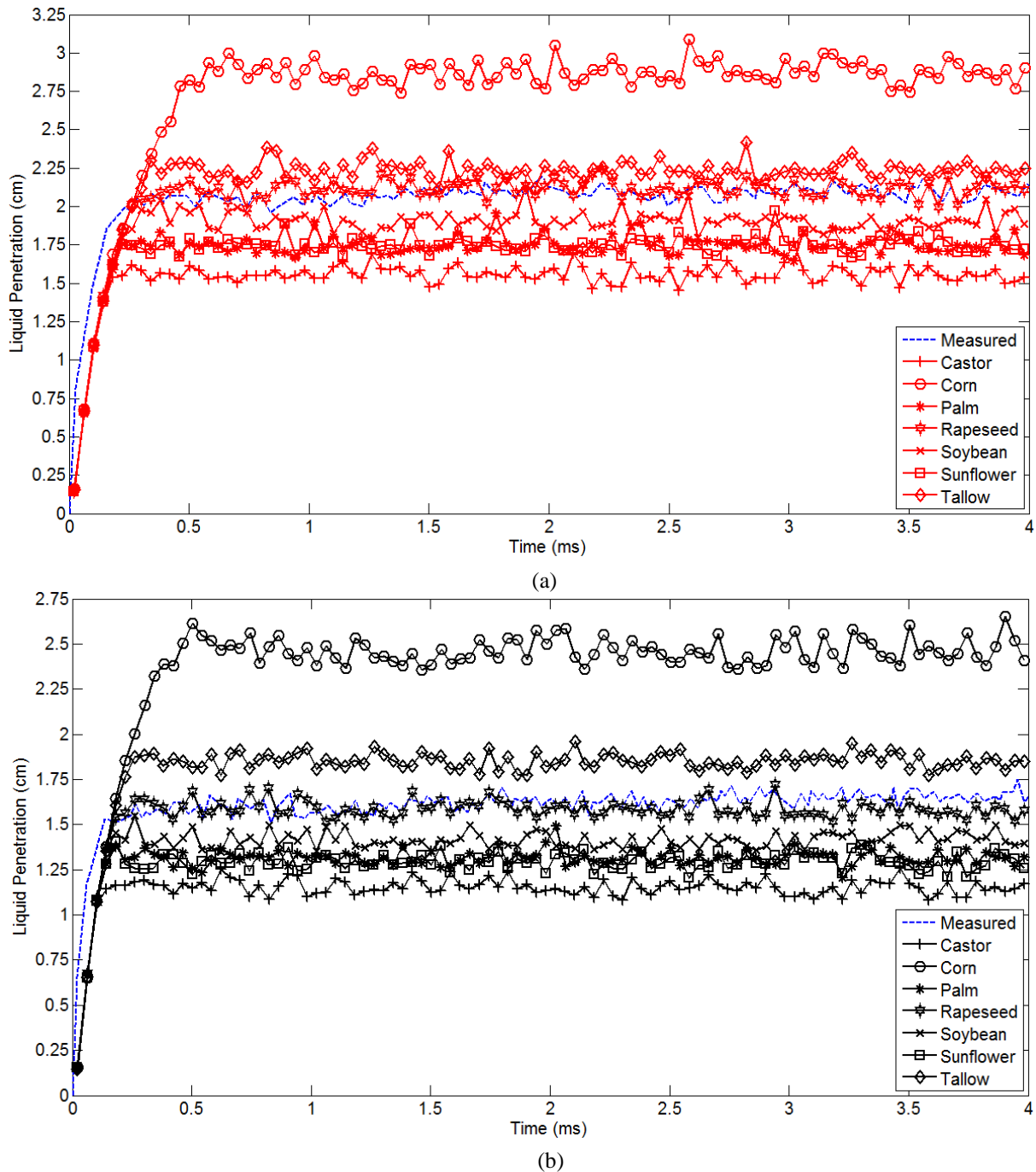


Figure 4.8: Liquid penetration of the biodiesel fuels and the soybean-derived biodiesel measurement from Nerva et al. (2012). Ambient temperature of 900 K (a) above, 1000 K (b) below.

At both temperatures, a similar order can be seen in terms of liquid-phase penetration. In descending order of penetration distance, it is: corn, tallow, rapeseed, soybean,

palm/sunflower, and castor. The liquid penetration distance of palm-derived biodiesel is about the same as that of sunflower-derived biodiesel to differentiate conclusively. Part of the explanation for the greater penetration of the corn-derived biodiesel may be the larger Sauter mean diameter (SMD) of 1.175 μm , but the SMD of tallow, rapeseed, soybean and sunflower are within 5 % of each other and their penetrations are different, so that cannot explain their differences. Note from Eq. (4.2) that the SMD is influenced by several factors including the injection velocity. In addition, it is generally accepted that in sprays under engine conditions, entrainment rate is a controlling factor for liquid penetration, rather than the SMD (Siebers, 1998; Iyer et al., 2000). The injection velocities of the various fuels in descending order are (in m/s): rapeseed (661.5), soybean (655.7), sunflower/castor (655.2), palm (654.5), tallow (621.4) and corn (600.6). These differences in injection velocity result in differences in momentum injection rate which, in turn, influence the entrainment rate.

Figure 4.9 shows the vapour pressure in kPa of the seven biodiesel fuels with respect to temperature (K). The vertical axis is in log scale. An inset table lists the vapour pressure of the biodiesel fuels at certain temperatures, their mean vapour pressure, and the standard deviation at each temperature case. It shows, for example, at around 500 K, rapeseed having the lowest tendency to vaporise and palm the most. From the inset table, it can be seen that the deviation of the vapour pressures from the mean is substantial. From the four sample temperatures, the coefficient of variation is about the same, showing the vapour pressure remains as varied across these temperatures. Even though tallow-sourced biodiesel has the highest vapour pressure in three of the four temperature cases, it does not have the shortest liquid penetration showing that the effect of feedstock vapour pressure on liquid-phase penetration is not dominant.

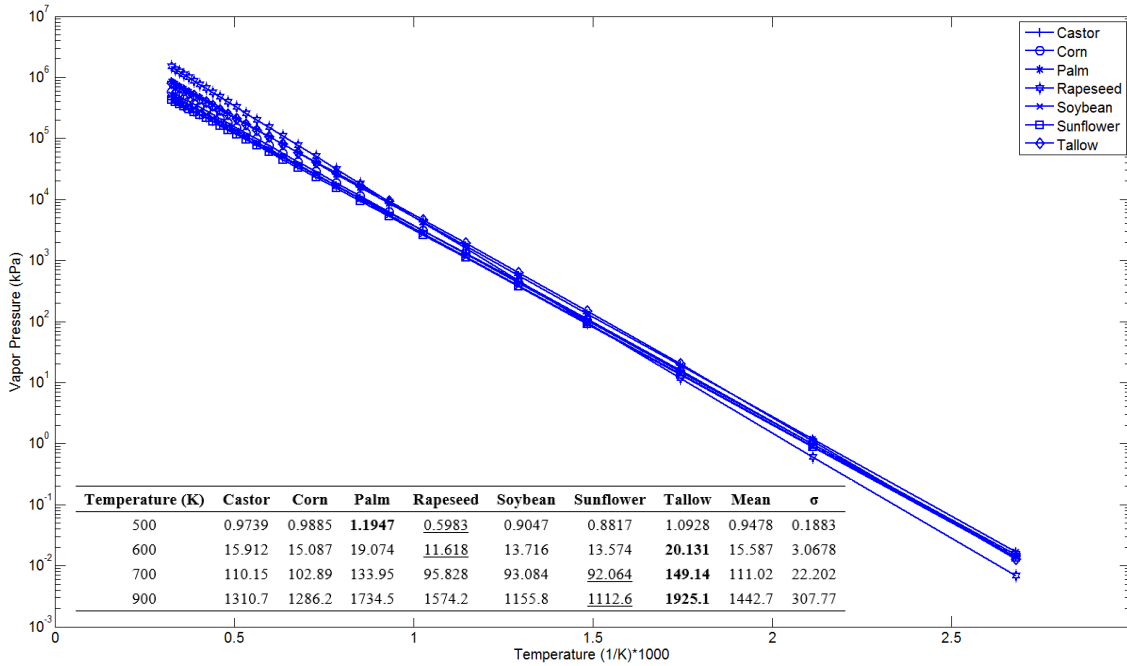


Figure 4.9: Vapour pressure of the biodiesel fuels. Vertical axis is in log-scale. Temperature equivalent ranges from 373.15 K to 3073.15 K. Vapour pressure (kPa) at selected temperatures (K) shown in the inset table, along with the mean and standard deviation.

Based on the observations above, a table can be generated to conveniently compare the spray properties of the seven fuels. This is shown in Table 4.2, and is arranged in descending order of liquid penetration distance. Recall from Fig. 4.8 that the liquid penetration distance of palm-derived biodiesel and sunflower-derived are very similar.

Table 4.2: Some of the properties employed in the spray calculations.

Feedstock	Injection Velocity (m/s)	Vapour Pressure (kPa @ 500 K)	Sauter-Mean-Diameter (μm)
Corn	600.6	0.9885	0.889
Tallow	621.4	1.0928	1.175
Rapeseed	661.5	0.5983	0.861
Soybean	655.7	0.9047	0.997
Sunflower^a	655.2	0.8817	1
Palm^a	654.5	1.1947	0.978
Castor	655.2	0.9739	0.966

^aLiquid penetration distance of sunflower and palm biodiesel are similar.

As mentioned above, even though the liquid penetration of corn biodiesel could be associated to the higher SMD, it should be associated to the low injection velocity, instead. Due to the low injection velocity, the mass of air entrained is lower, reducing vaporisation. The same can be stated regarding tallow, which has the second lowest injection velocity. Rapeseed-derived biodiesel should have a much shorter liquid penetration due to having the highest exit velocity. However, the relatively low vapour pressure causes the liquid penetration to lengthen. The exit velocity of soybean, palm, sunflower, and castor-derived biodiesel are very similar, so are the properties of vapour pressure and SMD. As such, these fuels' liquid

penetration are bunched together at around 10 % of each other in both temperature cases. It can be seen that, in general, the factors that influence liquid penetration are, in decreasing order of importance: entrainment rates brought on by injection momentum, vapour pressure, and SMD. However, as the liquid penetration distance is relatively short compared to the engine cylinder radius, the impact of the differences in liquid penetration on spray penetration beyond the liquid length is not expected to be significant.

4.3.2 Gas-phase Penetration

In a typical diesel engine, the injected fuel vaporises rapidly as a result of the high entrainment rate of the hot ambient air. As seen from Fig. 4.8, the fuel becomes fully vapour within about 3 cm of the orifice for an ambient temperature of 900 K, and 2.5 cm for 1000 K. Figure 4.10 shows the vapour penetration as a function of time for the fuels. These values were obtained by considering the farthest axial distance with a mixture fraction value of 0.0025. Computed results for ambient temperatures of 900 K and 1000 K, the measured results of Nerva et al. (2012), and an analytical result are shown. As evident, the vapour penetration of the various fuels collapse to within 10 % of the analytical vapour penetration curve (Bajaj et al., 2011), which is defined as:

$$x_{pen}^2 = 5.796 d (\rho_l / \rho_\alpha)^{0.5} U_i t, \quad (4.2)$$

where d is the diameter of the nozzle, ρ_l and ρ_α are the fuel and ambient gas density, respectively, U_i is the injection velocity, and t is time. Expressing the injection velocity in terms of injection pressure results in:

$$x_{pen}^2 = 5.796 d (2\Delta P / \rho_\alpha)^{0.5} t, \quad (4.3)$$

which shows that vapour penetration is only dependent on nozzle diameter, injection pressure and ambient density. Thus, the type of biodiesel feedstock does not factor into the analytical expression for vapour penetration.

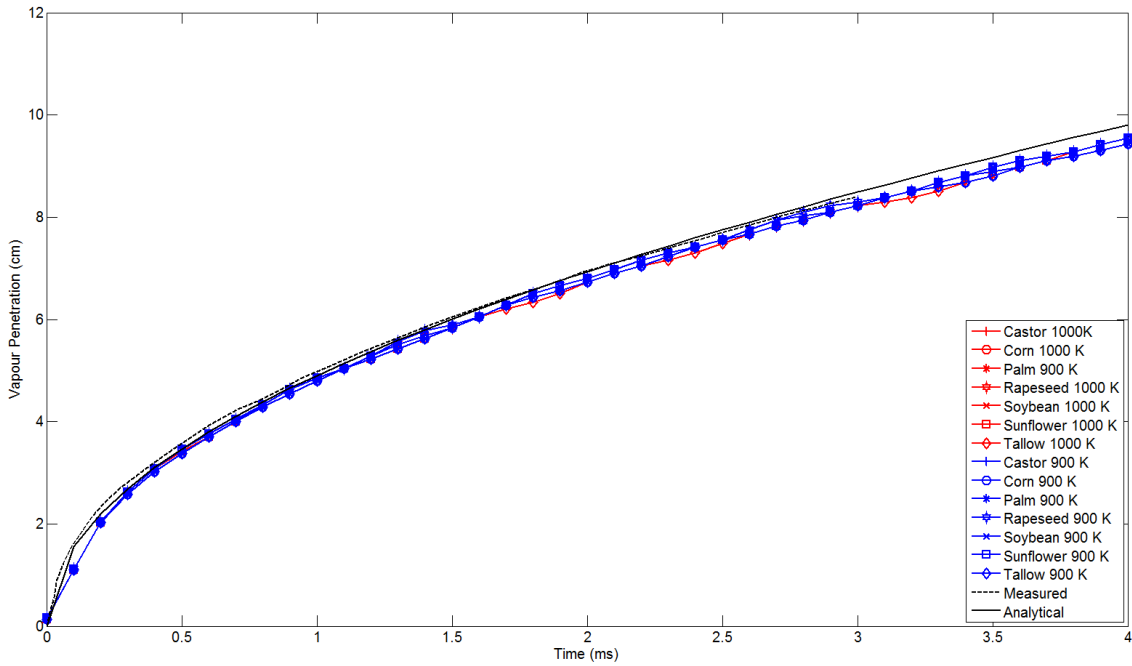


Figure 4.10: Vapour penetration of the biodiesel fuels compared to the soybean-derived measurement from Nerva et al. (2012) and an analytical curve.

In reality, changes in injection pressure for different liquid fuels and vaporisation rate will affect the penetration. The results suggest that the vaporisation rate effects are relatively small. Also, the quantity of the various fuels injected may vary in an engine to compensate for differences in density and heating value. These differences will influence the actual penetration.

4.3.3 Mixture Fraction Distribution

Figure 4.11 shows the mixture fraction (Z) contours for the various fuels at 900 K (a) and 1000 K (b). The contours in both temperature cases are arranged (1) – (7) in alphabetical order: castor, corn, palm, rapeseed, soybean, sunflower, and tallow. The lower Z cut-off is 0.0025. There are no noticeable differences from one fuel to the other. This is consistent with the results of Fig. 4.10.

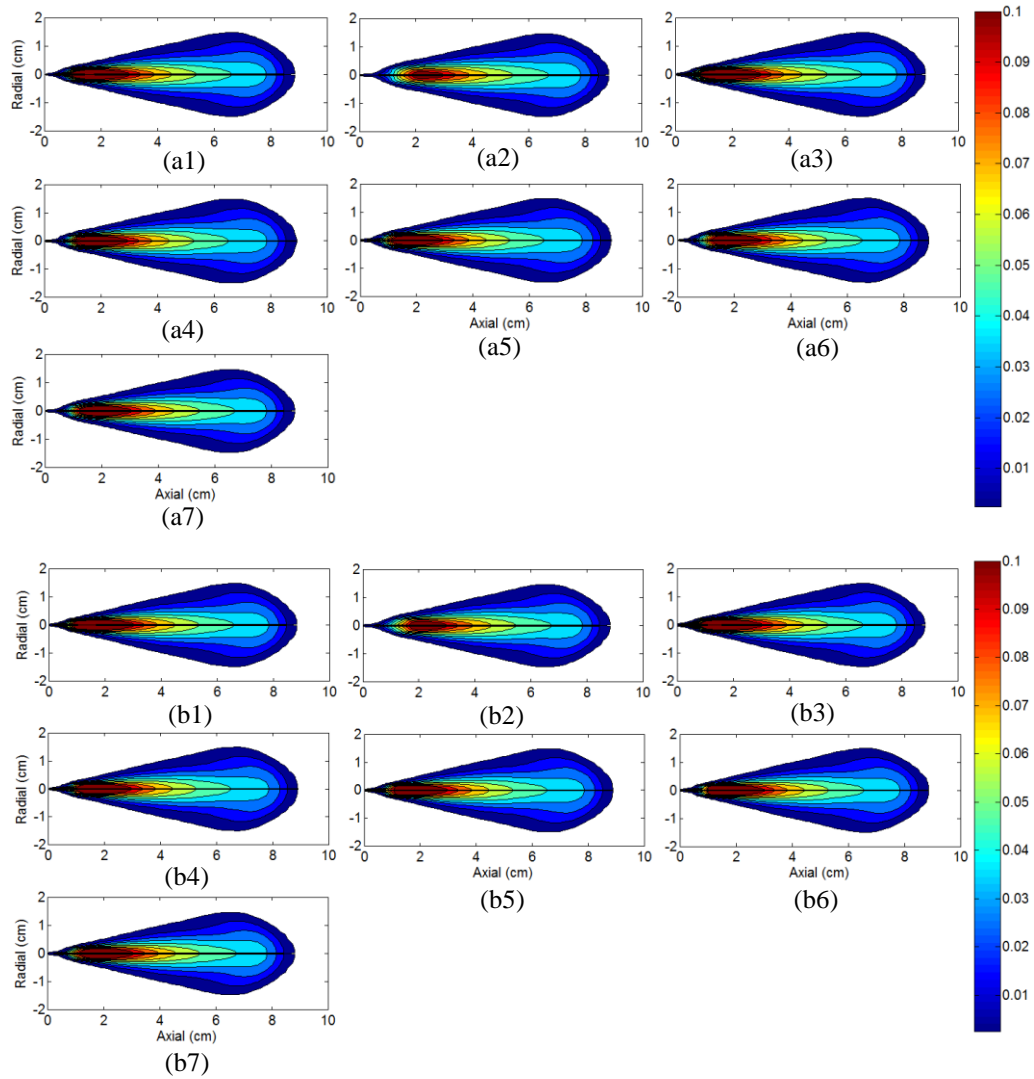


Figure 4.11: Mixture fraction contours of the biodiesel fuels at 4 ms after the start of injection. 900 K cases (a) above and 1000 K cases (b) below. Feedstocks: castor, corn, palm, rapeseed, soybean, sunflower and tallow represented by (1) to (7).

Lower cut-off fo

At this point in time, it would be useful to study the effect of various fuels on pollutant formation and flame structure. Unfortunately, chemical kinetics mechanisms for biodiesel fuels derived from various feedstocks are not available. What would be required to carry out the study are chemical mechanisms for each FAME that could model its chemical oxidation process accurately and with computational economy. The mechanisms currently available are for biodiesel surrogates which do not represent biodiesel from any one feedstock.

4.4 Summary

In this study, non-reacting sprays of biodiesel fuel sourced from seven feedstocks and injected into a constant-volume chamber are modelled. The injection and chamber conditions are representative of biodiesel engines. There are significant differences in the liquid-phase penetration for the fuels on account of differences in entrainment rate, vapour pressure, and SMD, in that order. The vapour phase penetrations and the mixture fraction distributions of the

various fuels show negligible differences. This study has not explored the effect of differences in oxidation kinetics on reacting sprays and pollutant formation because of the lack of availability of feedstock-dependent chemical kinetics mechanisms.

5 Limit Phenomena

5.1 Introduction

In this chapter, *limit phenomena*, i.e. *ignition* and *extinction*, of fuels is explored for diesel and biodiesel fuels. Section 5.2 discusses the importance of this in terms of the diesel engine. The influence of the limit phenomena on the formation of pollutants will be shown in Section 5.3. Finally, this chapter will end with a summary.

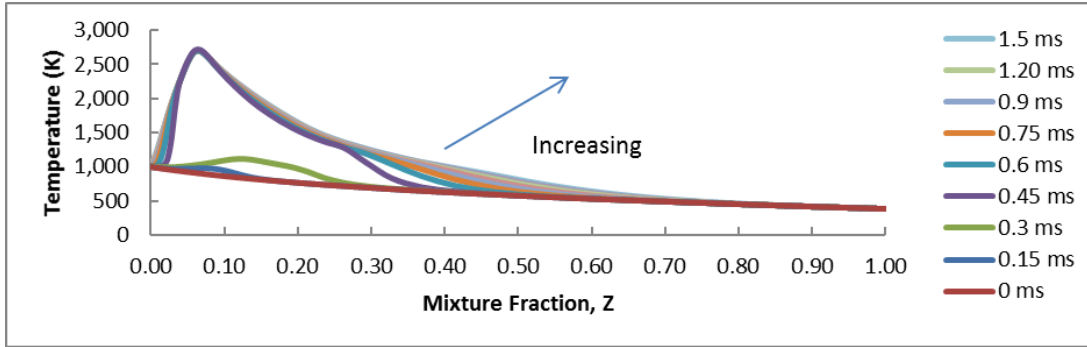
5.2 Background

The limit phenomena of ignition and extinction of the flame are important in compression ignition (CI) engines where turbulence generates a range of strain rates, be it due to the high pressure injection of fuel, piston motion, or air exchange. Ignition is not likely to occur in regions of high turbulent strain. If a diffusion flame already exists, they are likely to be extinguished by high strain rates. The strain rates below which ignition can occur is referred to as an ignition strain rate and the rate above which extinction occurs is referred to as the extinction strain rate. Please see Section 2.2 for a more detailed explanation.

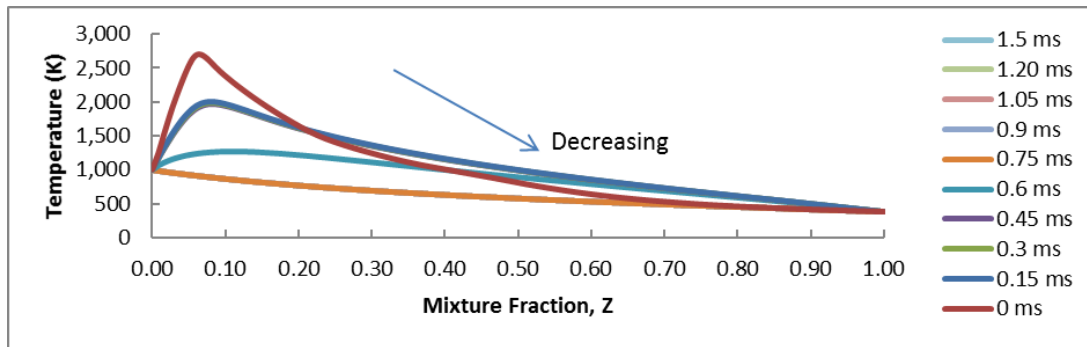
In this study, scalar dissipation rates (χ) will be employed rather than strain rates because the equations solved are the flamelet equations (see Section 3.2). The one-dimensional flamelet model, named Diffusion Laminar Flamelet Code (DLFC) is employed. The setup in mixture fraction (Z) space has boundary conditions of 1000 K at $Z = 0.0$ (air) and 373 K at $Z = 1$ (fuel). The pressure is selected to be constant at 40 bar. These conditions are typical of that in diesel engines. The numerical timestep is 5×10^{-7} s, which is found to be a sufficient balance between computational economy and accuracy. The Z -space is discretised into 51 non-uniform grid points with a higher density of points close to the stoichiometric mixture fraction (Z_{st}). The χ is assumed to have an error-function profile which would be close to that obtained in a mixing layer. The subsequent reference to χ is to the stoichiometric value of χ , i.e. χ_{st} .

Figure 5.1 shows the time evolution temperature profiles in Z space for (a) χ of 59 s^{-1} and (b) χ of 1542 s^{-1} , over a course of 1.5 ms. The diesel fuel surrogate used is a 37-species n-heptane kinetics mechanism (Peters et al., 2002). In that study, the ignition delay of the mechanism was matched very well to that of experiments at pressures of 3, 13.5 and 42 bar. In addition, the profiles of temperature, fuel, and other critical species were studied extensively. At the start of Figure 5.1(a), the temperature profile reflects the initial boundary condition profile. At 0.15 ms, there is evidence of ignition as the peak temperature rises above 1,000 K. By 0.45 ms, full ignition has occurred and the peak temperature close to Z_{st} has reached a

steady value. As a result of heat diffusion, the temperature rises at progressively higher values of Z until a steady profile is reached at about 1.5 ms. At a χ of 59 s^{-1} , this is the maximum χ where auto-ignition is possible, and is deemed the ignition χ , χ_{ign} . Beyond that, the flame will not ignite. In the DLFC code, the ignition limit is found by specifying a sufficiently large χ and reducing χ until auto-ignition occurs.



(a)



(b)

Figure 5.1: Temperature evolution of a diesel surrogate, n-heptane, at (a) χ of 59 s^{-1} , and (b) χ of 1542 s^{-1} .

The extinction χ , χ_{ext} , is the χ at which an existing flame is extinguished. For practical purposes, a temperature cut-off value may be employed. In other words, if the peak steady temperature is below the cut-off value, extinction may be assumed to have occurred. In the DLFC code, this limit is found by first creating a stable flame with a low χ , say 5 s^{-1} , and then using the result as an initial condition for subsequent simulations with progressively increasing values of χ . Figure 5.1(b) shows the time evolution of temperature at the χ_{ext} of $1,542 \text{ s}^{-1}$. At a time of 0.15 ms after the χ is imposed, the peak temperature value decreases. By 0.6 ms, the peak temperature has decreased to a value lower than 1,500 K and by 0.75 ms the flame is completely extinguished. Similar to the χ_{ign} , the χ_{ext} of $1,542 \text{ s}^{-1}$ implies that upon reaching this level of strain (and beyond), the flame extinguishes. Table 5.1 lists the χ_{ign} and χ_{ext} , for the two surrogates, with different mechanisms. Appendix A gives a further discussion of the different fuel mechanisms in terms of adiabatic flame temperature and laminar flame speed.

Table 5.1: Ignition and extinction limits for the fuel surrogates.

Fuel	Surrogate Mechanism	$\chi_{\text{ext}} \text{ (s}^{-1}\text{)}$	$\chi_{\text{ign}} \text{ (s}^{-1}\text{)}$	Reference
Diesel	37-species	1542	59	Peters et al., 2002
	44-species	7000	42	Liu et al., 2004
	160-species	4375	188	Seiser et al., 2000
	561-species	2500	125	Curran et al., 1998
Biodiesel	115-species	2500	37	Luo et al., 2012
	214-species	2500	50	<i>This work</i>

As can be seen, not only is the χ_{ign} and χ_{ext} different between the two fuels, it also differs between each surrogate mechanism. This makes it difficult to categorise a specific limit for each fuel, and it makes comparisons challenging.

5.3 Influence of Strain on Pollutants

The two pollutants of greatest interest in compression-ignition engines are soot and NO_x . Pollutant chemistry is discussed in detail in Section 2.4. The formation of these pollutants is influenced by turbulence characteristics, in addition to thermodynamic parameters. Increasing turbulence in an engine increases turbulent strain, which increases mixing. Hence, strain is indirectly related to mixing. Higher strain rate results in higher χ . This implies that the greater the turbulence, the greater the strain, the greater the χ , the faster the rate at which scalar non-uniformities are dissipated. It is expected that increasing χ will decrease the soot formation and increase soot oxidation although the precise trends are likely to depend on the range of values of χ . In this section, the influence of χ on soot and NO distribution in mixture fraction space will be examined. A soot mechanism and NO mechanism will be added to the primary fuel mechanisms studied above. The soot mechanism employed is the mechanism developed by Appel et al. (2000), and discussed in detail in Section 2.4.2. Henceforth, it will be referred to as the ABF soot mechanism, after the authors. The 19-species NO kinetics mechanism is taken from the GRI-Mech 3.0 mechanism (Smith et al., 1999). These pollutant mechanisms are both added to a petrodiesel and biodiesel fuel surrogate mechanism. For the petrodiesel surrogate, the 160-species n-heptane mechanism is chosen (Seiser et al., 2000). This choice was due to two reasons: Firstly, it is a well validated petrodiesel surrogate mechanism in many studies (Liu et al., 2004; Venugopal and Abraham, 2007). Secondly, its size offers a good balance between computational economy and support for the ABF soot mechanism. For the biodiesel surrogate, a 115-species tri-component mechanism is chosen (Luo et al., 2012). Its fuel component consists of n-heptane, methyl decanoate, and methyl-9-decenoate in a ratio of

2:1:1. Henceforth, it shall be referred to as the TBS mechanism, for “Ternary Biodiesel Surrogate”. This mechanism is well studied and known to give accurate predictions of ignition delay and product mass fractions. In total, including the two pollutant mechanism, the petrodiesel surrogate mechanism consists of 253 species and the biodiesel surrogate mechanism has 214 species. To simply, the former shall be denoted as “HEP253” and the latter “TBS214”. Some species are removed as they are duplicates.

Unlike the species in the primary fuel mechanism which reach steady concentration values within 1-2 ms after ignition, the concentration of the soot precursors and soot do not reach steady values for the durations of interest in compression-ignition engines. In addition, ignition delay is dependent on χ . Thus, if the sample time for recording soot production starts from 0 s, it would include the time taken for autoignition. The computations are, as a result, run with a numerical timestep of 5×10^{-7} s for a total time of 3 ms. The output is logged every 10 μ s to accurately capture the autoignition process. Soot production is recorded from the time when the peak temperature has reached 1,500 K, meeting the criteria for auto-ignition. An extra 1.5 ms is added to this time and the volume fraction of soot, f_v is recorded. To illustrate: The HEP253 mechanism only reaches a peak temperature of 1,500 K at 0.43 ms. Thus, the soot volume fraction will be taken 1.5 ms after this, i.e. at 1.93 ms. The initial conditions are a temperature of 1000 K for air ($Z = 0$), 373 K for fuel ($Z = 1$), and a pressure of 40 bar. Results will be presented for χ of 5 s^{-1} , 50 s^{-1} , 150 s^{-1} , 500 s^{-1} , 1000 s^{-1} , and 2000 s^{-1} . Recall that the χ_{ign} for the 160-species n-heptane mechanism is about 188 s^{-1} and the χ_{ext} is about 4375 s^{-1} . Hence, the procedure employed for cases where χ is greater than χ_{ign} is to compute a case with χ_{st} is 5 s^{-1} until the temperature and primary species concentrations reach steady-state. The results from this computation will then be employed as the initial condition for the higher χ_{st} cases and computed for a further 1.5 ms.

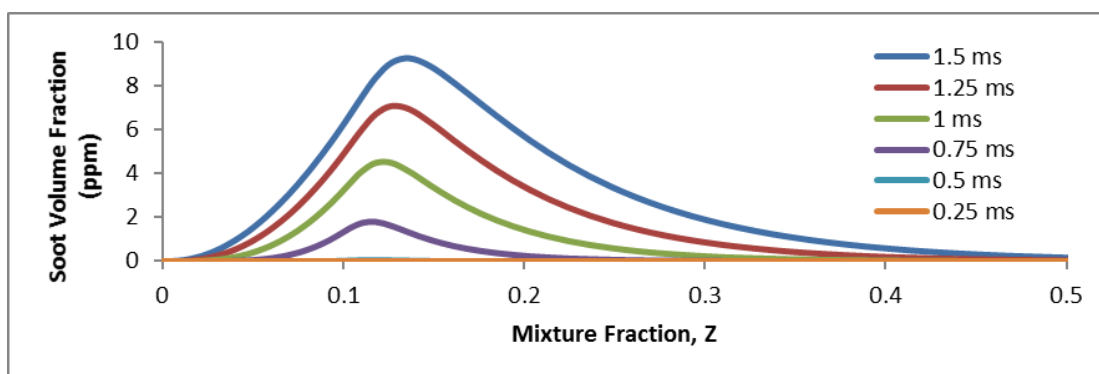


Figure 5.2: Soot volume fraction rising continuously over time for the petrodiesel surrogate mechanism at a χ of 5 s^{-1} .

Figure 5.2 shows the time-evolving soot volume fraction (f_v) when the χ_{st} has a value of 5 s^{-1} . The f_v increases with time and its peak value shifts towards richer mixture fraction values reflecting the shift in the precursor species benzene (A1) to pyrene (A4). Figure 5.3(a) shows the soot volume fraction at 1.5 ms for all χ_{st} calculated, from 5 s^{-1} to 2000 s^{-1} for this mechanism. It can be clearly seen that the f_v decreases with increasing χ_{st} . As the χ_{st} increases, the greater mixing (diffusion in the Z-space) results in reduced formation rates and increased oxidation rates.

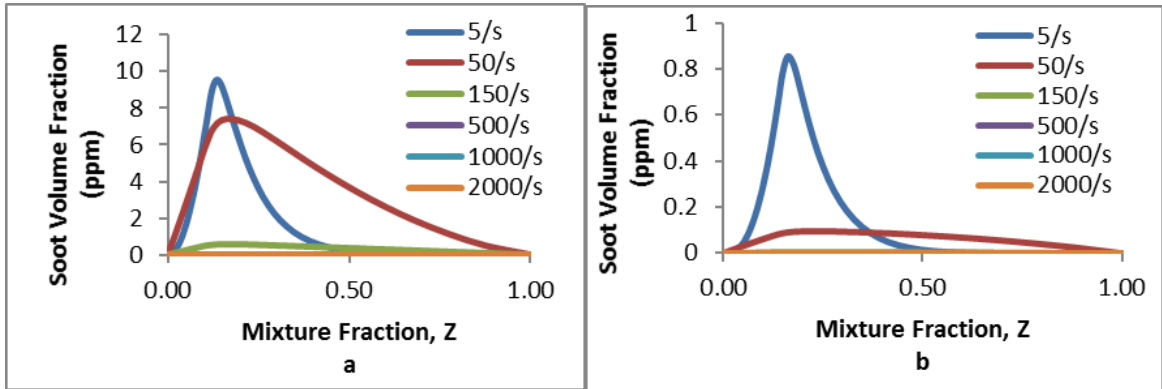


Figure 5.3: Soot volume fraction at various χ for a) HEP253, and b) TBS214.

In fact, soot f_v values are negligible for values above the χ_{ign} . It is interesting to note that flame lift-off in petrodiesel jets has been shown to occur at the axial location where the χ_{st} is equal to the χ_{ign} (Bajaj et al., 2012). This suggests that soot f_v will be practically non-existent at the lift-off length (LoL) and progressively increase downstream in the jet as χ_{st} decreases. The combination of increasing residence time and decreased χ_{st} is responsible for increasing axial concentrations of soot. The peak soot concentration occurs toward the head of the jet (Liu et al., 2010). Figure 5.3(b) shows the corresponding results for TBS214. As χ_{st} is increased, the soot f_v drops. The peak soot f_v at 5 s^{-1} , is about 10 times lower than that of HEP253. Whereas soot f_v are negligible for χ values greater than that of 150 s^{-1} in the case of HEP253, they are negligible for values greater than about 50 s^{-1} in the case of TBS214. It is interesting to note that this value is close to the χ_{ign} . It is not known if the correlation with the χ_{ign} has a fundamental origin. This has to be explored in further work. The most important point is that soot formation in TBS214 is more sensitive to increase in χ than in HEP253. In other words, increasing turbulence has a greater impact on soot formation in biodiesel engines compared to petrodiesel engines. From a practical point of view, lower levels of turbulence are needed to reduce soot in biodiesel engines compared to petrodiesel engines. If this conclusion holds, it is significant.

Table 5.2 lists the peak soot f_v , Z at the peak soot f_v , and the corresponding temperature for HEP253 and TBS214 at χ_{st} . The table also includes TBS304, which will be discussed in Section 6.2. This table emphasises the conclusions drawn in the discussion above. It is interesting to note that the Z at peak soot f_v with both TBS is, in general, consistently richer than with HEP253. This is consistent with the fact that the Z_{st} of TBS is about 0.08 whereas it is about 0.063 for HEP253. The rate of change in peak soot f_v in biodiesel as the strain rate increases is much larger compared to petrodiesel.

Table 5.2: Soot formation characteristics for HEP253, TBS214 and TBS304.

Fuel	χ (s^{-1})	Peak Soot f_v (ppm)	Mixture Fraction, Z	Temperature (K)
HEP253	5	9.6	0.137	2167
	50	7.4	0.176	1842
	150	6.0×10^{-1}	0.161	1851
	500	4.1×10^{-2}	0.176	1788
	1000	4.5×10^{-3}	0.214	1623
TBS214	5	1.26	0.176	1969
	50	7.67×10^{-2}	0.194	1875
	150	1.27×10^{-3}	0.214	1804
	500	1.42×10^{-6}	0.263	1623
	1000	1.12×10^{-8}	0.328	1440
TBS304	5	2.62	0.177	1972
	50	3.41×10^{-1}	0.177	1980
	150	7.39×10^{-2}	0.192	1912
	500	1.41×10^{-3}	0.229	1762
	1000	4.14×10^{-5}	0.307	1497

Figure 5.4 shows the NO concentration for (a) HEP253 and (b) TBS214 at the various χ . Similar to the soot f_v values, the peak NO concentration decreases as χ_{st} increases. However, the drop in peak concentration is not as large as compared to soot. This reflects the fact that NO formation is primarily temperature dependent. The prompt NO mechanism takes over the thermal NO mechanism as peak temperature decreases with increasing χ_{st} . (See Section 2.4.1 for details.) The differences shown reflect differences in temperature. The behaviour of TBS214 is very similar to that of HEP253 and the quantitative values are similar to those of HEP253.

Table 5.3 lists the peak NO concentration, the Z at the peak NO concentration, and the corresponding temperature for HEP253, TBS214 and TBS304 at the various values of χ . Although the changes in NO peak concentration are not as dramatic for soot, there are some interesting observations that can be made. As the χ is increased, the peak NO concentration decreases more rapidly for both TBS mechanisms.

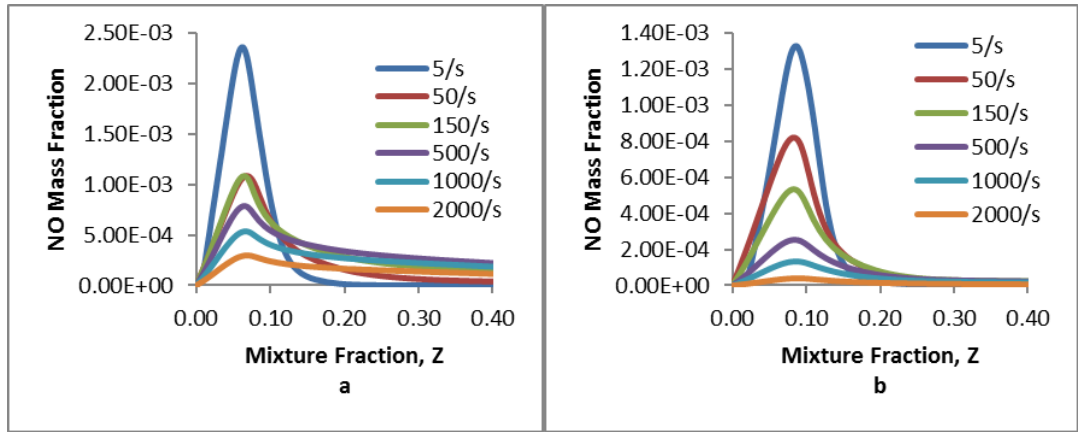


Figure 5.4: NO species concentration at various strain rates for a) HEP253 and b) TBS214.

For HEP253 case, the NO peak drops by about a factor of 8 from 5 s^{-1} to 2000 s^{-1} , compared to a factor of over 30 for both TBS214 and TBS304. In other words, the rate of change in peak NO concentration in biodiesel as the strain rate increases is much larger reflecting a greater reduction in peak temperature. Recall that the extinction strain rate for TBS fuel-only mechanism is lower than for the 160-species n-heptane mechanism (Table 5.1).

Table 5.3: NO formation characteristics for HEP253, TBS214 and TBS304.

Fuel	SDR (/s)	Peak NO Mass Fraction	Mixture Fraction	Temperature (K)
HEP253	5	2.30×10^{-3}	0.0633	2614
	50	2.30×10^{-3}	0.0676	2614
	150	1.09×10^{-3}	0.0654	2597
	500	7.84×10^{-4}	0.0654	2495
	1000	5.40×10^{-4}	0.0676	2410
TBS214	5	1.48×10^{-3}	0.0844	2604
	50	8.36×10^{-4}	0.0844	2641
	150	5.35×10^{-4}	0.0844	2579
	500	2.57×10^{-4}	0.0844	2450
	1000	1.33×10^{-4}	0.0844	2330
TBS304	5	1.52×10^{-3}	0.0839	2602
	50	6.22×10^{-4}	0.0863	2607
	150	5.07×10^{-4}	0.0839	2579
	500	2.42×10^{-4}	0.0863	2460
	1000	1.28×10^{-4}	0.0889	2353

5.4 Summary and Conclusions

In this chapter, the limit phenomena of various petrodiesel and biodiesel fuel surrogate mechanisms were studied. In general, it was found that both the ignition and extinction strain

rates of petrodiesel are higher than those of biodiesel. The effect of changes in strain rate on pollutant formation was then studied. As the strain rate increased, the reduction of soot in biodiesel was greater than in petrodiesel. This implies that to achieve the same soot formation rate, a biodiesel engine can be less turbulent than a petrodiesel engine. Another way of thinking about this is that changes in mixing rate induced by turbulence have a much greater impact in biodiesel-fuelled engines compared to petrodiesel-fuelled engines. It is noted that the peak soot volume fraction is also influenced by the choice of the surrogate fuel kinetic mechanism. The influence of the role of specific species on the formation of soot will be investigated in the next chapter. For NO, it was found that increasing strain affects changes in NO for both fuels similarly, which is not surprising because NO formation is primarily temperature-dependent and the strain rate affects it primarily through changes in temperature. In the case of soot formation, the strain appears to affect the soot kinetics directly and not just through changes in temperature.

6 Soot Formation Reaction Pathway Analysis

6.1 Introduction

In this chapter, reaction pathway analyses of oxidation and soot formation kinetics are carried out to identify the critical pathways for soot formation in biodiesel and petrodiesel combustion. In Section 6.2, a 304-species biodiesel surrogate mechanism is discussed. Its purpose is to ensure that no chemical species are left out in this pathway analysis. In Section 6.3, the reaction pathway analysis will be conducted. This discussion will end with a summary in Section 6.4.

6.2 304-Species TBS Mechanism

In Section 5.3, it was found that the peak soot volume fraction (f_v) predicted by a combined biodiesel, soot and NO kinetic mechanism, TBS214 (“TBS” stands for ternary biodiesel surrogate), is about an order of magnitude lower than predicted by the petrodiesel alternative (HEP253) at a scalar dissipation rate (χ) of 5 s^{-1} . Though this is encouraging, the possibility cannot be ruled out that this difference may arise from deficiencies in the primary fuel mechanism. Both of the mechanisms employed are skeletal mechanisms derived from larger detailed mechanisms. Mechanism reduction is achieved to meet certain constraints. Accurate prediction of soot was not, however, a constraint for either mechanism when developing either mechanism. As a result, reactions that may be important for soot formation may be missing in one mechanism or another, or both. The development of a new mechanism is beyond the scope of the current research. However, it is possible to assess the sensitivity of the soot predictions to the underlying fuel-oxidation mechanism in indirect ways.

In this study, the sensitivity of the soot predictions to the TBS surrogate mechanism was accessed. This was done by taking the original 115-species TBS mechanism (Luo et al., 2012), and adding to this, reactions from the 160-species n-heptane petrodiesel surrogate mechanism (Seiser et al., 2000) which are also present in the 3299-species detailed TBS mechanism (Herbinet et al., 2008). Figure 6.1 illustrates this concept.

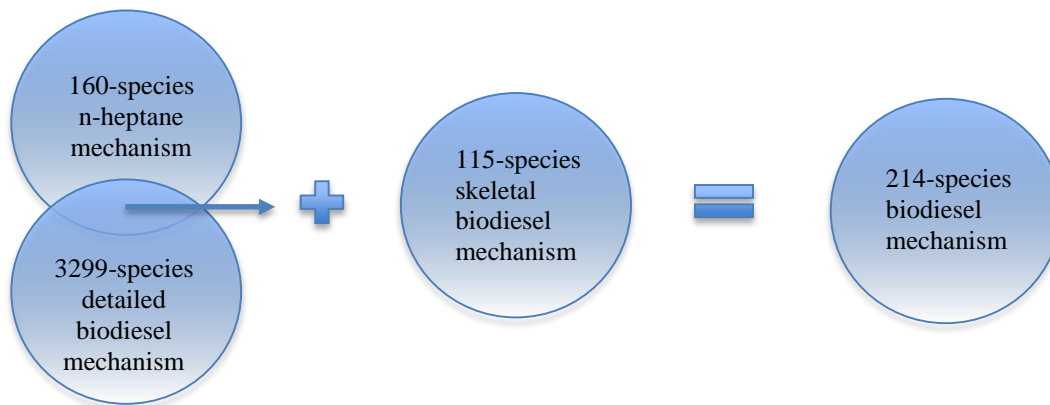


Figure 6.1: Creation of a 214-species biodiesel mechanism.

The ABF soot (Appel et al., 2000) and GRI-Mech 3.0 NO (Smith et al., 1999) mechanism is then added to this. The result is a 304-species 1609-reaction TBS mechanism, henceforth referred to as TBS304. The additional species in the primary fuel section in this mechanism are listed in Appendix B. This ensures that the differences in soot between biodiesel and petrodiesel are not on account to species being removed due to the reduction process of the detail biodiesel mechanism. This 304-species TBS mechanism will be evaluated below by comparing soot predictions with the TBS214 mechanism. Figure 6.2 shows the soot f_v evolution when employing the TBS214 and TBS304 mechanisms as a function of mixture fraction at different times. The overall behaviour of soot peak f_v is, however, very similar to TBS214. Due to the influence of the additional reactions, the soot f_v increases faster and is noticeably higher in TBS304 than TBS214.

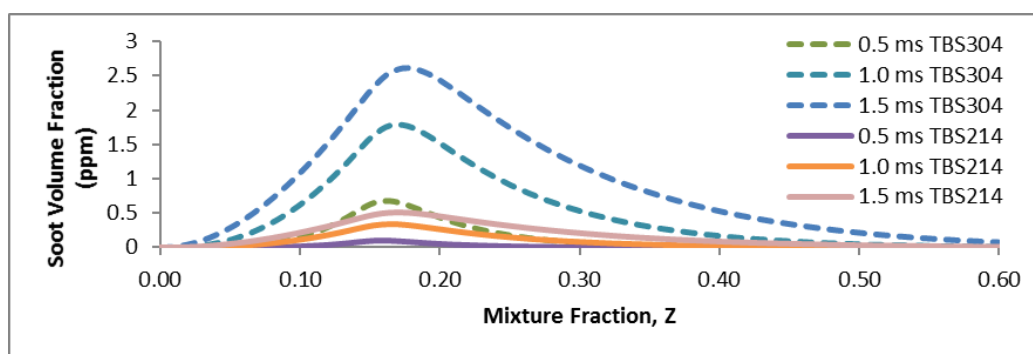


Figure 6.2: Time evolution of soot volume fraction for TBS 214 and TBS304.

To summarise the results above, Figures 6.3(a) and (b) show the soot f_v and NO concentration of HEP253, TBS214 and TBS304. While there are no differences in the NO results with the two TBS mechanisms, the peak soot f_v is about a factor of two higher with TBS304 compared to the TBS214. Comparisons with experimental data are needed before concluding that one mechanism is superior to another. It is then of important to understand why

n-heptane and TBS oxidation lead to drastic differences in soot f_v . What are the differences in chemical pathways which lead to the differences?

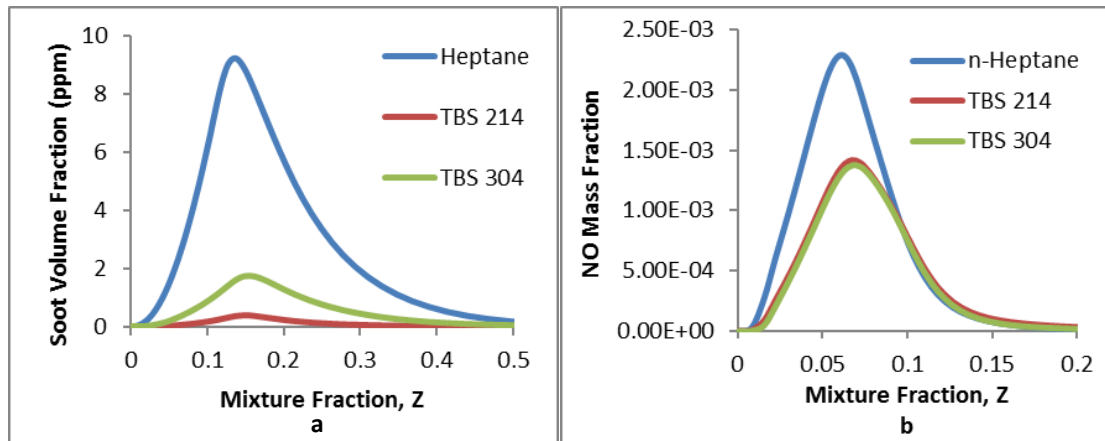


Figure 6.3: a) Soot volume fraction and b) NO concentration for the three fuel surrogates.

6.3 Reaction Pathway Analysis

In this section, the coupled primary fuel, ABF soot and GRI-Mech 3.0 NO mechanisms will be examined further to understand the key reaction pathway that leads to the formation of soot. In particular, this analysis will lead to an improved understanding of the differences in the predictions of soot for n-heptane and TBS. The ABF mechanism (Appel et al., 2000) has the addition of C_2H_2 to the aromatic ring after the abstraction of the H atom as an important step in the soot formation pathway (See Section 2.4.2 for details regarding the HACA mechanism). Differences in C_2H_2 concentrations may be responsible for the differences in soot formation rates. Figure 6.4 shows the C_2H_2 concentration for the two fuels at a time of 1.5 ms when the χ_{st} is 5 s^{-1} . Notice that while there are differences in C_2H_2 f_v , these differences do not explain the order of magnitude difference in soot f_v . Thus, the difference in soot f_v for the petrodiesel and biodiesel surrogates has to arise from the concentration of the aromatic species, i.e. the PAH (see Section 2.4.2). Figure 6.5 shows the concentration of aromatic species benzene (also referred to as $A1$ as it is one aromatic ring) for the same conditions as Fig. 6.4. Peak concentrations of soot in TBS214 and TBS304 are different by a factor of about 2.5 at this time. Recall that the peak soot f_v between HEP253 and TBS214 are different by a factor of 7 at the same time (Fig. 6.3(a)).

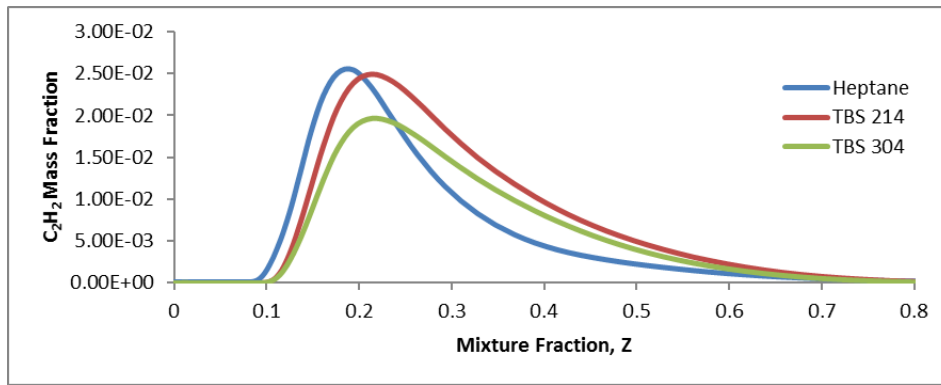


Figure 6.4: C₂H₂ concentration for the three fuel surrogate mechanisms.

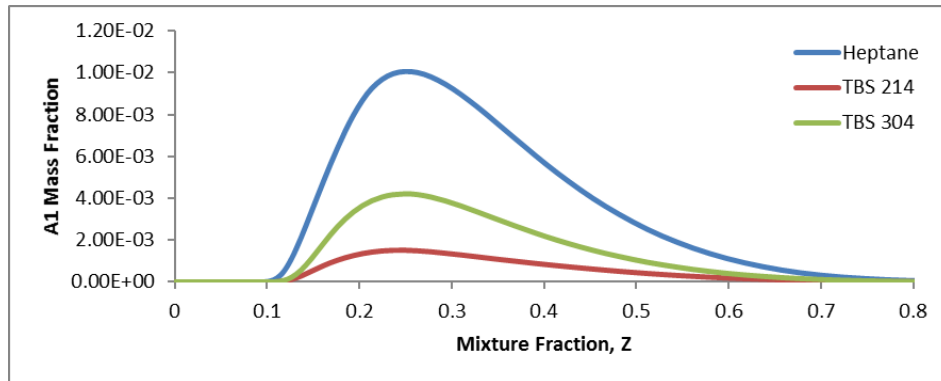


Figure 6.5: A1 concentration for the three fuel surrogate mechanisms.

The next step is to determine why there is a difference in the concentration of the aromatic species. Note that the aromatic species is formed through the primary fuel mechanism. A reaction pathway analysis was carried out in the one-dimensional flamelet code (See Section 3.2). For reference, the ignition delay time is found to be 0.42 ms for the n-heptane mechanism and 0.52 ms for the TBS mechanism. This is defined as the time where the peak temperature reaches 1,500 K. It is interesting to note that biodiesel ignition delay time is generally lower than that of petrodiesel. So, the results presented here are specific to the surrogate fuels selected and not a reflection of actual engine behaviour. Typical results from the computations are shown in Figure 6.6 for n heptane and TBS at 1.5 ms after ignition.

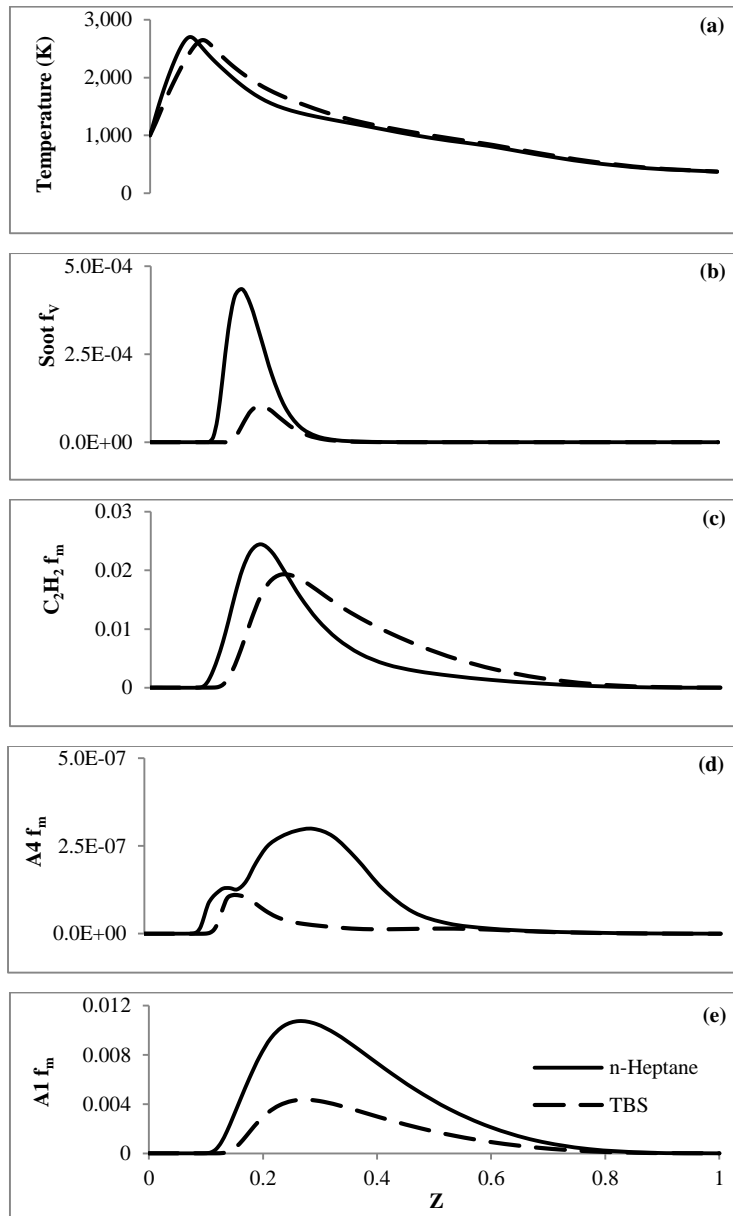


Figure 6.6: Plots for temperature, soot volume fraction, and acetylene, A4 and A1 mass fraction.

Temperature, soot f_v , and mass fractions (f_m) of, acetylene, A4, and A1 are shown with respect to Z . From the temperature plot (a), it can be seen that the peak temperature is similar between n heptane and TBS although the Z where the peak occurs is different because Z_{st} is higher for biodiesel. These results are consistent with previous findings (Hoffman and Abraham, 2009). However, the soot f_v is lower in TBS by about a factor of four (Fig. 6.6(b)). The impetus becomes to understand these differences from a kinetics perspective in the context of engine conditions. Recall that the soot mechanism used in this study is identical between the n-heptane and TBS mechanism, and that the HACA mechanism begins with the benzene (A1) species, subsequently forming A2, A3 and A4 through hydrogen-abstraction and carbon-addition. In this regard, it is useful to compare the concentration of C_2H_2 , A1, and A4 between n-heptane and TBS to identify differences. The difference in C_2H_2 concentration

(Fig. 6.6(c)) of about 20% is not enough to explain the differences in soot. Comparing Fig. 6.6(d), it can be seen that the difference in $A4$ is in fact of the same magnitude as the difference in soot volume fraction. Fig. 6.6(e) shows that, while differences in $A1$ are not as large as in the soot f_v or $A4 f_m$, they are about a factor of three. The next section will discuss the origin of this difference.

To understand the difference in $A1$ (and eventually, soot) between n-heptane and TBS, an understanding of the reaction pathway leading to the formation of $A1$ is needed. By tracing the formation of $A1$ through the various reactions that form it, critical species and reactions may be identified that cause this eventual difference. As the maximum f_m of $A1$ occurs at $Z = 0.263$ in n heptane and $Z = 0.277$ for TBS, the pathway will be investigated at that Z for each surrogate fuel. Note that in terms of equivalence ratio, these Z correspond to 5.31 and 4.41, respectively, i.e. the peak $A1$ occurs at an overall leaner equivalence ratio in TBS than in n-heptane.

Table 6.1 shows the overall reaction pathway for the formation of $A1$ through its various precursors. The first column shows the reaction number. The next four columns list the chemical reaction and the Arrhenius reaction rate constants: the pre-exponential factor (A), the temperature-exponent (b), and the activation energy (E_A). For each reaction, a critical species is in **bold** and underlined. This species is identified as such because among the species at that level, it is most likely to influence the formation of $A1$. The species is investigated for its influence on the formation of soot. The last 3 columns list the f_m of the critical species in n-heptane, TBS, and their ratio, respectively.

At the top level, reaction (henceforth, written as ‘Rxn’) 1.1 – 1.3 form $A1$. Comparing the ratios of the critical species, the ratios of n-C₄H₅ and n-C₆H₇ f_m are the largest which may explain the difference in $A1$ between n-heptane and TBS. However, the f_m of n-C₆H₇ is relatively low to cause such an impact in $A1$. Hence, Rxn 1.2 is the most likely route to $A1$. This type of evaluation is repeated to determine the key reactions and species that form n-C₄H₅. n-C₄H₅ is formed by numerous reactions, but only four important ones will be listed in Table 6.1. Comparing the ratios of species, it can be seen that the ratio of C₂H₃ f_m is largest between n-heptane and TBS. It is interesting to examine Rxn 2.3; the f_m of C₅H₅O is 125 times higher in TBS compared to n-heptane presumably because TBS is oxygenated.

Table 6.1: Reaction pathway analysis for the formation of A1

Reaction #	Reaction	A	b	E _A	Heptane	TBS	Heptane:TBS Ratio
1.1	$\underline{\text{C}_3\text{H}_3} + \text{C}_3\text{H}_3 = \text{A1}$	2.0E+12	0	0	1.07E-04	9.51E-05	1.13
1.2	$\underline{\text{n-C}_4\text{H}_5} + \text{C}_2\text{H}_2 = \text{A1} + \text{H}$	1.6E+18	-1.9	7400	3.64E-06	1.54E-07	23.6
1.3	$\underline{\text{n-C}_6\text{H}_7} = \text{A1} + \text{H}$	5.3E+25	-4.4	17300	4.19E-09	9.61E-11	43.6
2.1	$\underline{\text{C}_2\text{H}_3} + \text{C}_2\text{H}_2 = \text{n-C}_4\text{H}_5$	8.1E+37	-8.1	13400	5.19E-05	6.37E-06	8.15
2.2	$\underline{\text{C}_4\text{H}_6} + \text{OH} = \text{n-C}_4\text{H}_5 + \text{H}_2\text{O}$	6.2E+06	2	3430	1.72E-03	1.84E-03	0.935
2.3	$\underline{\text{C}_5\text{H}_5\text{O}} = \text{n-C}_4\text{H}_5 + \text{CO}$	2.5E+11	0	43900	1.43E-09	1.79E-07	7.99E-03
2.4	$\underline{\text{C}_5\text{H}_4\text{OH}} + \text{O} = \text{CO}_2 + \text{n-C}_4\text{H}_5$	3.0E+13	0	0	5.99E-08	2.63E-08	2.28
3.1	$\underline{\text{C}_2\text{H}_4} (+\text{M}) = \text{C}_2\text{H}_3 + \text{H} (+\text{M})$	1.69E+15	0.1	107099	5.16E-02	3.64E-02	1.42
3.2	$\text{C}_2\text{H}_2 + \underline{\text{HO}_2} = \text{C}_2\text{H}_3 + \text{O}_2$	2.73E-16	-0.9	11400	9.30E-13	5.33E-08	1.74E-05
3.3	$\text{C}_2\text{H}_4 + \underline{\text{IC}_3\text{H}_7} = \text{C}_2\text{H}_3 + \text{C}_3\text{H}_8$	1.31E+11	0	17800	1.29E-04	3.44E-07	375
4.1	$\text{H} + \underline{\text{C}_3\text{H}_6} = \text{IC}_3\text{H}_7$	1.30E+13	0	1560	1.01E-02	3.99E-03	2.53
4.2	$\underline{\text{C}_3\text{H}_8} + \text{O}_2 = \text{IC}_3\text{H}_7 + \text{HO}_2$	4.00E+13	0	47500	5.98E-03	5.53E-05	108
4.3	$\text{H} + \underline{\text{C}_3\text{H}_8} = \text{H}_2 + \text{IC}_3\text{H}_7$	1.30E+06	2.4	4471	-	-	-
4.4	$\underline{\text{CH}_3} + \text{C}_3\text{H}_8 = \text{CH}_4 + \text{IC}_3\text{H}_7$	3.98E+11	0	9500	1.33E-04	3.24E-05	4.10

Knowing the critical reaction and species in the 2nd level, the pathway can be traced back further to the 3rd. Only three of the numerous reactions are listed. Rxn 3.2 has a pre-exponential factor that is too low for the forward-direction reaction to affect A1 production. However, Rxn 3.2 is interesting due to the involvement of O₂ and HO₂. Although the forward reaction is very slow, it indicates that the reverse reaction is preferred. As HO₂ is almost 60,000 times more abundant in TBS than n-heptane at the peak A1 mixture fraction, this suggests that Rxn 3.2 is a very fast oxidising reaction that drastically slows down the formation of A1 in TBS by consuming C₂H₃. Comparing Rxn 3.1 and Rxn 3.3, although the former has a greater chance of forming C₂H₃, the critical species, IC₃H₇, is more abundant in n-heptane than TBS. Thus, reaction Rxn 3.3 is the most likely reaction that contributes to the difference in A1 at this level.

The final level looks into the formation of IC₃H₇. Though there are many reactions that form IC₃H₇, only four reactions will be compared here. Looking at the hydrocarbon species, C₃H₈ has a much larger mass fraction in n-heptane than TBS and Rxn 4.2 can be concluded to form part of the critical pathway. Figure 6.7 summarizes the pathway identified above. For each species in the sequence, the f_m is significantly lower in TBS than n-heptane. It has been found that the pool of smaller hydrocarbons, such as C₂H₅, C₂H₆, and C₃H₈, has a smaller f_m in TBS than n-heptane by about 50%. The oxidation process of the biofuel does not easily disassociate the attached oxygen atoms due to the strong bonding force. The oxidation process of TBS initially breaks the fuel into more alkoxy groups, such as aldehyde and alcohol compared to n-heptane. A comparison of aldehydes and alcohols shows that their f_m in TBS is 60% higher than in n-heptane. The higher amount of oxygenated species reduces the proportion of hydrocarbons that are available to form soot precursors. While the focus in Table 4 is on C₃H₈, it has been replaced by C_mH_n in Fig. 6.7 to represent the collective pool of small hydrocarbons. This

suggests that differences in the breakdown mechanism of TBS to these lower order hydrocarbons compared to that of n-heptane plays an important role in determining the final outcome.

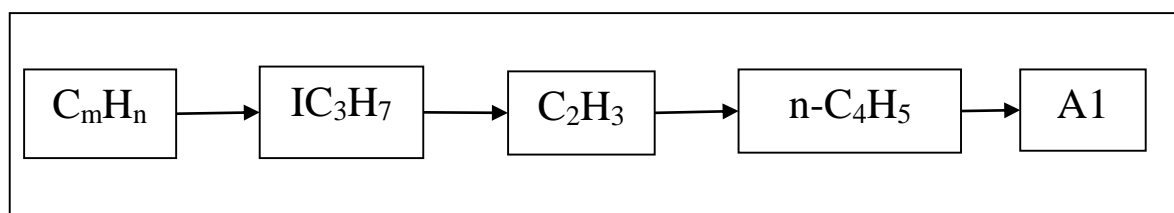


Figure 6.7: Reaction pathway of critical species that affects the formation of A1.

Another possible factor for the lower f_m of A1 in TBS is that it peaks at a leaner equivalence ratio: 4.41 as compared to 5.31 in n-heptane. Under leaner conditions, the amount of oxygen would naturally be higher, which in turn increases the oxidation of precursors of A1 and A1 itself. In fact, at the Z of peak A1, the O_2 concentration, while small, is still about six orders of magnitude larger in TBS than n-heptane. Its strong presence in TBS contributes significantly to the overall oxidation process through the creation of radicals such as O and OH. Referring back to Rxn 3.2 in Table 6.1, the high level of O_2 suggests that C_2H_3 can be more readily oxidised in the reverse reaction, thus also reducing the formation of soot.

Exhaust gas recirculation (EGR), the process of injecting a fraction of the exhaust gas back into the injection stream, has mostly been used to reduce NO_x at the expense of engine efficiency and an increase in particulates (Heywood, 1988). As it has been shown that the amount of O_2 strongly influences the formation of soot, an investigation into various EGR conditions has been carried out. It has been found that varying the initial $O_2:N_2$ ratio to reflect 20 %, 40 % and 60 % EGR does not affect the conclusions arrived in this study.

6.4 Summary and Conclusions

In this study, the cause for the difference in soot was investigated. By creating an extended biodiesel mechanism, it was found that the difference in soot between the petrodiesel and biodiesel surrogate fuel was due to the aromatic species, benzene. It was found that benzene differed in similar proportion as the soot f_v . The difference in acetylene was not enough to cause a major difference in soot. Further investigation into causes of the difference in benzene through a reaction pathway analysis arrived at a critical reaction pathway. In this pathway of most possible reactions, the differences in the species compounded as the reactions carried forward, resulting in the difference in benzene.

7 Two-Equation Soot Model Formulation

7.1 Introduction

The process of formulating a semi-empirical two-equation soot model is explored in this chapter. The soot model builds upon the understanding of the critical reaction pathway from the previous chapter. In Section 7.2, some background into soot models are touched upon. Section 7.3 outlines the computational method for this study. In section 7.4, the proposed two-equation soot model is presented. A sensitivity analysis of the soot model is performed in Section 7.5, along with the optimisation process. Finally, Section 7.6 ends this chapter with a summary and conclusions.

7.2 General Formulation of Two-Equation Soot Models

In conventional compression-ignition engines, fuel is injected directly into the cylinder toward the end of the compression stroke and it auto-ignites. Combustion primarily occurs in highly strained and wrinkled diffusion flames surrounding the fuel jet and located where the fuel/air mixture is stoichiometric. Polycyclic aromatic hydrocarbons (PAHs) are formed in the rich mixture downstream of the flame lift-off height and eventually form soot farther downstream (Dec, 1997; Westbrook, 2000). Predictive models for soot can aid engine designers in their efforts to develop cleaner engines. However, the modelling of soot is challenging because the kinetic mechanisms of soot formation, the turbulence/chemistry interactions as it affects soot formation, and the physics of soot particle growth and coagulation are complex and not well known. (Please see Section 2.4.2 for more details.) Furthermore, reliable quantitative soot measurements in fuel sprays have been scarce, especially under engine conditions, and are only now becoming available (www.sandia.gov/ecn/).

The PAH mechanism builds upon the primary fuel mechanism; but, a complete mechanism for oxidation of practical fuels is not feasible due to the large number of components in a fuel sample (Pitz and Mueller, 2011). Thus, surrogate fuels such as octane, dodecane, heptane, or a combination are proposed to represent practical fuels. For practical research purposes, detailed oxidation mechanisms for these fuels which often include hundreds of species and thousands of reactions are simplified to skeletal or reduced mechanisms. This simplification may reduce the accuracy of predictions of the HACA mechanism by omitting species or reactions critical to the soot formation process. Available skeletal and reduced mechanisms have not been developed with the requirement that such mechanisms predict soot kinetics accurately. For that

matter, it is not clear that available detailed mechanisms include the details needed for the prediction of soot.

In any case, solving detailed kinetics-based soot models is computationally expensive, and not feasible for large-scale engine parametric or optimisation studies, irrespective of whether they are built on detailed or skeletal/reduced fuel oxidation mechanisms. A less computationally intensive approach is to use semi-empirical methods to predict soot formation by employing two additional transport equations to model the soot mass (or volume fraction) and soot particle number. These transport equations typically include models for inception, soot growth, coagulation, and oxidation. However, many of such soot models employ acetylene as both the soot inception species and that for surface growth. In Section 6.3, it was understood that in terms of petrodiesel and biodiesel combustion, the peak acetylene mass fraction was only 20 % apart. This cannot differentiate soot between these fuels. This work is motivated by the desire to develop a semi-empirical two-equation model that can predict soot in both *diesel* and *biodiesel* non-premixed combustion in engine applications. Thus, the desire to formulate a novel two-equation soot model that can achieve this.

7.3 Computational Method

As diesel fuel consists of over 100 hydrocarbons, its direct chemical kinetic modelling is computationally intensive even if kinetic mechanisms were available (Pitz and Mueller, 2011). For this study, n-heptane (C_7H_{16}) is used as the surrogate fuel for diesel as it has been shown to represent important aspects of the chemical kinetics reasonably well (Chen et al., 2012). A 160-species n-heptane surrogate mechanism is chosen (Seiser et al., 2000) as it provides the best compromise between computational time and accuracy. In that study, the mechanism was developed by matching the ignition delay to shock tube results at 3.2, 13.5, and 38 bar. This makes the mechanism well suited for engine studies. Hoffman and Abraham (2009) found that the 160-species mechanism has sufficient detail for coupling with the soot kinetics mechanism of Appel et al. (2000). A 44-species skeletal n-heptane surrogate mechanism is also employed when evaluating the two-equation semi-empirical model (Liu et al., 2004). Similar to the 160-species mechanism, this mechanism has been validated by matching the ignition delay results to experimental data at pressures similar to those of conventional diesel engines. In addition, the mole fraction of various critical species were also matched with experimental data.

Though the composition of biodiesel is simpler than of hydrocarbon diesel (Herbinet and Pitz, 2008), the detailed oxidation kinetics of biodiesel is not well established. For the current study, a ternary biodiesel surrogate fuel (TBS) proposed in the literature is

employed (Herbinet and Pitz, 2008). The TBS consists of three fuel components: 25% methyl decanoate (MD), 25% methyl-9-decanoate (MD9D) and the remainder n-heptane. A 115-species skeletal kinetics mechanism for the biodiesel surrogate is employed (Luo et al., 2012). This mechanism was obtained by reducing the detailed TBS mechanism (Herbinet and Pitz, 2008) through validation of ignition delay, temperature, and the mole fraction of critical species at elevated pressures. A larger mechanism obtained by combining the original 115-species skeletal TBS mechanism with additional reactions from the 160-species n-heptane mechanism that also appear a detailed mechanism developed for methyl decanoate (Herbinet and Pitz, 2008) will also be employed. (Please see Fig. 6.1.) This reduces the probability that the difference in soot formation is due to differences in the complexity of the kinetics.

In the approach we have adopted, we employ the detailed soot kinetics mechanism of Appel et al. (2000), henceforth referred to as the ABF mechanism, as the reference mechanism to generate soot results to compare with the proposed semi-empirical model. The ABF mechanism consists of 101 species and 546 reactions. In the mechanism, soot is formed through several steps subsequent to the formation of pyrene (the inception species) through the HACA mechanism. Although the specific steps in the inception stage are not well known, the pathway via PAHs is the most widely accepted Frenklach and Warnatz, 1987). The PAH formation pathway forms soot through the Hydrogen-abstraction carbon-addition (HACA) process (Kazakov and Frenklach, 1998; Frenklach et al., 1988). (Please see Section 2.4.2 for more detail.) Soot formation past the kinetic mechanism is then modelled by using the method of moments (Frenklach and Harris, 1987). While we will not present any results of the prediction of nitrogen oxides in this study, the mechanisms employed included the NO kinetics from GRI-Mech 3.0 since this is of interest in diesel and biodiesel combustion (Smith et al., 1999).

To summarise, the fuel, ABF soot, and GRI-Mech 3.0 kinetic mechanisms are combined together to form a 253-species, 2085-reactions n-heptane mechanism as the diesel surrogate, and the 304-species, 1609-reactions TBS mechanism as the biodiesel surrogate. This will be used for the detailed kinetics benchmark. For the two-equation soot model, a 44-species n-heptane fuel mechanism and a 115-species TBS (biodiesel surrogate) fuel mechanism will be used.

The semi-empirical soot model formulated in this work consists of two equations, one for the soot volume fraction or soot density and the other for the soot number density. The equations have the general form:

$$\frac{d\rho y_s}{dt} = \alpha_1 + \alpha_2 - \alpha_3 - \alpha_4 , \quad (7.1)$$

$$\frac{dN}{dt} = \beta_1 - \beta_2, \quad (7.2)$$

where ρy_s is the soot species density and N is the soot number density. Empirical models for inception, surface growth, oxidation via oxygen, and oxidation via OH serve as source terms for soot species density and are denoted as $\alpha_1 \dots \alpha_4$, respectively, in Eq. (7.1). Inception and coagulation serve as source terms for soot number density and are denoted as β_1 and β_2 , respectively, in Eq. (7.2).

In the ABF mechanism, pyrene (also known as $A4$ as it has four aromatic rings) is the largest and last species to be formed kinetically before soot is modelled. It is formed via the HACA mechanism by benzene, $A1$. Thus, the mass fraction (f_m) of $A1$ directly affects the soot volume fraction (f_v). Figure 7.1 shows the plots of (a) soot volume fraction (f_v) and f_m of (b) $A1$, (c) C_2H_2 , and (d) C_2H_3 for both the 253-species n-heptane mechanism and 304-species TBS mechanism taken at 2 ms after ignition in the flamelet simulation, where ignition is defined as occurring when the temperature reaches 1,500 K.

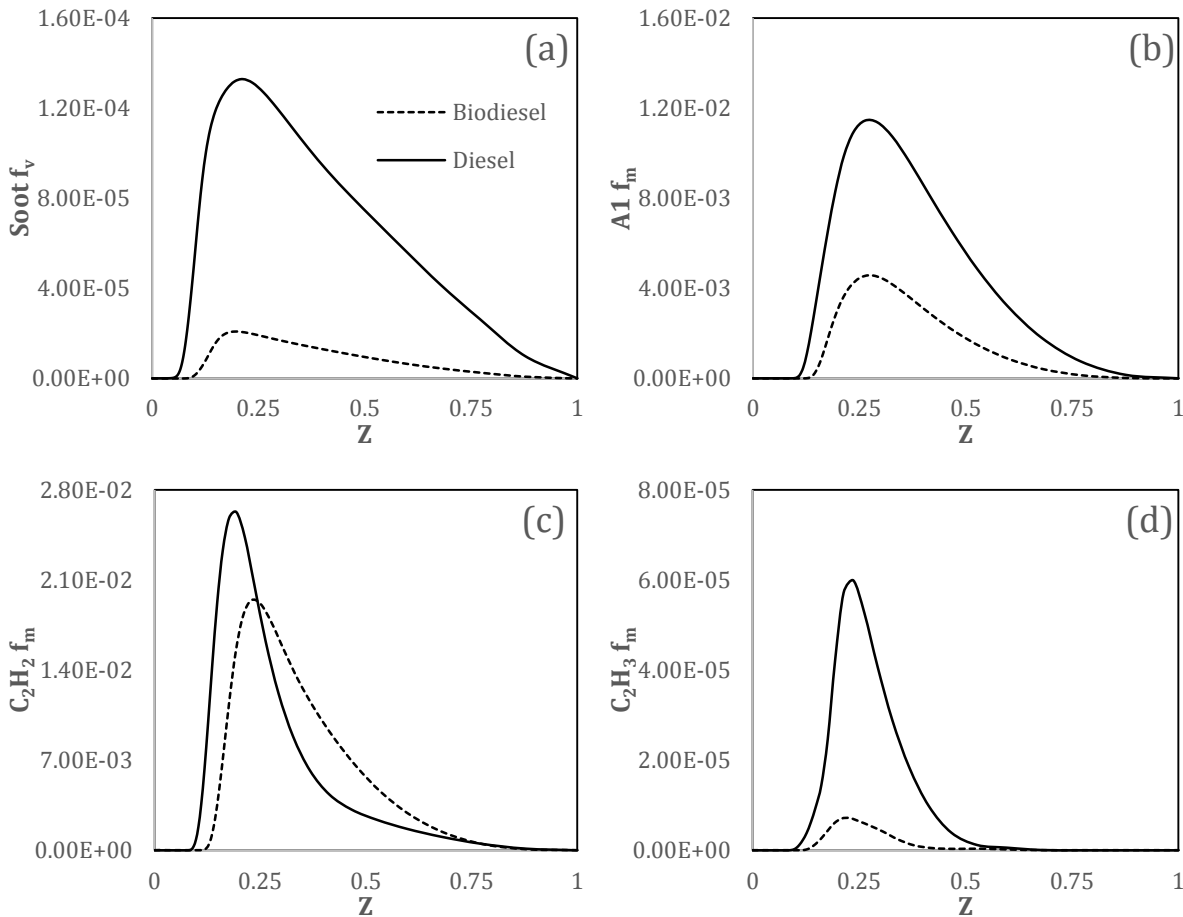


Figure 7.1: Volume fraction of soot (a), and mass fraction of (b) $A1$, (c) C_2H_2 , (d) C_2H_3 in the diffusion flame.

It can be seen in Fig. 7.1(a) that the difference in soot f_v between the n-heptane and TBS cases is about a factor of 6. It is well known that biodiesel combustion results in lower soot

volume fractions than diesel combustion and so this difference is as expected. Recall that the formation of soot through the HACA mechanism begins with the benzene ($A1$) and acetylene (C_2H_2) species, and reacts to form larger aromatic species. Comparing Fig. 7.1(b) and 1(c), though the peak C_2H_2 f_m is lower in the n-heptane case compared to TBS case, the difference is not large enough to affect the difference in soot. It is clear that the difference in soot is mainly caused by the differences in the $A1$ species, not C_2H_2 . This suggests that using C_2H_2 as an inception species for a two-equation soot model, to predict biodiesel soot production is not suitable, because it cannot explain the large differences in soot between n-heptane and TBS. Thus, many of the developed two-equation soot models in the present literature cannot be used to accurately to predict soot in both petrodiesel and biodiesel. One may choose to select the species $A4$ as an inception species, such as in the work of Sukumaran et al. (2013). However, if $A4$ or any aromatic species ($A1 - A4$) is selected as the soot inception species, a mechanism with the complexity of the ABF mechanism would be required, in addition to the fuel mechanism, to predict it and this adds to computational cost. And in that case, one would rather use the kinetic mechanism directly, instead. The question then raised is the following: is there a species common to n-heptane and biodiesel in their primary fuel mechanisms that can be used as an inception species?

From Fig. 7.1, it can be clearly seen that there is – and it is the vinyl radical (C_2H_3). Looking back to Fig. 7.1, it can be seen that the ratio of soot volume fraction is almost identically predicted by C_2H_3 . In the formulating the critical reaction pathway in Section 6.3 (Fig. 6.7), C_2H_3 also lies within this pathway. In addition, if the fuel mechanism for both the 160-species n-heptane and 115-species TBS mechanism are studied, C_2H_3 is a species within both of them. As acetylene is already part of the fuel mechanism, the computations can completely omit the ABF soot mechanism, thus drastically saving on computational time. In the literature, the important role of the vinyl radical in the formation of soot is well supported (Richter and Howard, 2000; Wang and Rutland, 2004; Senosiain and Miller, 2007). Other work has even proposed the vinyl radical replacing acetylene as the critical species in PAH growth (Shukla and Koshi, 2012), instead of acetylene.

7.4 The Proposed Two Equation Soot Model

The structure of the two-equation semi-empirical model was discussed in Section 7.3 and Section 2.4. The various terms in the soot volume fraction and number density equations were also discussed. In this section, models will be proposed for the various terms in a novel semi-empirical two-equation soot model. Recall that our objective is to predict soot in both

hydrocarbon diesel and biodiesel engine combustion with the same model. The terms in the model are based on the understanding gained from the use of the ABF model in Section 6.3. The accuracy of the proposed models is, of course, dependent on the accuracy of the ABF model. Nevertheless, it is our opinion that the approach outlined here is one that can be adopted by other researchers in development of semi-empirical soot models.

7.4.1 Soot Inception

In our discussion below, we use a notation format of α_1 and β_1 as in Eqs. (7.1) and (7.2) to indicate the various terms. Our analysis in Section 7.3 shows that the vinyl radical (C_2H_3) can be used as a suitable soot inception species. The corresponding inception source terms are shown in Eq. (7.3) and (7.4) below:

$$\alpha_1 = L_{\alpha 1} \times \exp\left(-\frac{E_{\alpha 1}}{T}\right) \times \rho \times Y_{C_2H_3}, \quad (7.3)$$

$$\beta_1 = \frac{\alpha_1}{W_{C_2H_3} \times C_n}, \quad (7.4)$$

where T is the temperature of the gas phase, ρ is the density of the gas phase, $Y_{C_2H_3}$ is the mass fraction of the vinyl radical species, $W_{C_2H_3}$ is the molecular mass of the vinyl radical species, and C_n , taken to be 100, is the number of carbon atoms in the inception soot particle. The understanding here is that there is an exponential dependence of the inception rate on temperature and a linear dependence on the density. $L_{\alpha 1}$ and $E_{\alpha 1}$ are model constants for the linear and exponential dependence, respectively.

7.4.2 Surface Growth

For the HACA mechanism of soot formation, surface growth is the chemical bonding of acetylene (C_2H_2) to the soot species. The α_2 source term is then formulated as:

$$\alpha_2 = L_{\alpha 2} \times \exp\left(-\frac{E_{\alpha 2}}{T}\right) \times \sqrt{S} \times \rho \times Y_{C_2H_2}, \quad (7.5)$$

where S is the soot surface area. There is also a linear dependence on density. $L_{\alpha 2}$ and $E_{\alpha 2}$ are model constants. The soot surface area is defined in Eq. (7.6) below:

$$S = \pi \left[\frac{6\rho y_s}{\pi\rho_{c(s)}N} \right]^{2/3} N, \quad (7.6)$$

where N is the number density of soot and $\rho_{c(s)}$ is the density of the soot particle, taken to be 1.8 g cm^{-3} . $L_{\alpha 2}$ and $E_{\alpha 2}$ are model constants for the linear and exponential dependence, respectively.

7.4.3 Coagulation

Coagulation causes an agglomeration of soot particles, thus reducing the soot number density. It does not affect the soot volume fraction. It is modelled by Eqn. (7.7) below, which is taken from the model by Moss et al. (1995):

$$\beta_2 = 2.25 \times 10^{15} \times T^{1/2} \times N^2, \quad (7.7)$$

7.4.4 Oxidation by O₂

Oxidation by O₂ follows the standard Nagle and Strickland-Constable (1962) formulation. This is shown in Eqn. (7.8) below:

$$\alpha_3 = L_{\alpha 3} \times \frac{12 \times S}{M_{c(s)}} \left[\left(\frac{K_A P_{O_2}}{1 + K_Z P_{O_2}} \right) x + K_B P_{O_2} (1 - x) \right], \quad (7.8)$$

where,

$$x = \frac{P_{O_2}}{P_{O_2} + \frac{K_T}{K_B}}, \quad (7.9)$$

$$K_A = 30 \times \exp\left(\frac{-15800}{T}\right), \quad (7.10)$$

$$K_B = 8 \times 10^{-3} \times \exp\left(\frac{-7640}{T}\right), \quad (7.11)$$

$$K_T = 1.51 \times 10^5 \times \exp\left(\frac{-49800}{T}\right), \quad (7.12)$$

$$K_Z = 27 \times \exp\left(\frac{3000}{T}\right), \quad (7.13)$$

In Eq. (7.8), $M_{c(s)}$ is the molecular mass of one carbon atom, P_{O_2} is the partial pressure of oxygen and $L_{\alpha 3}$ is a model constant. This formulation was derived from the study of oxidation of pyrolytic graphite. The kinetic expression above is based on the assumption that the CO radical is the primary product formed and that there are two active reaction sites on graphite.

7.4.5 Oxidation by OH

In the oxidation of commercial graphite at conditions of P_{O_2} of 0.04 – 0.30 atm and temperatures in the range of 1530 – 1890 K, Fenimore and Jones (1967) found there was little dependence of the reaction rate on the partial pressure of oxygen, P_{O_2} . Oxidation rates were found to be a factor of 5 higher than when only oxidation via O_2 was considered. It was then suggested the increased oxidation was on account of OH oxidation. The oxidation rate via OH is given by Eqn. (7.14) below:

$$\alpha_4 = L_{\alpha 4} \times \gamma_{OH} \times X_{OH} \times T^{-1/2} \times \exp\left(\frac{-19,023}{T}\right) \times S, \quad (7.14)$$

where γ_{OH} is the soot-OH collision efficiency, taken to be 0.1, and X_{OH} is the OH molar fraction. $L_{\alpha 4}$ is a model constant. The effect of the six model constants $L_{\alpha 1}, E_{\alpha 1}, L_{\alpha 2}, E_{\alpha 2}, L_{\alpha 3}, L_{\alpha 4}$, on the overall soot f_v will be studied below. Focus is placed primarily on soot f_v as experimental measurements of number density are not available and it would be difficult to compare model results with measured results when it is employed for diesel and biodiesel combustion. For this reason, the constant in Eqs. (7.4) and (7.7) are not varied.

7.5 Sensitivity Analysis of the Model

The values of the six constants ($L_{\alpha 1} \dots L_{\alpha 4}$) chosen for the sensitivity study are listed in Table 7.1. Notice that for each constant, three values are considered (baseline, Case 1, and Case 2). Soot f_v profiles will be presented at a time of 3 ms after ignition, a residence time typical of combustion duration in diesel engines. In this work, the time of ignition is defined as that when the peak flame temperature exceeds 1,500 K.

Table 7.1: Values of constants selected for sensitivity study.

Constant (Eqn #)	$L_{\alpha 1}$ (1)	$E_{\alpha 1}$ (1)	$L_{\alpha 2}$ (2)	$E_{\alpha 2}$ (2)	$L_{\alpha 3}$ (3)	$L_{\alpha 4}$ (4)
Baseline	100	-1000	100	-1000	1	1
Case 1	200	-5000	200	-2000	500	500
Case 2	300	-10000	300	-3000	1000	1000

Figure 7.2 shows the results for the surrogate fuels for hydrocarbon diesel, where the sensitivity study results are presented. Figures 7.2(a)-(d) show the effect of changes to the inception linear term $L_{\alpha 1}$, inception exponential term $E_{\alpha 1}$, surface growth linear term $L_{\alpha 2}$, and surface growth exponential term $E_{\alpha 2}$, respectively. Figures 7.2(e) and (f) show the effect of

changes to the O_2 and OH oxidation model constants, $L_{\alpha 3}$ and $L_{\alpha 4}$, respectively. In each case, only one constant is changed (at a time) while keeping other constants at their baseline values. Figure 7.2(a) shows that the increase of $L_{\alpha 1}$ from 100 to 200, and then to 300, results in relatively small change to the peak soot f_v , suggesting that the sensitivity to this term is weak. Changing $E_{\alpha 1}$ shows a reduction in peak soot f_v , and a shift in the corresponding mixture fraction, as seen in Fig. 7.2(b). This is reasonable as there is higher temperature toward the stoichiometric mixture fraction, causing a shift in the peak soot f_v towards the stoichiometric mixture fraction.

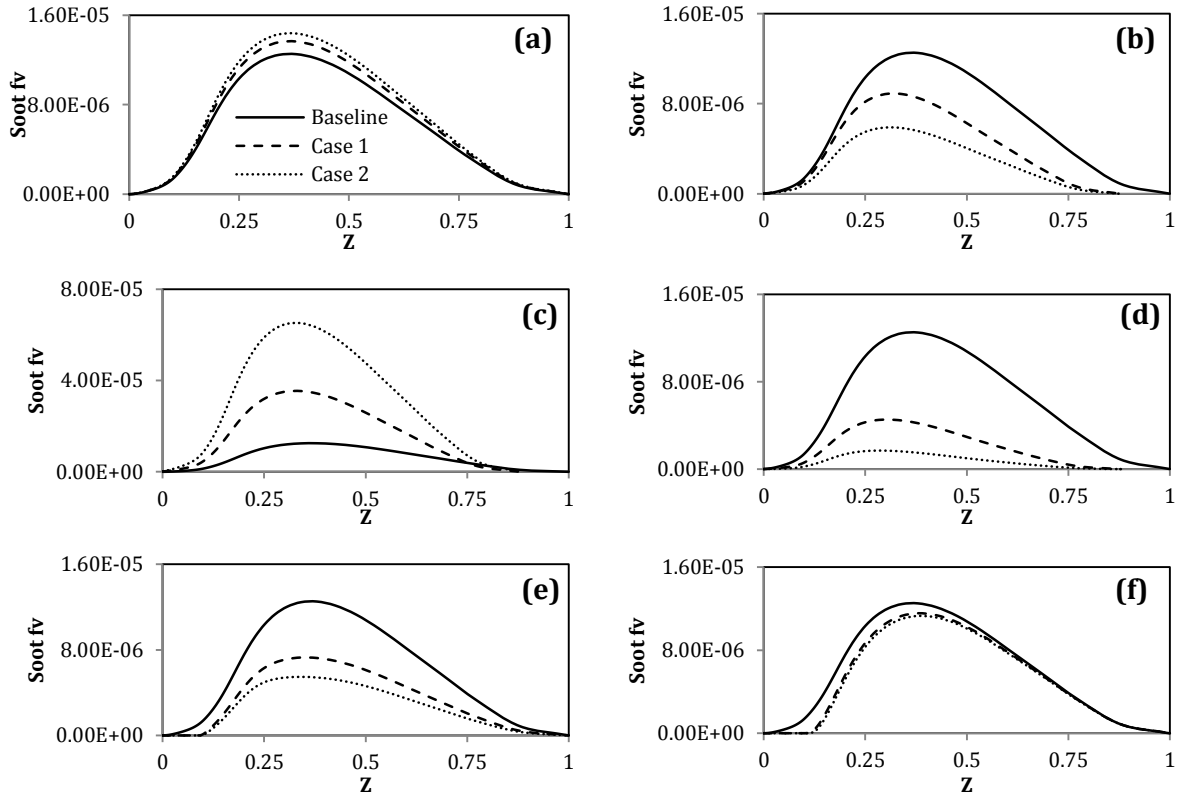


Figure 7.2: Predicted soot volume fraction for varying values of $L_{\alpha 1}$, $E_{\alpha 1}$, $L_{\alpha 2}$, $E_{\alpha 2}$, $L_{\alpha 3}$ and $L_{\alpha 4}$ as listed in Table 2 are shown in (a)-(f), respectively. The line types are identified in (a).

Compared to the inception source term, the soot f_v has a greater sensitivity to changes in surface growth. In Fig. 7.2(c), changes to $L_{\alpha 2}$ results in a significant shift in the peak soot f_v , compared to changes in inception. Recall from earlier discussion that the C_2H_2 mass fraction is about three orders of magnitude higher compared to C_2H_3 and so the surface growth term is dominant in soot formation. When $E_{\alpha 2}$ is changed (Fig. 7.2(d)), the peak soot f_v and the corresponding mixture fraction show changes that are similar to the effects observed when $E_{\alpha 1}$ is changed although the magnitude of the reduction in peak soot f_v is more significant. In addition, when $E_{\alpha 2}$ is increased, the ratio of peak soot f_v between diesel and biodiesel was noticed to increase as well. Figure 7.2(e) shows the effect of changes in the O_2 oxidation term. Of note is the complete elimination of soot in the regions leaner than stoichiometric as

compared to the baseline case. The response of soot f_v to changes in the OH oxidation model constant is less evident compared to the changes in the O₂ model constant. When OH oxidation is increased, the peak soot f_v does not decrease dramatically as shown in Fig. 7.2(f). Additional simulations that we have carried out show that the responses to changes to the linear and exponential terms are very similar between the diesel and biodiesel fuel surrogates.

Having understood the sensitivities of each term in the two-equation model, the soot f_v profile can be optimised with the two-equation soot model to match the results of the ABF soot model. We proceeded to do this as follows. First, $E_{\alpha 1}$ is varied to match the peak soot f_v mixture fraction for both surrogate fuels to that of the ABF soot model. $E_{\alpha 1}$ is chosen as it shifts the mixture fraction of peak soot f_v for both surrogate fuels simultaneously, without altering the ratio of peak soot f_v . Then, $E_{\alpha 2}$ is varied. This changes the ratio of the peak soot f_v of diesel and biodiesel to match the difference expressed in ABF soot model. Thirdly, $L_{\alpha 1}$ or $L_{\alpha 2}$ are varied to match the peak soot f_v magnitude. $L_{\alpha 1}$ is used to effect smaller changes and $L_{\alpha 2}$ for larger changes. Using this approach, a preliminary set of values of the various constants is selected. For this set, the model constants in the oxidation terms are unchanged from the original values in the literature, for sake of simplicity, although it has been suggested by prior studies that these constants would also have to be changed. The preliminary set of values of the constants is listed in Table 7.2.

The resulting soot f_v profiles for biodiesel and diesel obtained from this two-equation soot model are shown in Fig. 7.3 for two values of χ_{st} of 5 s⁻¹ (a) and 10 s⁻¹ (b) that are representative of scalar dissipation rate values in the diesel spray downstream of the lift-off length. For comparison, the results obtained using the ABF model are also presented. It can be clearly seen that the soot f_v at leaner mixtures (mixture fraction $Z < 0.1$) is significantly over-predicted. In addition, the peak value of the soot f_v predicted for the diesel surrogate with the two-equation soot model is greater than that predicted by the ABF model by almost a factor of 4 when χ_{st} of 10 s⁻¹.

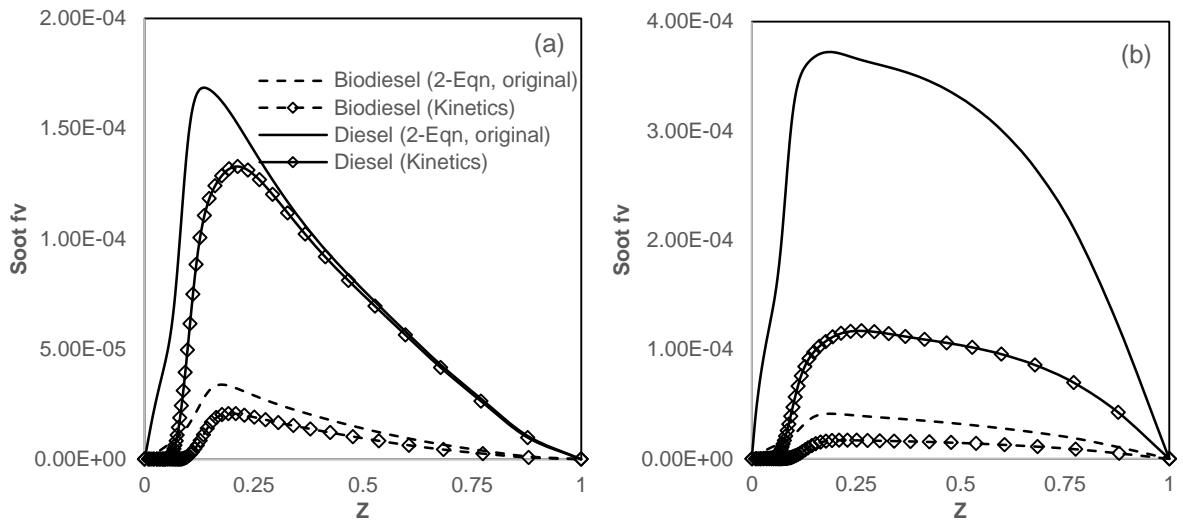
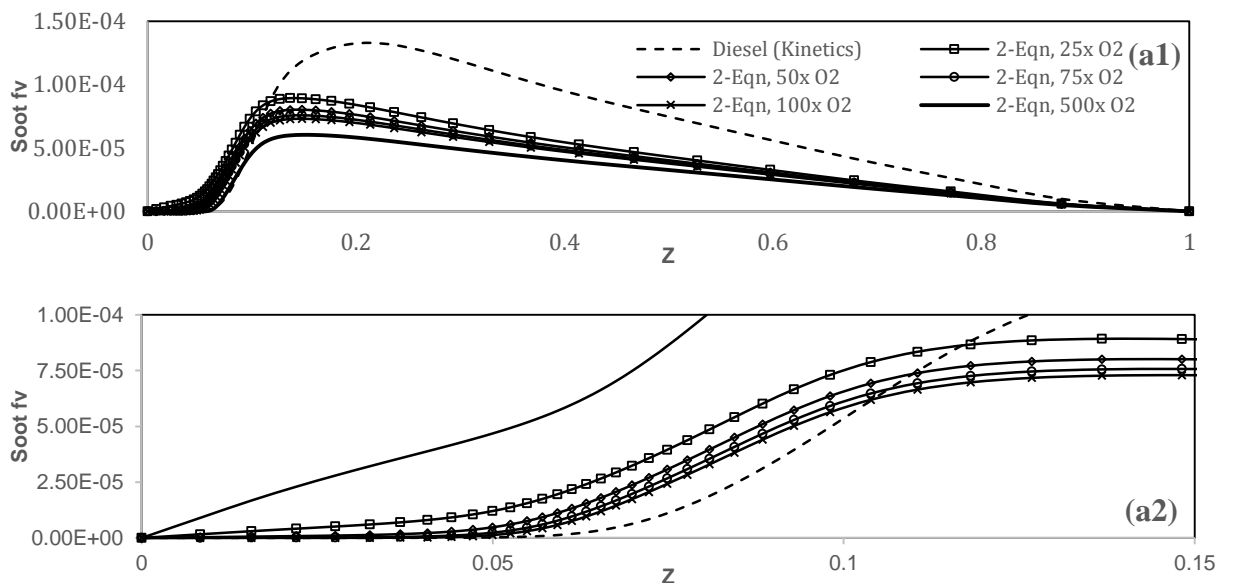


Figure 7.3: Predicted soot volume fractions with the preliminary set of constants in the two-equation model compared with the predictions of the ABF model.

7.5.1 Addressing Soot Oxidation in Lean Mixtures

The over-prediction of soot f_v in leaner mixtures appears to be related to the oxidation rates. Recall that the oxidation rates employed are unchanged from the original values suggested in the literature when the oxidation models are presented. Figure 7.4 show soot f_v for the diesel surrogate when the O_2 oxidation term is increased by factors of 25, 50, 75 and 100. Figure 7.4(a) shows the results across the entire mixture fraction (Z) space, and Fig. 7.4(a2) zooms into the Z -space of 0 – 0.15. When the factor is 25, there is a dramatic decrease in soot in the lean mixture fraction region and the peak soot f_v also decreases significantly. It is clear that if the O_2 oxidation factor is increased sufficiently, the lean ($Z < 0.05$) region of the flame can eventually have soot volume fractions similar to that predicted by the ABF model. Increasing the oxidation rate (via the O_2 route) alone, however, reduces the peak soot volume fraction to values lower than that predicted by the ABF model.



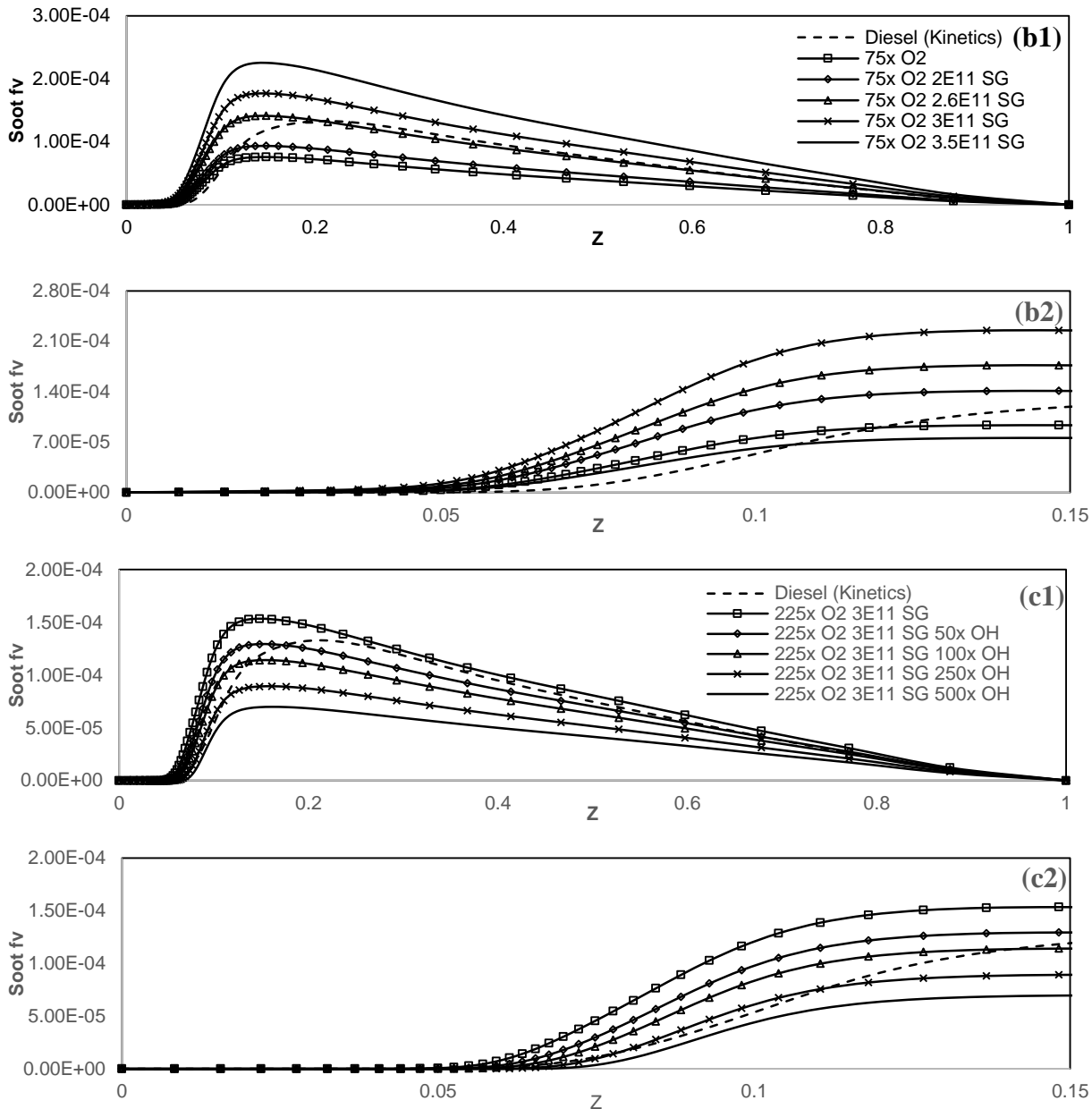


Figure 7.4: Soot volume fraction when (a) $L\alpha_3$ is increased for the diesel surrogate, (b) $L\alpha_2$ increased with a constant $L\alpha_3$, and (c) $L\alpha_4$ increased with a constant $L\alpha_2$ and $L\alpha_3$. (a2), (b2) and (c2) show zoomed region of $Z = 0 - 0.15$.

From the sensitivity study in Section 7.5, we concluded that to increase the peak soot f_v , increasing the soot surface growth term offers the greatest sensitivity. It also has the benefit of increasing the peak soot f_v for diesel and biodiesel by similar proportions, thus maintaining the ratio of peak soot f_v between the two fuels. Figure 7.4(b1) shows the results for the diesel surrogate fuel when the O_2 oxidation rate is increased by a factor of 75 and the surface growth term is modified relative to the original values. The surface growth (“SG” in Fig. 7.4) is varied between $2.0E11$ to $3.5E11$. But, Fig. 7.4(b2) shows that increasing the surface growth rate increases the soot f_v in the leaner Z -space, undoing the effect of increased O_2 oxidation. This can be addressed by further increasing the O_2 oxidation rate but the effect is to shift the value of Z at which peak soot f_v is observed. To address this, we examine the OH oxidation term.

Figure 7.4(c1) shows results when the O₂ oxidation rate is increased by a factor of 225, the surface growth rate constant is 3.0E11 and the OH oxidation rate is increased in steps. Increasing OH oxidation encourages a much stronger response of the peak soot f_v compared to increasing the O₂ oxidation.

The optimisation process have been described in some detail so that other researchers may be able to use this model and optimise it for their specific problems. The final and optimised two-equation soot model constants are presented in Table 7.2.

Table 7.2: Model constants.

Constant (Eqn #)	L _{α1}	E _{α1}	L _{α2}	E _{α2}	L _{α3}	L _{α4}
Preliminary Values	625	-10,000	2.5 x 10 ¹¹	-40,000	1	1.63 x 10 ¹¹
Optimised Values	625	-10,000	3.0 x 10 ¹¹	-40,000	200	8.15 x 10 ¹³

The resulting soot f_v profiles for biodiesel and diesel surrogates obtained are shown in Fig. 7.5 for two values of χ_{st} of 5 s⁻¹ (a) and 10 s⁻¹ (b). Results from the ABF model are also shown. There is good agreement between the two-equation soot model results and the ABF model results across the range of Z values for both surrogates. Comparing the computational time required when employing the two-equation soot model to that required with the ABF mechanism, there is an order of magnitude saving in time. This makes the two-equation soot model developed in this work an effective tool for engine researchers.

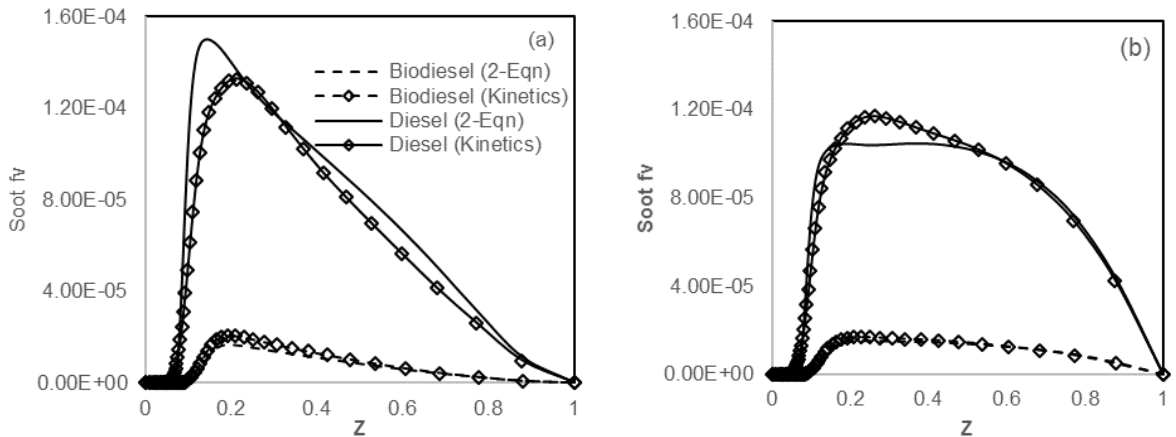


Figure 7.5: Soot volume fraction predicted by the two-equation soot model compared to the ABF soot model for χ_{st} of a) 5/s and b) 10/s.

7.6 Conclusion and Summary

In this Chapter, a semi-empirical two-equation soot model is developed. This soot model employs the vinyl radical as the soot inception species, acetylene as surface growth, and oxidation via O_2 and OH . The soot model was developed based on a kinetics-based soot model. From a sensitivity analysis, the soot model was optimised. Compared to the kinetics-based soot model, it offers very good accuracy and at great computational economy.

8 Modelling Diesel Sprays with Two-Equation Soot Model

8.1 Introduction

In this Chapter, the semi-empirical two-equation soot model developed will be applied to nine cases of diesel sprays under engine conditions. Section 8.2 expands the computational conditions. Section 8.3 briefly outlines the alternative soot models used for comparison. Section 8.4 presents the results of spray comparisons and their discussion. Finally, this chapter will close with a summary and conclusions in section 8.5.

8.2 Computational Conditions

To validate the accuracy of the two-equation soot model developed (henceforth known as the “CYA soot model”), it will be used to model soot in n-heptane sprays for a range of conditions that reflect changes in injection pressure, chamber temperature, chamber density, chamber oxygen mass fraction, and orifice diameter in a diesel engine. The predictions will be compared with available measured results taken from the Engine Combustion Network (www.sandia.gov/ecn/). In addition, a second two-equation soot model (Leung et al., 1991) that has been widely employed for modelling soot in turbulent jets (Xu et al., 1997; Beltrame et al., 2001; Liu et al., 2003), including in diesel engines (Hong et al., 2005; Tao et al., 2009; Bolla et al., 2013), will also be employed and the results from the two models compared. Finally, the two-equation soot models will also be compared to a kinetics-based soot model (Appel et al., 2000).

Similar to the previous studies, n-heptane (C_7H_{16}) is used as the surrogate fuel for diesel fuel as it has been shown to represent the chemical kinetics of diesel fuel reasonably well (Chen et al., 2012). A 44-species skeletal n-heptane mechanism was chosen as it offers a good balance between computational economy and accuracy (Liu et al., 2004). In addition, this mechanism contains the vinyl radical (C_2H_3) which is used in the CYA soot model as the soot inception species. For the ABF soot mechanism, a 160-species reduced n-heptane mechanism was selected (Seiser et al., 2000) as it is large enough to support the ABF soot mechanism and offer good coupling (Hoffman and Abraham, 2009). Even though this paper will not focus on NO modelling, it is important to include the NO mechanism because of its effect on the formation of soot (Westbrook and Dryer, 1984; Abian et al., 2014). For this study, we will be using the NO kinetics from the GRI-Mech 3.0 mechanism (Smith et al., 1999).

As pointed out earlier, the conditions employed for the study reflect conditions in a diesel engine. The computations and the corresponding measurements were carried out in a

constant-volume chamber. The ABF soot mechanism has already been applied to compute these sprays in the past, and it has been shown that there is a correlation of the computed flame lift-off length to the predicted soot volume fraction (f_v) in the domain (Yen and Abraham, 2014, 2015). For comparison, and completeness, the results of soot predictions obtained using the ABF soot mechanism will also be shown alongside the two-equation soot model results in this paper. Table 8.1 shows the list of conditions employed in this study. Measurement conditions change in each case compared to the baseline (Case 1). These conditions correspond to conditions of spray measurements made at Sandia National Laboratories (www.sandia.gov/ecn). From left, they are: nozzle diameter, injection pressure, ambient gas pressure, ambient gas temperature, ambient gas density, and ambient O₂ concentration. Soot measurements are not available for all these cases. The measured results will be shown alongside the predicted results when they are available.

Table 8.1: Computational conditions for the n-heptane spray. Parameter changed in each case in **bold** and underlined.

Case	d (mm)	ΔP (MPa)	P_g (bar)	T_g (K)	ρ_g (kg/m ³)	O ₂ %
1	0.1	150	42.66	1000	14.8	21
2	0.1	<u>60</u>	42.66	1000	14.8	21
3	0.1	150	55.45	<u>1300</u>	14.8	21
4	0.1	150	38.39	<u>900</u>	14.8	21
5	0.1	150	43.02	1000	14.8	<u>15</u>
6	0.1	150	43.20	1000	14.8	<u>12</u>
7	0.1	150	43.45	1000	14.8	<u>8</u>
8	<u>0.18</u>	140	42.66	1000	14.8	21
9	0.1	150	<u>86.47</u>	1000	<u>30.0</u>	<u>15</u>

8.3 Other Soot Models Considered

To validate the accuracy of the developed soot model, it will, in addition the measured data, be compared to another two-equation soot model, and a kinetics-based soot model. These will be elaborated in the following sections.

8.3.1 Leung et al Two-Equation Soot Model

The results from the developed soot model will be compared to results obtained by employing the Leung et al. soot model (1991). The Leung et al. soot model (henceforth known as the “LLJ soot model”) has been well studied (Kennedy, 1997; Stanmore et al., 2001; Frenklach, 2002) and will provide a good benchmark for the two-equation soot model developed by the authors. In the LLJ soot model, acetylene is proposed to be responsible for

both soot inception and surface growth. Oxidation is considered to be via O₂ by using the Lee et al. model (1962). As indicated earlier, the primary motivation for the development of a two-equation soot model by the authors was to employ one model for both diesel and biodiesel fuels. As the LLJ soot model uses acetylene as the inception species, this model cannot be used for both diesel and biodiesel flames (please see Section 6.3). This is due to the acetylene mass fraction being very similar in the oxidation chemistry of the two fuels, so it cannot explain observed differences in soot f_v . To summarise, the source terms of this soot model are as follows:

$$\text{Inception (mass): } R_1 = 10,000 \times \exp\left(-\frac{21,100}{T}\right) \times x_{C_2H_2}, \quad (8.1)$$

$$\text{Surface growth (mass): } R_2 = 6,000 \times \exp\left(-\frac{12,100}{T}\right) \times x_{C_2H_2} \times \sqrt{S}, \quad (8.2)$$

$$\text{Oxidation (mass): } R_3 = 10,000 \times \sqrt{T} \times \exp\left(-\frac{19,680}{T}\right) \times S \times x_{O_2}, \quad (8.3)$$

$$\text{Inception (number density): } R_4 = \frac{2}{C_{min}} N_A R_1, \quad (8.4)$$

$$\text{Agglomeration (number density): } R_5 = k_4 \times \left[\frac{\rho y_s}{M_{C(s)}}\right]^{\frac{1}{6}} \times [\rho N]^{\frac{11}{6}}, \quad (8.5)$$

$$k_4 = 2 \times C_a \times \left(\frac{6M_{C(s)}}{\pi\rho_{C(s)}}\right)^{\frac{1}{6}} \times \sqrt{\left(\frac{6KT}{\rho_{C(s)}}\right)}, \quad (8.6)$$

where x_A is the mole fraction of species A, S is the surface area of the soot particle (Eq. (7.6)), and C_{min} is the inception diameter of the soot particle, taken to be 100 atoms. N_A is Avogadro number, $M_{C(s)}$ is the molar mass of carbon, taken to be 12.011 kg/kmol, and $\rho_{C(s)}$ is the density of soot, taken to be 1.8 kg/m³. K is the Boltzmann constant and C_a is the agglomeration rate constant, recommended to be 9. The soot mass and number density equations are thus:

$$\frac{d\rho y_s}{dt} = R_1 + R_2 - R_3, \quad (8.7)$$

$$\frac{dN}{dt} = R_4 - R_5, \quad (8.8)$$

where ρy_s is the soot volume fraction, and N is the soot number density.

8.3.2 Kinetics-based Soot Model

For the kinetics-based soot model, this study once again employs the work of Appel et al. (2000). Henceforth known as the “ABF soot mechanism”, it assumes that soot is formed via the pathway of aromatic species. And addition of carbon in the means of acetylene. Please see Section 2.4 for more information. The ABF soot mechanism consists of 101 species and 546 steps. This will be added to the petrodiesel and biodiesel surrogate mechanisms.

8.4 Results and Discussion

Figure 8.1 shows computed flame temperature contours at 4 ms after start of injection (ASI) for the nine cases of Table 8.1. Taking Case 1 as a baseline, the lower injection pressure of Case 2 relative to Case 1 reduces the amount of fuel injected into the cylinder and the lower injection velocity reduces the local scalar dissipation rate (χ) in the jet, which reduces the flame lift-off length (LoL). The χ is higher near the orifice and then decreases downstream in the jet. The LoL can be correlated with the ignition χ for the mixture (Yen and Abraham, 2014, 2015). The ignition χ (χ_{ign}) is that value of the scalar dissipation rate above which ignition will not occur. Since the chamber temperature and density in Cases 1 and 2 do not change, the χ_{ign} remains unchanged, but in the jet that χ occurs closer to the orifice. In Case 3, the increased ambient temperature of 1,300 K increases the χ_{ign} and causes the LoL to reduce as a flame can be sustained closer to the orifice where the χ is higher. In Case 4, the LoL is increased relative to Case 1 because the lower temperature reduces the χ_{ign} . This reduced χ is located farther from the orifice than in Case 1. In Cases 5 – 7, the progressive reduction in ambient O₂ % reduces the χ_{ign} . This increases the LoL. In Case 8, an increase in the fuel flow rate on account of the increased orifice diameter increases the injected momentum but also mixing which reduces the local χ . This, in turn, causes the LoL to shorten. The LoL in Case nine is shorter than in Case 5 (the other case with 15 % ambient O₂), because of the increased mixing on account of higher chamber density.

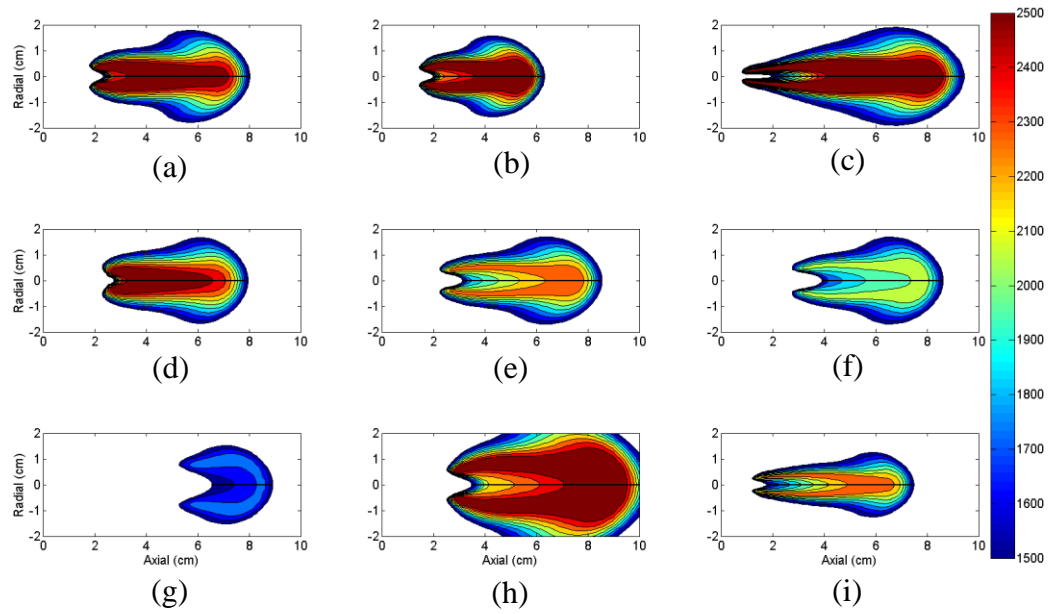


Figure 8.1: Temperature contours for the nine cases at 4 ms ASI with (a) – (i) representing Cases 1 – 9, respectively.

Figure 8.2 shows the soot f_v contours for the nine cases from Table 8.1 at 4 ms ASI for all nine cases. The same contour scales are used for all cases so that the relative difference in soot f_v is clear in the images. In general, the higher the LoL, the lower the soot in the domain. The higher LoL results in greater entrainment of chamber air upstream of the LoL which results in increased oxidation. Quantitative comparisons of predicted soot with measured values over a broad range of conditions are very challenging with available models, especially with empirical and semi-empirical models. Only a qualitative comparison will be presented.

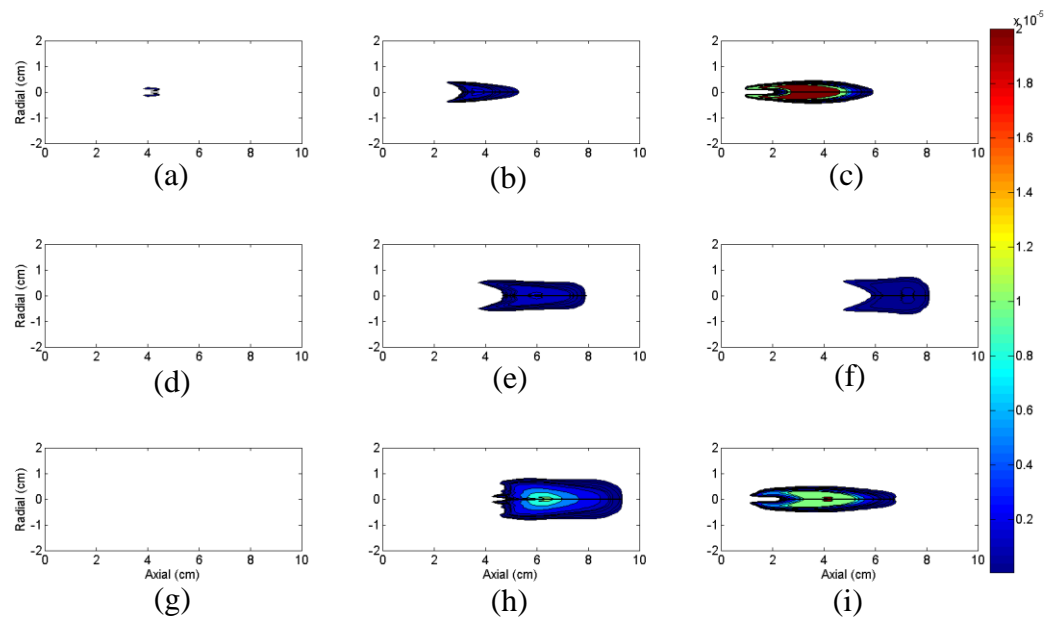


Figure 8.2: Soot volume fraction contour for the nine cases at 4 ms ASI.

Predicted results obtained along the axis of the spray from the three models: the two-equation CYA soot model, the two-equation LLJ soot model and the detailed kinetic ABF soot mechanism, are compared to the measured soot data in a qualitative sense in Fig. 8.3. Four cases of measured data are available and shown. A fifth case, Case 7, is not shown as there is negligible soot in the measurements and the predictions. In addition, the measured results have been smoothed via local regression using weighted linear least squares and a 1st degree polynomial model to a span of 0.1. To compare the soot f_v qualitatively, the jet centreline soot f_v in each of the cases is normalised by their corresponding maximum values and plotted against axial distance. Considering the four cases shown and the three models employed, the predicted and measured results agree quite well. In particular, the axial changes in peak soot location with changes in operating conditions are predicted well. Interestingly, the three models show similar results. Differences between predictions and measurements, and between the predictions themselves, will be highlighted in the discussion that follows.

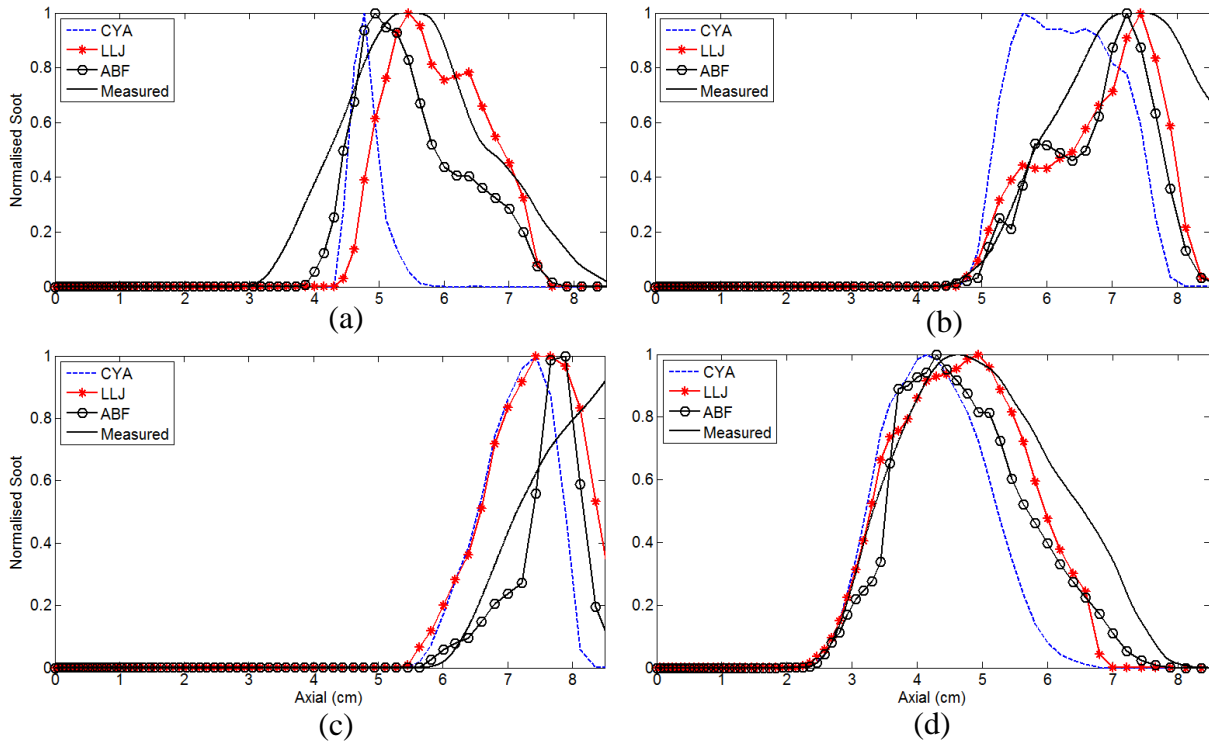


Figure 8.3: Soot volume fraction with respect to axial distance at the centreline for Cases 1, 5, 6, and 9 at 4 ms ASI with (a) - (d) representing them, respectively. Soot is normalised in each case independently.

In Case 1 (Fig. 8.3(a)), the peak soot f_v of the measured data and predicted results are within 10 %. However, the CYA soot model has a much narrower distribution. Given that the soot f_v increases in magnitude at roughly the same location upstream for all lines (3.5 – 4.5 cm axially), the most reasonable explanation for the narrow peak of the CYA would be the higher influence of the O_2 oxidation sub-model. In Case 5 (Fig. 8.3(b)), ambient O_2 is reduced to 15 %. This

(d)

reduces the effect of the O₂ oxidation component of the CYA soot model compared to the others. Thus, the distribution of soot f_v in the CYA spreads both farther downstream and upstream. It appears that for this case, the reduction of soot oxidation from the drop in O₂ plays a bigger role than the reduction of soot formation on account of reduced temperature. In the case of 12 % ambient O₂ (Fig. 8.3(c)), the three soot models predict soot upstream of the measured results, showing the challenge in predicting soot in very lean conditions. Fig. 8.3(d) can be compared to Fig. 8.3(b) as the conditions in both cases correspond to 15 % ambient O₂, but the former has a higher gas density, at 30.0 kg/m³ compared to 14.8 kg/m³ of the latter. An increase in density increases the chemical reaction rates. In general, the models appear to predict faster oxidation. As a result, the predicted soot decreases to negligible values upstream of the axial distance where the measured soot decreases to such values.

Figure 8.4 compares the soot f_v contours from the measured data, ABF kinetics model, CYA soot model, and LLJ soot model. Measured data is only available for Cases 1, 5, 6, 7, and 9. Thus, only these cases will be shown. Contour levels differ for each case. The three soot models predict the axial location of the peak soot in each case quite well. Both the ABF and CYA predict soot worse than the LLJ in Case 1. But in Cases 5, 6 and 9, the ABF and CYA perform slightly better. In general, the soot profile predicted by the CYA soot model is similar to the ABF kinetics model as the latter was used as a benchmark. The results are encouraging in that the changes in the axial peak soot location and in total amount of soot with changes in chamber and injection conditions are predicted qualitatively correctly. Quantitative comparisons are unrealistic, but it is noted that the predicted results are generally within an order of magnitude of the measured results.

8.5 Summary and Conclusions

In this work two semi-empirical soot models and one kinetics-based soot model are employed to compute soot in nine n-heptane sprays. The nine sprays represent changes in injection pressure, chamber temperature, ambient O₂ %, orifice radius, and chamber density. The predictions of the two semi-empirical models and the kinetics model are similar. Measured soot distributions are available for five of the nine cases. When comparing the predicted and measured soot distributions, the semi-empirical two-equation soot models are found to predict the measured distribution just as well as the kinetics soot model.

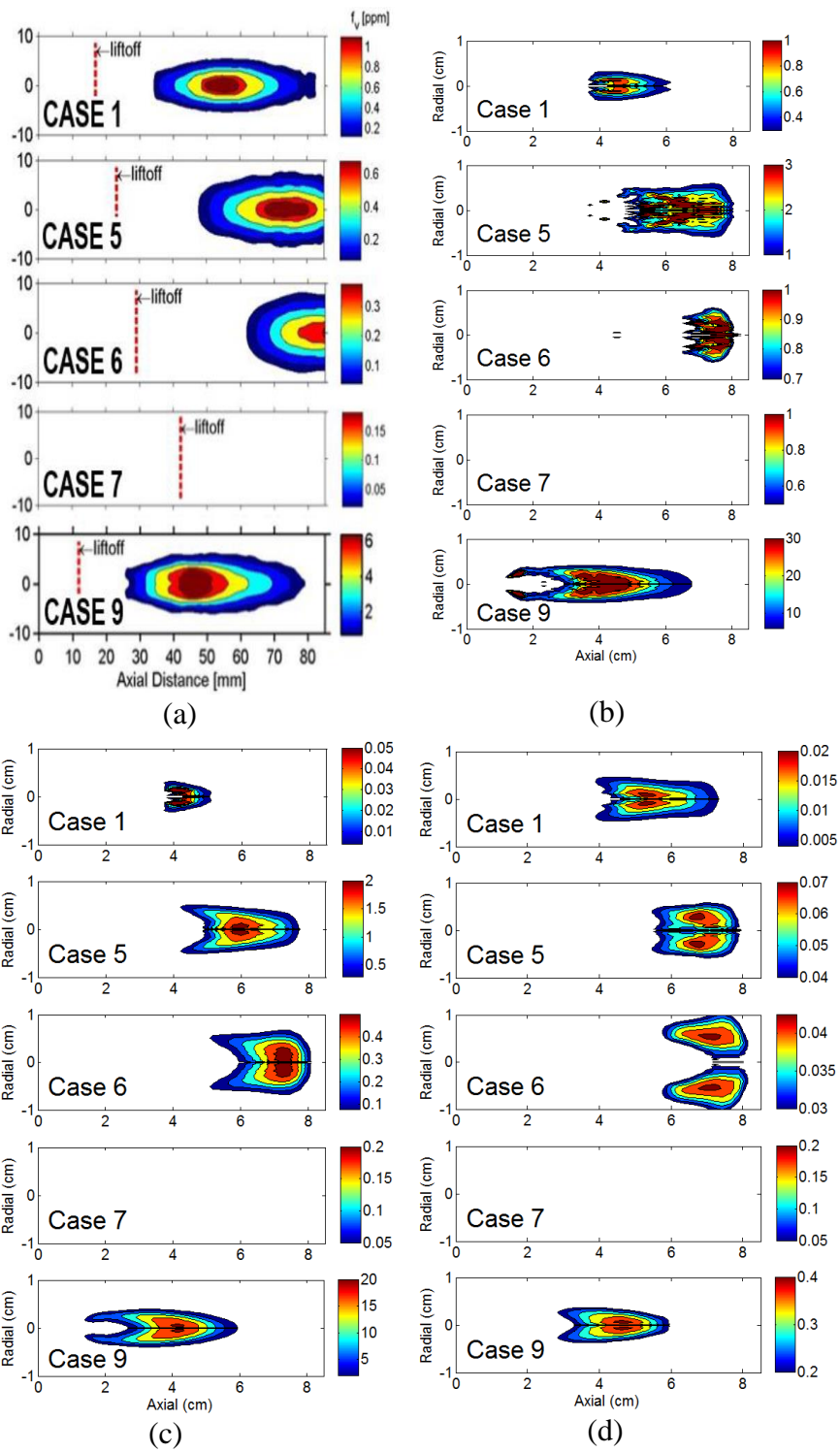


Figure 8.4: Soot volume fraction comparison between measured data (a), ABF kinetics soot mechanism (b), CYA soot model (c), LLJ soot model (d). Cases 1, 5, 6, 7 and 9 are compared. Measured data is from Engine Combustion Network (www.sandia.gov/ecn/).

9 Biodiesel and Diesel Sprays

9.1 Introduction

In this Chapter, the two-equation soot model that was developed and validated will be applied to biodiesel and diesel sprays. The two-equation soot model will be compared to measured results of Nerva et al. (2012). Section 9.2 will outline the computational method in this study. Section 9.3 will present the results and discussion. Finally, section 9.4 will close this study with a summary and conclusions.

9.2 Computational Conditions

In this study, computed results of biodiesel and diesel sprays will be presented. Some of the results will be compared with measured results from Nerva et al. (2012). Diesel and biodiesel sprays will be simulated in a constant-volume chamber. The chamber conditions reflect those in an engine with exhaust gas recirculation (EGR). The authors are, in particular, interested in determining if a semi-empirical two-equation soot model previously developed (Cai and Abraham, 2015; Cai et al., 2015) and detailed in Section 7.4, can predict the measured differences in soot in diesel and biodiesel sprays.

Similar to the previous studies, the 44-species n-heptane chemical kinetics mechanism developed by Liu et al. (2004) is chosen to represent diesel oxidation. The mechanism was chosen as it was relatively compact, and found to match experimental pre-mixed ignition delay times at various temperatures reasonably well (Wang and Rutland, 2003). Most importantly, the mechanism contains the vinyl radical (C_2H_3) and acetylene (C_2H_2) species for soot inception and surface growth, respectively, in the two-equation soot model. For biodiesel kinetics, a 115-species skeletal mechanism developed by Luo et al. (2012) was chosen. Derived from a detailed biodiesel kinetics soot mechanism (Herbinet et al., 2010), the 115-species mechanism also uses a tri-component fuel surrogate consisting of n-heptane, methyl decanoate (MD) and methyl-9-decenoate (MD9D) in the ratio of 2:1:1, respectively. The 115-species mechanism matched both the detailed mechanism and measured data well in terms of ignition delay and species profiles in a jet-stirred reactor. Again, the existence of the C_2H_3 and C_2H_2 species was critical.

NO is also modelled as soot predictions have been found to be sensitive to NO concentrations (Westbrook and Dryer, 1984; Abian et al., 2004). NO formation is modelled using a sub-mechanism taken from GRI Mech 3.0 (Smith et al., 1999). Unlike species mass fractions and temperature, which reach an equilibrium over time, soot volume fraction (f_v) and

soot number density (N) continue to grow during the time of injection. Thus, a tracer particle is injected along with the fuel to track the residence time of the injected mass within the domain. These tracers are modelled using the LDEF approach as discussed in Section 3.3. Instead of the progress variable (C), the tracer residence time is employed along with mixture fraction (Z) and scalar dissipation rate (χ) to tabulate f_v and N in the domain.

The predictions of soot from diesel and biodiesel combustion were compared to experimental results obtained by Nerva et al. (2012). The experimental studies of non-reacting and reacting sprays of soy-derived biodiesel (SME) and #2 diesel fuel were performed under diesel engine operating conditions in a constant-volume chamber. Fuel was injected using a Bosch common rail injector through a single nozzle of 90 μm diameter at an injection pressure of 150 MPa. This injector setup is similar to the ‘Spray A’ setup of the Engine Combustion Network (www.sandia.gov/ecn/). The fuel temperature for SME and #2 diesel was 363 K and 373 K, respectively. Two ambient gas temperature conditions were considered: 900 and 1,000 K. The ambient gas density was 22.8 kg/m^3 . The reacting phase of the work limited the ambient O_2 concentration to 15 %. This would represent conditions in a typical diesel engine with exhaust gas recirculation (EGR). To summarise, Table 9.1 shows the conditions of the study.

Table 9.1: Constant-volume chamber conditions for the reacting jet study.

Property	Nerva et al. (2012)
Gas density (kg/m^3)	22.8
Ambient temperature (K)	900,1000
Fuel temperature (K)	363 (biodiesel), 373 (diesel)
Nozzle diameter (μm)	90
Injection pressure (MPa)	150
Injection duration (ms)	4
O_2 %	15

9.3 Results and Discussion

Figure 9.1 shows the computed and measured liquid-phase penetrations. The penetration is shown as a function of time after start of injection (ASI). Results are shown for two temperature conditions, 900 K (Fig. 9.1(a,b)) and 1000 K (Fig. 9.1(c,d)). Penetrations in non-reacting cases are shown in Fig. 9.1(a,c), and reacting sprays are shown in Fig. 9.1(b,d). The results agree within about 30 % for the reacting and non-reacting diesel sprays and within 50 % for the biodiesel sprays suggesting that the properties of the biodiesel surrogate fuel may be less accurate than of the diesel surrogate fuel.

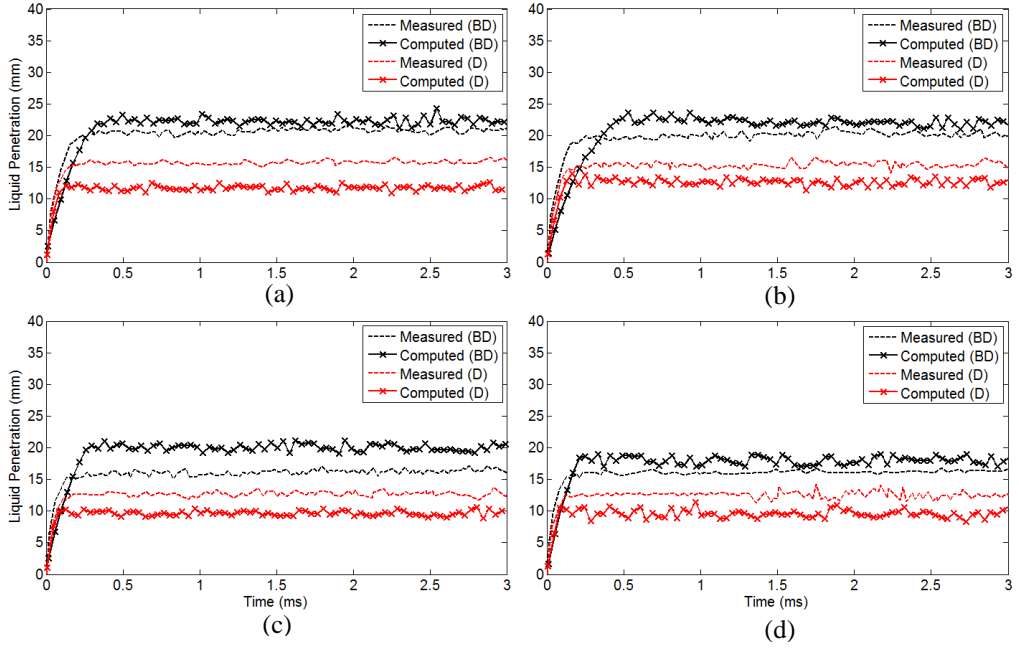


Figure 9.1: Non-reacting and reacting liquid penetration plotted against time. 900 K ambient (a,b) and 1000 K ambient (c,d). Non-reacting (a,c), reacting (b,d).

Beyond the maximum penetration distance of the liquid, the fuel continues to penetrate as vapour. In Fig. 9.2 the vapour-phase fuel penetration is shown as a function of time ASI. Measured data is only available for the 900 K non-reacting sprays, but computed results are shown also for 1000 K. The penetration is obtained by determining the axial distance where the Z has decreased to a certain value. Fig. 9.2(a) shows the computed penetrations when this value is 0.0025, and Fig. 9.2(b) shows the penetrations when the value is 1×10^{-6} . An analytical solution to the tip vapour penetration is also shown in Fig. 9.2. It has been derived as (Bajaj et al., 2011):

$$x_{tip}^2 = C_t d (\rho_l / \rho_\alpha)^{0.5} U_i t, \quad (9.1)$$

where C_t is a constant of 6.51, d is the nozzle diameter, ρ_l and ρ_α is the fuel and ambient gas density, respectively, U_i is the injection velocity, and t is time. Expanding the injection velocity term results in:

$$x_{tip}^2 = 6.51 d (2\Delta P / \rho_\alpha)^{0.5} t, \quad (9.2)$$

where ΔP is the injection pressure.

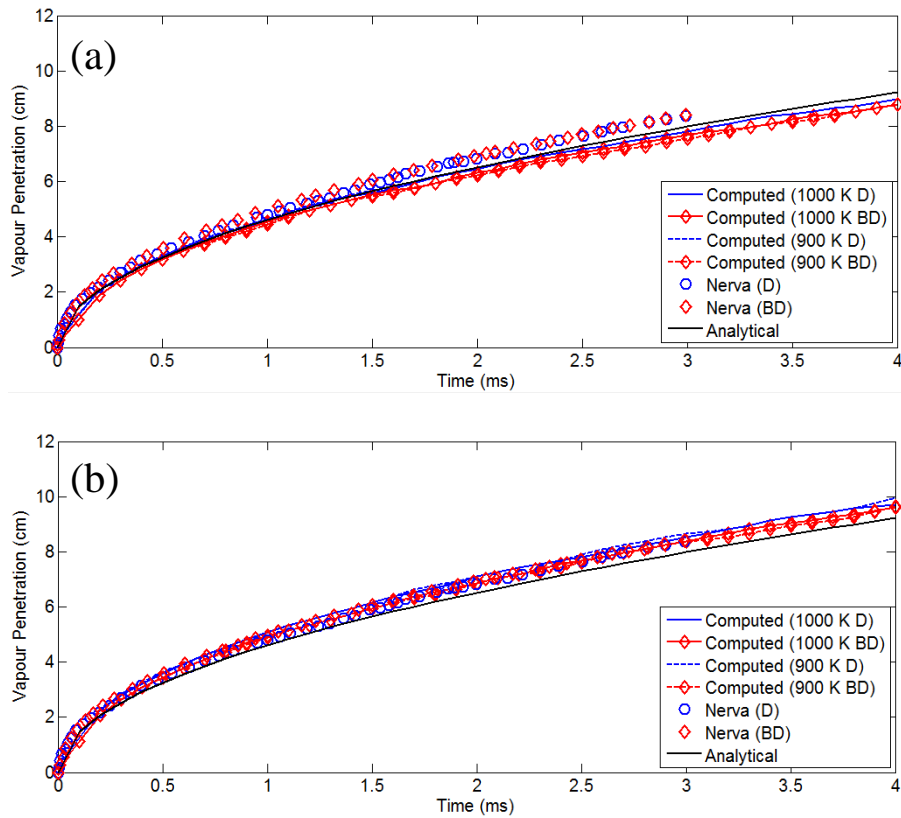


Figure 9.2: Spray penetration as a function of time when the spray tip is identified as the location where the mixture fraction is (a) 0.0025, and (b) 1E-6.

From Fig. 9.2, it can be concluded that while the penetrations are affected by the definition of the tip, for the two values of mixture fraction selected to define the tip, the differences are within 10%. Furthermore, both the experimental and computed results suggest that the differences between diesel and biodiesel penetrations are negligible. This is not surprising as the penetrations are momentum controlled.

Figure 9.3 shows the Z contour plot of the four cases. Clockwise from the top left, they are: 900 K biodiesel, 900 K diesel, 1000 K diesel, and 1000 K biodiesel. The stoichiometric Z (Z_{st}), 0.054 for biodiesel and 0.046 for diesel, is drawn by the thick line. The computed images are composed from contour plots in one slice of an axisymmetric geometry which is then mirrored about the axis – hence the lines along the axis. Given that the Z_{st} of biodiesel is higher, it would be expected that the stoichiometric line to be more contracted and upstream. However, the reduced vaporisation rate of biodiesel fuel causes the Z of any axial location to be higher than the equivalent location in diesel fuel. In essence, shifting the higher Z region downstream. This has the effect of making the Z_{st} of both fuels about equal distance from the injector.

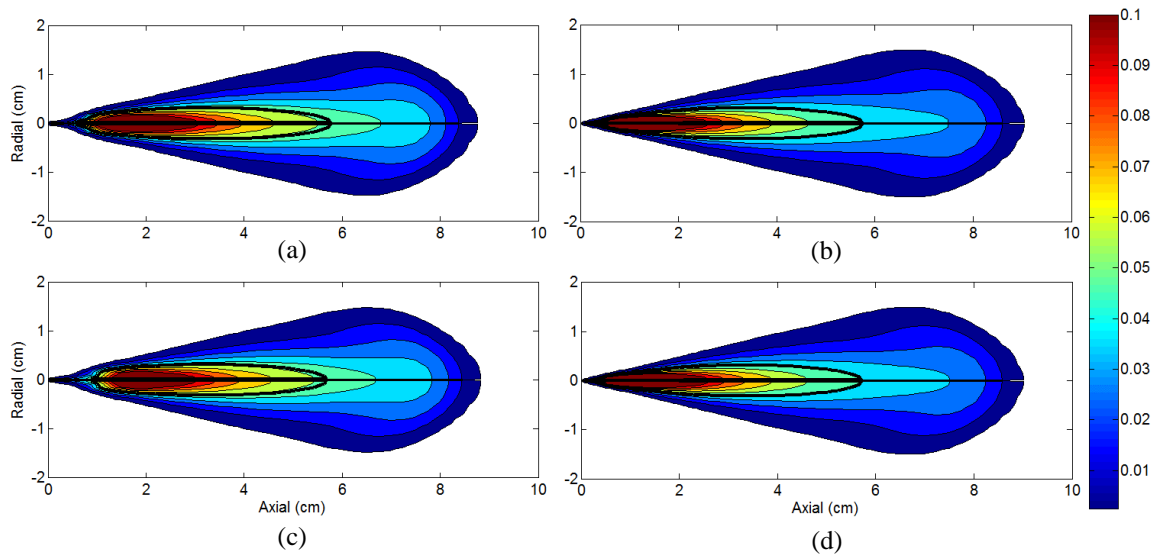


Figure 9.3: Mixture fraction contour plots of the computed non-reacting jets. Ambient temperature of 900 K is plotted above (a,b) and 1000 K below (c,d). Biodiesel cases left, diesel cases right. Stoichiometric mixture fraction is emphasised by thick line. Contour ranges from 0.0025 – 0.1.

9.4 Reacting Jet

For the reacting sprays, the ambient O₂ mole fraction was set to 15 %, which is typical of an engine with exhaust gas recirculation (EGR). Figure 9.4 shows the temperature contour plots of the computed sprays. Cases with an ambient temperature of 900 K are shown above (Fig. 9.4(a,b)), and 1,000 K (Fig. 9.4(c,d)) below. Biodiesel sprays are shown on the left, and diesel on the right. As expected, the cases with 1,000 K ambient temperature reaches a higher peak flame temperature. The flame lift-off lengths (LoL) are: 2.2 cm (1,000 K diesel), 1.9 cm (1,000 K biodiesel), and 2.4 cm (both 900 K cases). These values are within 10% of the measured LoL from Nerva et al. (2012) and matches the observations of LoL between diesel and biodiesel (Kuti et al., 2010). Although there has been previous work relating the LoL to the soot in the domain (Yen and Abraham, 2014; Mukhopadhyay and Abraham, 2012), that study focused on diesel jets. As such, such a relation cannot be applied to this work.

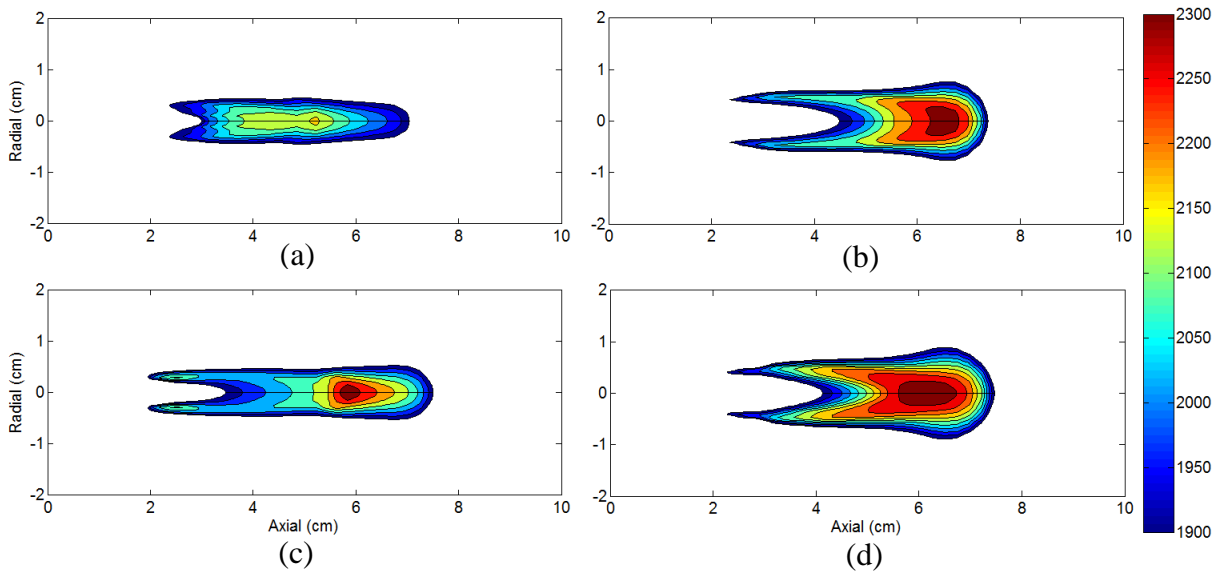


Figure 9.4: Temperature contour plots of the computed reacting jets. Ambient temperature of 900 K is plotted above (a,b) and 1000 K below (c,d). Biodiesel cases left, diesel cases right. Temperature ranges from 1,900 – 2,300 K.

Figure 9.5 shows the soot volume fraction (f_v) contours of the four cases. Similar to Fig. 9.4, the 900 K ambient temperature cases are above, and 1000 K cases below. Biodiesel case are on the left and diesel cases on the right. All four cases share the same contour levels. Though quantitative predictions of soot are difficult, qualitative comparisons can be made. It is apparent that the 1000 K diesel case produces the most soot, with a peak of around 7 ppm. It is interesting to note that even the 900 K diesel flame has higher soot than the 1000 K biodiesel case. At 900 K, the soot from the biodiesel case is negligible in the computations.

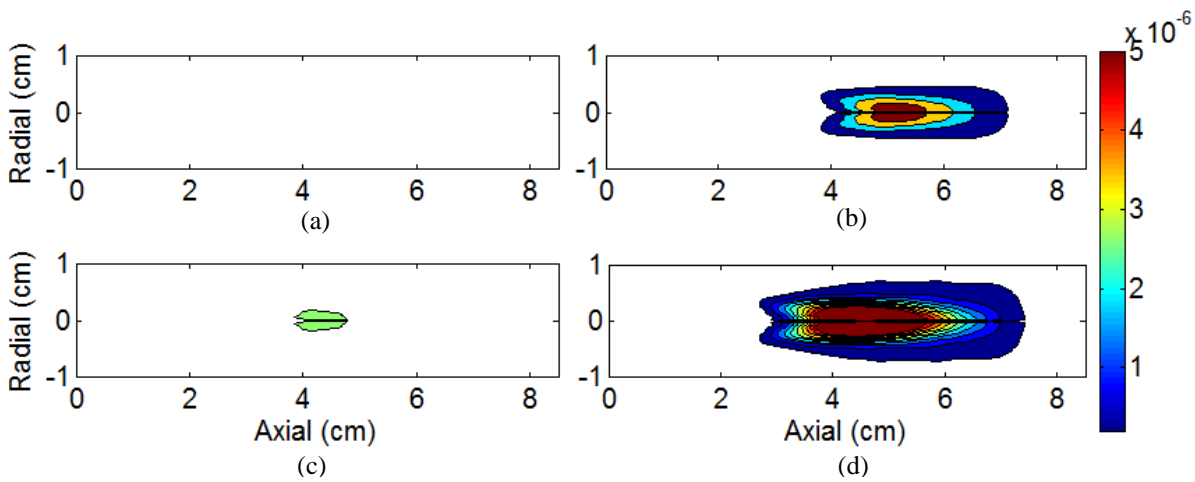


Figure 9.5: Soot volume fraction contour plots of the computed reacting jets. Ambient temperature of 900 K is plotted above (a,b) and 1000 K below (c,d). Biodiesel cases left, diesel cases right.

The soot f_v contours of the computed cases (a) are compared to measurements (b) in figure 9.6. As mentioned before, only qualitative comparisons can be made. In Fig. 9.6, the cases are compared in the order: 1000 K diesel, 1000 K biodiesel, 900 K diesel, 900 K biodiesel. The measured and computed flame lift-off lengths are identified on the figures. They are in

reasonable agreement, within about 10 %. When compared to the measured data, the computed soot f_v reaches a maximum value upstream of the location of the measured maximum value. The difference in axial distance is about 20 % for all cases. In fact, it appears that the entire soot curve is shifted upstream, with soot forming in a richer region and being oxidized much faster than evident in the measurements. Similar behaviour has been seen in a previous work which employed kinetic models to predict soot in diesel sprays (Yen and Abraham, 2014, 2015) and in turbulent jets (Cai et al., 2015; Kohler et al., 2012). One explanation for this behaviour is that the oxidation sub-model(s) reduces the soot too rapidly in leaner mixture fractions, thereby reducing the soot concentration downstream. Another explanation is that at 15 % ambient O_2 concentration, the reduction of O_2 oxidation is less than the reduction of soot formation due to lower flame temperatures. In spite of these limitations, the computations show lower soot volume fraction with biodiesel compared to diesel fuel and also show lower soot at 900 K relative to 1000 K. This is encouraging.

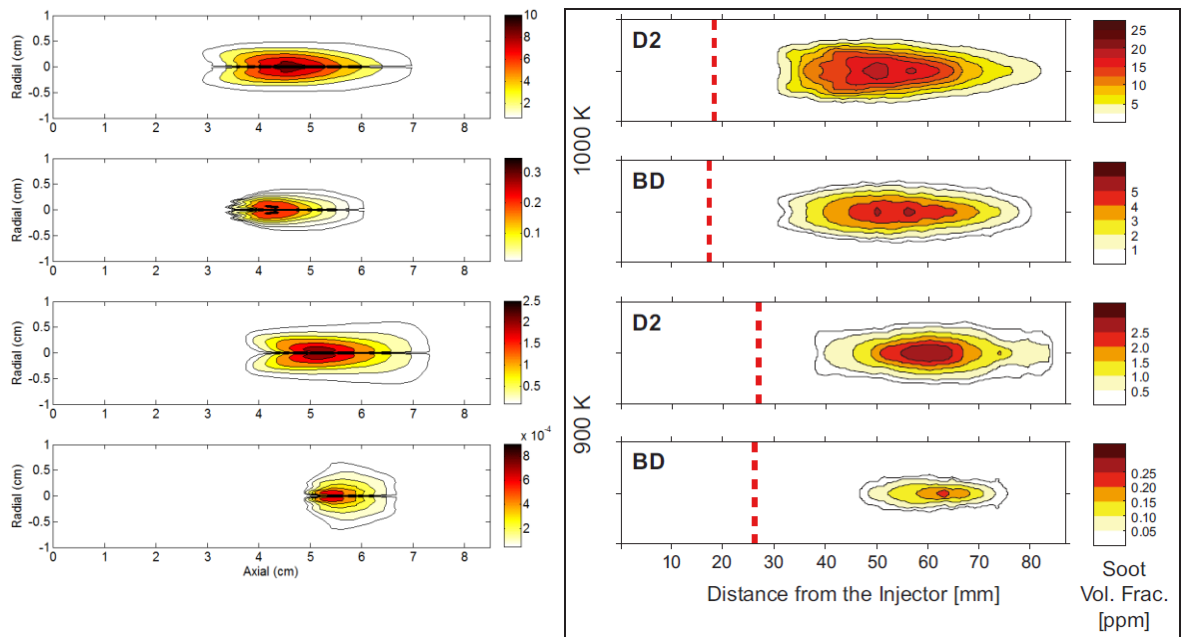


Figure 9.6: Predicted (a) soot volume fraction compared to measured data (b). Proceeding downwards, sprays are: 1000 K diesel, 1000 K biodiesel, 900 K diesel, 900 K biodiesel. Measured data taken from work of Nerva et al. (2012).

9.5 Summary and Conclusions

In this study computations of non-reacting and reacting biodiesel/diesel jets are conducted. For the non-reacting sprays, the liquid-phase penetration is in agreement of 30 %, and the vapour penetration within 10 %. A semi-empirical two-equation soot model is employed to compute soot in the reacting diesel and biodiesel sprays. The model was developed recently to predict soot in both diesel and biodiesel sprays. Computations are carried out for two chamber

temperatures that are typical of conditions in engines with exhaust gas recirculation. The flame lift-off heights are predicted well, within about 10 % of measured values. The soot model is able to predict the trends in reduction of soot in biodiesel sprays relative to diesel sprays and also the reduction in soot with decreasing chamber temperature.

10 Summary, Conclusions, and Future Work

This work has been directed toward a comparative study of biodiesel and petrodiesel combustion on a fundamental level. While it is clear from prior work that substituting petrodiesel with biodiesel has benefits in terms of energy security, toxic pollutant emissions, and carbon emissions on a life-cycle basis, such studies are often carried out experimentally in reciprocating compression-ignition engines where phasing of physical processes with transient volume change and wall effects potentially affect the results and conclusions. In fact, the challenges in interpreting engine results have made it difficult to isolate the importance of separate effects that can affect an outcome. Sometimes, there is no consensus on the outcome itself. For example, there is no consensus on whether NO_x emissions change when petrodiesel is substituted with biodiesel. While many studies suggest that NO_x emissions increase, others have found there to be no difference, and some have reported it to decrease. Explanations have varied from effects of injection timing to fuel effects. Hence, there is a need to do a comparative study of petrodiesel and biodiesel combustion at a fundamental level where the complexities of the engine do not influence the results. This is part of the objective of the current work. The next section will summarise the work and draw important conclusions. Section 10.2 will discuss possible future work.

10.1 Summary and Conclusions

Chapter 1 laid the motivation and objectives of the work, and focused on differences in properties between the two fuels and in their production methods. A literature review in Chapter 2 highlighted the need for comparative studies of petrodiesel and biodiesel combustion at a fundamental level, outside of the engine environment. The Chapter also reviewed existing understanding of diesel spray combustion and prior engine studies employing the two fuels. The review revealed some findings which appear to be widely accepted, e.g. particulate emissions from engines decrease when petrodiesel is substituted with biodiesel, whereas effects on efficiency are less clear.

In Chapter 3 the computational tools employed in this work were described. The studies are carried out by employing an in-house laminar flamelet code and a Reynolds-averaged Navier-Stokes (RANS) solver. Turbulence was modelled using the standard two-equation $k - \epsilon$ turbulence model. Turbulence-chemistry interactions were modelled using a tabulated unsteady flamelet progress variable model. NO was modelled using the comprehensive mechanism from GRI-Mech 3.0. Various soot models employed in this work were discussed throughout the thesis.

Chapter 4 reported on a study conducted as part of this work to investigate whether biodiesel spray behaviour is affected by feedstock selection. As is expected, the feedstock for biodiesel production differs based on the geographical region. Seven feedstocks from regions of major biodiesel production were chosen for comparison of their properties at two ambient temperatures. Fuel properties considered included density, vapour pressure, and surface tension. It was found that the liquid phase penetration distance differed noticeably based on the feedstock. This was, in turn, because of differences in the Sauter mean diameter (SMD) of the drops which induced differences in entrainment rate and also resulted in differences in vaporization rates. The vaporization rate is also influenced by the vapour pressure. It was shown that the differences in entrainment rate, vapour pressure, and finally SMD, in descending order of importance, affected the liquid phase penetration, although they are all interlinked. While liquid-phase penetrations varied between feedstocks, vapour-phase penetrations showed little change. As expected, the vapour-phase penetration is primarily injection momentum controlled. The mixture fraction distribution of the different sprays was also very similar. This implies that the biodiesel feedstock has no substantial effect on biodiesel combustion in engines under warm operating conditions where vaporization rate is relatively fast. Under cold start conditions, when the vaporization rate is slower and the liquid phase penetration dominates the spray length, the differences are likely to become more pronounced.

In Chapter 5, studies of combustion were conducted under the assumption that it occurs in flamelets around the spray. The laminar flamelet equations were solved using an in-house flamelet code. The specific focus of the study was on limit phenomena, i.e. ignition and extinction. Through the study, ignition and extinction scalar dissipation rates were determined for the two fuels. Though the magnitude of the ignition and extinction scalar dissipation rate limits tend to differ with the degree of complexity of the fuel surrogate kinetics mechanism, it was found that the limits for biodiesel were lower than for petrodiesel. It was also found that as the scalar dissipation rate increased, the rate of reduction of soot in biodiesel combustion was greater than in petrodiesel combustion. This implies that since scalar dissipation rate can be correlated with turbulent strain, soot formation in biodiesel combustion is more sensitive to changes in turbulent strain compared to petrodiesel combustion. In more practical terms, this suggests that increasing turbulent mixing in a biodiesel engine will have a greater impact on soot reduction than in a conventional petrodiesel engine. On the other hand, the rate of change of NO to changes of turbulent strain were similar for both petrodiesel and biodiesel combustion. NO formation is primarily temperature-dependant and it can be affected by turbulent strain only to the extent that the temperature is affected by turbulent strain.

In the next stage of the work, reported in Chapter 6, the soot formation pathways for both petrodiesel and biodiesel combustion were identified. A specific question of interest was: why is the soot formation rate in biodiesel combustion lower? The 115-species biodiesel surrogate mechanism (Luo et al., 2012) was extended by including species and reactions that were concurrently employed in both a detailed biodiesel surrogate mechanism (Herbinet et al., 2010) and a 160-species petrodiesel surrogate mechanism (Seiser et al., 2000). This resulted in a 214-species biodiesel surrogate mechanism and ensured that the differences in soot were not simply due to species and reactions missing from the original 115-species mechanism. Comparisons between the reaction pathways using this mechanism and the petrodiesel surrogate mechanism, showed that the differences in soot formation between biodiesel and petrodiesel combustion were on account of the concentration of aromatic species, such as pyrene, naphthalene, and benzene. Probing further into the formation of benzene, which is the initial aromatic species that is formed, through a reaction pathway analysis, helped in identifying a critical reaction pathway. In this pathway, the critical species at each level, through specific reactions, amplifies the difference in species mass fraction between petrodiesel and biodiesel at the next level. This results in the difference in benzene concentration between petrodiesel and biodiesel. It was also discovered that the pool of hydrocarbons that were candidates to form soot precursors was 50 % less in biodiesel than petrodiesel combustion.

A general understanding of soot formation suggests that a soot inception particle, formed from soot precursors, grows via surface growth and coagulation. It reduces in size through oxidation. This understanding is captured in semi-empirical soot models. The challenge is that existing semi-empirical soot models cannot be employed to predict soot in petrodiesel and biodiesel combustion with the same set of model constants. This is, in large part, because the soot inception species in existing models is not the appropriate one. Using the understanding gained in Chapter 6 on reaction pathways, a semi-empirical two-equation soot model was developed in Chapter 7 that can be employed in both petrodiesel and biodiesel combustion. From the reaction pathway analysis, the vinyl radical was chosen as the inception species as its ratio between the two fuels was similar to the ratio of soot between the two fuels. Surface growth was modelled through acetylene addition due to its mass fraction being similar in both fuels. When compared to a well-established soot kinetics model (Appel et al., 2000) in a one-dimensional flamelet study, the developed two-equation soot model can predict soot in both petrodiesel and biodiesel combustion reasonably well under typical engine conditions, at only a fraction of the computational cost of using the kinetics model.

Detailed extensive measurements of soot are not available in reacting biodiesel sprays. Hence, it is difficult to assess the accuracy of the soot model using experimental data in

biodiesel sprays. In Chapter 8, the semi-empirical two-equation soot model was validated using measured results in diesel sprays. Nine cases of experimental data were chosen from the Sandia National Laboratories' Engine Combustion Network (www.sandia.gov/ecn/) to validate the two-equation soot model. The nine cases have been well studied (Bajaj et al., 2013; Yen and Abraham, 2014, 2015). A 44-species n-heptane petrodiesel surrogate mechanism was chosen to represent fuel oxidation (Liu et al., 2003). The two equation soot model predicted relationship between flame lift-off length and soot well. When compared to some experimental data (due to lack of data on some cases), results from a kinetics-based soot model (Appel et al., 2010), and results from another accepted two-equation soot model (Leung et al., 1991), the new two equation soot model predicted the qualitative distribution of soot well.

In Chapter 9, the two-equation soot model was applied to predict soot in both diesel and biodiesel sprays. Similar to the previous study, a 44-species n-heptane mechanism was chosen to represent petrodiesel fuel oxidation (Liu et al., 2003). For biodiesel, a ternary-component biodiesel surrogate mechanism was chosen (Luo et al., 2012). Comparisons were made with measured data from the work of Nerva and co-workers (2012). Conditions represented those in diesel engines with exhaust gas re-circulation. Two ambient temperatures cases were considered: 900 and 1000 K. In terms of non-reacting liquid-phase penetration, the computational model predicted results within 10 % of the data for both temperatures. For vapour-phase penetration, the curve of both predicted and measured data collapsed onto an analytical curve. For the reacting jet, the predicted quantitative soot values follow the trends of the measured data. When compared to the measured data, the lift-off length is predicted within 10 %, and the soot distribution for both petrodiesel and biodiesel is predicted well. While further testing is needed, it appears that the two-equation soot model developed as part of the thesis work is able to model soot in both petrodiesel and biodiesel combustion.

10.2 Future Work

This work has shown that there is a need for further fundamental studies in biodiesel and petrodiesel combustion. Specific suggestions follow.

- 1.) While there are several studies in *laminar* hydrocarbon sooting flames using fuels that can be considered as diesel surrogates, there are very few such studies using biodiesel surrogates (Singh et al., 2012). This limits the ability to compare models through fundamental studies where turbulence-chemistry interactions are not important. Such studies can be focused on the chemical kinetics and soot formation and oxidation

mechanisms alone. In fact, such studies have driven the development of soot models for hydrocarbon flames in the last thirty years, but corresponding studies in biodiesel combustion are missing.

- 2.) An important finding in this computational study was that changes in turbulent strain have greater impact on soot formation and oxidation in biodiesel combustion compared to hydrocarbon combustion. Experimental evidence does not exist. An examination of engine data shows that it is hard to extract such evidence from engine data which is affected by many factors in addition to increasing mixing, for example, when engine speed is increased. Fundamental studies in counter-flow diffusion flames using surrogate fuels would be helpful in clarifying the impact of strain.
- 3.) Kinetic models for oxidation of biodiesel fuel surrogates are in an early stage of development. From the literature review, it can be seen that, unlike petrodiesel, where n-heptane and dodecane are well-accepted surrogate fuels, no consensus exists as to what the best surrogate fuels for biodiesel are. Recall that in the study where biodiesel feedstocks were compared, only the non-reacting sprays could be analysed. While it is known from engine studies that the feedstocks can influence combustion and formation of pollutants, these effects cannot be studied because oxidation mechanisms do not exist for the fuels from different feedstocks. One approach may be to develop oxidation mechanisms for the fundamental constituents of biodiesel fuels and then develop additive or mixing rules for developing the kinetics of the mixture of constituents. In fact, developing such mechanisms is a major effort in the case of gasoline, diesel, and jet fuels.
- 4.) The predictions of soot in the turbulent jet flames reveal that predicted soot generally lies upstream of the measured soot (Yen and Abraham, 2014, 2015; Kohler et al., 2012). Fundamental studies are under way to identify the reasons for this. In any case, the predicted behaviour implies that either soot formation rate reaches a maximum value upstream (rich), or that oxidation rate, be it via O₂ or OH, is higher than it should be. Existing oxidation sub-models have to be re-examined through fundamental studies.

References

- Abián, M., Peribáñez, E., Millera, Á., Bilbao, R. and Alzueta, M.U., 2014. Impact of nitrogen oxides (NO, NO₂, N₂O) on the formation of soot. *Combustion and Flame*, 161(1), pp.280-287.
- Abraham, J. and Pickett, L.M., 2010. Computed and measured fuel vapor distribution in a diesel spray. *Atomization and Sprays*, 20(3).
- Abraham, J., 2013. Recent progress in modeling reacting diesel sprays. In: *Australian Combustion Symposium (4th: 2013: Perth, Western Australia)*.
- Agarwal, A. and Assanis, D.N., 1997. Modeling the effect of natural gas composition on ignition delay under compression ignition conditions (No. 971711). SAE Technical Paper.
- Anand, K., Sharma, R.P. and Mehta, P.S., 2011. Experimental investigations on combustion, performance and emissions characteristics of neat karanja biodiesel and its methanol blend in a diesel engine. *Biomass and bioenergy*, 35(1), pp.533-541.
- Anneken, D.J., Both, S., Christoph, R., Fieg, G., Steinberner, U., Westfechtel, A., 327 2011. Fatty Acids, in: Wiley-vch (Eds.), Ullmann's Encyclopedia of Industrial 328 Chemistry, seventh ed. Wiley-VCH Verlag GmbH, Germany, pp. 73-116.
- Antoine, C., 1888. Tensions des vapeurs; nouvelle relation entre les tensions et les températures. *Comptes Rendus des Séances de l'Académie des Sciences*, 107, pp.681-684.
- Appel, J., Bockhorn, H., and Frenklach, M. (2000). Kinetic modeling of soot formation with detailed chemistry and physics: laminar premixed flames of C₂ hydrocarbons. *Combustion and Flame*, 121(1-2), 122–136. doi:10.1016/S0010-2180(99)00135-2.
- Bagley, S.T., Gratz, L.D., Johnson, J.H. and McDonald, J.F., 1998. Effects of an oxidation catalytic converter and a biodiesel fuel on the chemical, mutagenic, and particle size characteristics of emissions from a diesel engine. *Environmental science and technology*, 32(9), pp.1183-1191.
- Bajaj, C., Abraham, J. and Pickett, L.M., 2011. Vaporization effects on transient diesel spray structure. *Atomization and Sprays*, 21(5).
- Bajaj, C., Ameen, M., and Abraham, J. (2013). Evaluation of an Unsteady Flamelet Progress Variable Model for Autoignition and Flame Lift-Off in Diesel Jets. *Combustion Science and Technology*, 185, 454–472. doi:10.1080/00102202.2012.726667.
- Battin-Leclerc, F., 2008. Detailed chemical kinetic models for the low-temperature combustion of hydrocarbons with application to gasoline and diesel fuel surrogates. *Progress in Energy and Combustion Science*, 34(4), pp.440-498.
- Beltrame, A., Porshnev, P., Merchan-Merchan, W., Saveliev, A., Fridman, A., Kennedy, L.A., Petrova, O., Zhdanok, S., Amouri, F. and Charon, O., 2001. Soot and NO formation in methane–oxygen enriched diffusion flames. *Combustion and flame*, 124(1), pp.295-310.
- Bockhorn, H. ed., 2013. Soot formation in combustion: mechanisms and models (Vol. 59). Springer Science and Business Media.

- Bolla, M., Wright, Y.M., Boulouchos, K., Borghesi, G. and Mastorakos, E., 2013. Soot formation modeling of n-heptane sprays under diesel engine conditions using the conditional moment closure approach. *Combustion Science and Technology*, 185(5), pp.766-793.
- Bowman, C.T., 1992, December. Control of combustion-generated nitrogen oxide emissions: technology driven by regulation. In Symposium (International) on Combustion (Vol. 24, No. 1, pp. 859-878). Elsevier.
- Brakora, J. and Reitz, R.D., 2013. *A comprehensive combustion model for biodiesel-fueled engine simulations* (No. 2013-01-1099). SAE Technical Paper.
- Brakora, J.L., Ra, Y., Reitz, R.D., McFarlane, J. and Daw, C.S., 2008. *Development and validation of a reduced reaction mechanism for biodiesel-fueled engine simulations* (No. 2008-01-1378). SAE Technical Paper.
- Cai, G. and Abraham, J., 2013. Reaction pathways to soot formation in petrodiesel and biodiesel combustion. In *Australian Combustion Symposium (4th: 2013: Perth, Western Australia)*.
- Cai G, Abraham J. On formulating a simplified soot model for diesel and biodiesel combustion. *Chem Engineering Sci* 2015; under review.
- Cai G, Yen M, Abraham J. Predictions of Soot in Reacting Diesel Sprays with semi-empirical and kinetic models. *Proc. IMechE Part D: J. Auto Eng* 2015; under review.
- Canakci, M., 2005. Performance and emissions characteristics of biodiesel from soybean oil. *Proceedings of the Institution of Mechanical Engineers, Part D: Journal of Automobile Engineering*, 219(7), pp.915-922.
- Cardone, M., Prati, M.V., Rocco, V., Seggiani, M., Senatore, A. and Vitolo, S., 2002. Brassica carinata as an alternative oil crop for the production of biodiesel in Italy: engine performance and regulated and unregulated exhaust emissions. *Environmental science and technology*, 36(21), pp.4656-4662.
- Castellanos Diaz, O., Schoeggl, F., Yarranton, H.W., Satyro, M.A., Lovestead, T.M., Bruno, T.J., 2012. Modeling the vapor pressure of biodiesel fuels. *World Academy of Science, Engineering and Technology*. 6, 839-849.
- Castro M.P.P., Andrade, A.A., Franco, R.W.A., Miranda, P.C.M.L., Stel, M., 276 Vargas, H., Constantino, R., Baesso, M.L., 2005. Thermal properties 277 measurements in biodiesel oils using photothermal techniques. *Chem. Phys.* 278 Letters. 411, 18-22.
- Chen, P., Wang, W., Roberts, W.L., Fang, T., 2013. Spray and atomization of diesel fuel and its alternatives from a single-hole injector using a common rail fuel injection system. *Fuel*, 103, 850-861.
- Chen, G., Yu, W., Fu, J., Mo, J., Huang, Z., Yang, J., Wang, Z., Jin, H. and Qi, F., 2012. Experimental and modeling study of the effects of adding oxygenated fuels to premixed n-heptane flames. *Combustion and Flame*, 159(7), pp.2324-2335.

Cheung W.W.L., Lam, V.W.Y., Sarmiento, J.L., Kearney, K., Watson, R., Zeller, D., Pauly, D., 2010. Large-scale redistribution of maximum fisheries catch potential in the global ocean under climate change. *Global Change Biology*, 16, 24-35.

Chevron, 1998. *Diesel Fuels Technical Review*. Chevron Products Company, USA.

Chevron, 2007. *Diesel Fuels Technical Review*. Chevron Products Company, USA.

Chew, K.J., 2014. The future of oil: unconventional fossil fuels. *Philosophical Transactions of the Royal Society of London A: Mathematical, Physical and Engineering Sciences*, 372(2006), p.20120324.

Ciezki, H.K. and Adomeit, G., 1993. Shock-tube investigation of self-ignition of n-heptane-air mixtures under engine relevant conditions. *Combustion and Flame*, 93(4), pp.421-433.

Curran, H.J., Gaffuri, P., Pitz, W.J. and Westbrook, C.K., 1998. A comprehensive modeling study of n-heptane oxidation. *Combustion and flame*, 114(1), pp.149-177.

Dec, J.E., 1997. *A conceptual model of diesel combustion based on laser-sheet imaging** (No. 970873). SAE technical paper.

Demirbas, A., 2002. Biodiesel from vegetable oils via transesterification in supercritical methanol. *Energy Conversion and Management*, 43(17), 2349-2356.

Demirbas, A., 2009. Progress and recent trends in biodiesel fuels. *Energy conversion and management*, 50(1), pp.14-34.

Dockery, D.W., Pope, C.A., Xu, X., Spengler, J.D., Ware, J.H., Fay, M.E., Ferris Jr, B.G. and Speizer, F.E., 1993. An association between air pollution and mortality in six US cities. *New England journal of medicine*, 329(24), pp.1753-1759.

Dukowicz, J. K. (1980). A particle-fluid numerical model for liquid sprays. *Journal of Computational Physics*, 35(2), 229–253. doi:10.1016/0021-9991(80)90087-x.

Elkoth, M.M., 1982. Fuel atomization for spray modelling. *Progress in Energy and Combustion Science*, 8(1), pp.61-91.

Encyclopedia of Earth, Effects of oil on wildlife and habitat, <http://www.eoearth.org/view/article/158446/>, last access 17th Dec 2015.

Faeth, G.M., 1983. Evaporation and combustion of sprays. *Progress in Energy and Combustion Science*, 9(1), pp.1-76.

Farrace, D., Bolla, M., Wright, Y.M. and Boulouchos, K., 2013. Predicting in-cylinder soot in a heavy-duty diesel engine for variations in SOI and TDC temperature using the Conditional Moment Closure model (No. 2013-24-0016). SAE Technical Paper.

Feng, Q., Jalali, A., Fincham, A.M., Wang, Y.L., Tsotsis, T.T. and Egolfopoulos, F.N., 2012. Soot formation in flames of model biodiesel fuels. *Combustion and Flame*, 159(5), pp.1876-1893.

- Fenimore, C.P. and Jones, G.W., 1967. Oxidation of soot by hydroxyl radicals. *The Journal of Physical Chemistry*, 71(3), pp.593-597.
- Fenimore, C.P., 1971, December. Formation of nitric oxide in premixed hydrocarbon flames. In *Symposium (International) on Combustion* (Vol. 13, No. 1, pp. 373-380). Elsevier.
- Frenklach, M., Clary, D.W., Gardiner, W.C. and Stein, S.E., 1988, December. Effect of fuel structure on pathways to soot. In *Symposium (International) on Combustion* (Vol. 21, No. 1, pp. 1067-1076). Elsevier.
- Fisher, E.M., Pitz, W.J., Curran, H.J., Westbrook, C.K., 2000. Detailed chemical kinetic mechanisms for combustion of oxygenated fuels. *Proceedings of the combustion institute*, 28(2), pp.1579-1586.
- Frenklach, M., 2002. Reaction mechanism of soot formation in flames. *Physical Chemistry Chemical Physics*, 4(11), pp.2028-2037.
- Frenklach, M., Harris, S.J., 1986. Aerosol dynamics modeling using the method of moments. *J. Colloid and Interface Sci.* 118(1), 252-261.
- Frenklach, M. and Wang, H., 1991, December. Detailed modeling of soot particle nucleation and growth. In *Symposium (International) on Combustion* (Vol. 23, No. 1, pp. 1559-1566). Elsevier.
- Frenklach, M. and Wang, H., 1994. Detailed mechanism and modeling of soot particle formation. In *Soot formation in combustion* (pp. 165-192). Springer Berlin Heidelberg.
- Frenklach, M. and Warnatz, J., 1987. Detailed modeling of PAH profiles in a sooting low-pressure acetylene flame. *Combustion science and technology*, 51(4-6), pp.265-283.
- Frijters, P.J.M. and Baert, R.S.G., 2006. Oxygenated fuels for clean heavy-duty diesel engines. *International journal of vehicle design*, 41(1-4), pp.242-255.
- Garo, A., Prado, G. and Lahaye, J., 1990. Chemical aspects of soot particles oxidation in a laminar methane-air diffusion flame. *Combustion and Flame*, 79(3), pp.226-233.
- Genzale, C.L., Pickett, L.M., Kook, S., 2010. Liquid penetration of diesel and biodiesel sprays at late-cycle post-injection conditions. *SAE Technical Paper*, 2010-01-0610.
- Giakoumis, E.G., 2013. A statistical investigation of biodiesel physical and chemical properties, and their correlation with the degree of unsaturation. *Renewable Energy*, 50, pp.858-878.
- Gilyazetdinov L.P., 1972. *Khim Tverd Topl*;3:103.
- Glaude, P., Fournet, R., Bounaceur, R., Moliere, M., 2010. Adiabatic flame temperature from biofuels and fossil fuels and derived effect on NOx emissions. *Fuel Processing Technol.* 91, 229-235.
- Glaude, P.A., Herbinet, O., Bax, S., Biet, J., Warth, V. and Battin-Leclerc, F., 2010. Modeling of the oxidation of methyl esters—Validation for methyl hexanoate, methyl heptanoate, and methyl decanoate in a jet-stirred reactor. *Combustion and flame*, 157(11), pp.2035-2050.

- Goering, C.E., Schwab, A.W., Daugherty, M.J., Pryde, E.H., Heakin, A.J., 1982. Fuel properties of eleven oils. *Trans. ASAE*, 25, 1472-1483.
- Gogoi, T.K. and Baruah, D.C., 2010. A cycle simulation model for predicting the performance of a diesel engine fuelled by diesel and biodiesel blends. *Energy*, 35(3), pp.1317-1323.
- Golovitchev, V.I. and Yang, J., 2009. Construction of combustion models for rapeseed methyl ester bio-diesel fuel for internal combustion engine applications. *Biotechnology advances*, 27(5), pp.641-655.
- Gopalakrishnan, V. and Abraham, J., 2004. Effects of multicomponent diffusion on predicted ignition characteristics of an n-heptane diffusion flame. *Combustion and Flame*, 136(4), pp.557-566.
- Gopalakrishnan, V. and Abraham, J., 2004. Computed NO and soot distribution in turbulent transient jets under diesel conditions. *Combustion science and technology*, 176(4), pp.603-641.
- Graboski, M.S. and McCormick, R.L., 1998. Combustion of fat and vegetable oil derived fuels in diesel engines. *Progress in energy and combustion science*, 24(2), pp.125-164.
- Haynes, B.S. and Wagner, H.G., 1981. Soot formation. *Progress in Energy and Combustion Science*, 7(4), pp.229-273.
- Herbnet, O., Pitz, W.J. and Westbrook, C.K., 2008. Detailed chemical kinetic oxidation mechanism for a biodiesel surrogate. *Combustion and Flame*, 154(3), pp.507-528.
- Herbnet, O., Pitz, W.J. and Westbrook, C.K., 2010. Detailed chemical kinetic mechanism for the oxidation of biodiesel fuels blend surrogate. *Combustion and Flame*, 157(5), pp.893-908.
- Herzler, J., Jerig, L. and Roth, P., 2005. Shock tube study of the ignition of lean n-heptane/air mixtures at intermediate temperatures and high pressures. *Proceedings of the Combustion Institute*, 30(1), pp.1147-1153.
- Hess, M.A., Haas, M.J., Foglia, T.A. and Marmer, W.N., 2005. Effect of antioxidant addition on NO_x emissions from biodiesel. *Energy and Fuels*, 19(4), pp.1749-1754.
- Heywood, J.B., *Internal Combustion Engine Fundamentals*, McGraw-Hill New York, US, 1988.
- Hinze, J.O., 1975. *Turbulence* McGraw-Hill. New York, 218.
- Hiroyasu, H. and Kadota, T., 1976. Models for combustion and formation of nitric oxide and soot in direct injection diesel engines (No. 760129). SAE Technical Paper.
- Hirsch, R.L., Peaking of world oil production. In: Atlantic Council Workshop on Transatlantic Energy Issues, 23rd October, 2006.
- Hoffman, S.R., Abraham, J., 2009. A comparative study of n-heptane, methyl decanoate, and dimethyl ether combustion characteristics under homogeneous-charge compression-ignition engine conditions. *Fuel*, 88(6), 1099-1108.

- Hong, S., Wooldridge, M.S., Im, H.G., Assanis, D.N. and Pitsch, H., 2005. Development and application of a comprehensive soot model for 3D CFD reacting flow studies in a diesel engine. *Combustion and Flame*, 143(1), pp.11-26.
- Hou, Z.X. and Abraham, J., 1995. *Three-dimensional modeling of soot and NO in a direct-injection diesel engine* (No. 950608). SAE Technical Paper.
- Ihme, M., and See, Y.C., 2009. Large-Eddy Simulation of a Turbulent Lifted Flame in a Vitiated Co-Flow. *AIAA Aerospace Sciences Meeting Exhibition*.
- Ihme, M. and See, Y.C., 2010. Prediction of autoignition in a lifted methane/air flame using an unsteady flamelet/progress variable model. *Combustion and Flame*, 157(10), pp.1850-1862.
- International Energy Agency, Oil, <http://www.iea.org/aboutus/faqs/oil/>, last access 17th Dec 2015.
- Iyer, V.A., Post, S.L., Abraham, J., 2000. Is the liquid penetration in diesel sprays mixing controlled? *Proc. Combust. Inst.* 28, 1111-1118.
- Jones, W.P. and Whitelaw, J.H., 1982. Calculation methods for reacting turbulent flows: a review. *Combustion and flame*, 48, pp.1-26.
- Kazakov, A. and Foster, D.E., 1998. *Modeling of soot formation during DI diesel combustion using a multi-step phenomenological model* (No. 982463). SAE Technical Paper.
- Kazakov, A. and Frenklach, M., 1998. Dynamic modeling of soot particle coagulation and aggregation: Implementation with the method of moments and application to high-pressure laminar premixed flames. *Combustion and Flame*, 114(3), pp.484-501.
- Kazakov, A., Wang, H. and Frenklach, M., 1995. Detailed modeling of soot formation in laminar premixed ethylene flames at a pressure of 10 bar. *Combustion and Flame*, 100(1), pp.111-120.
- Kegl, B., 2008. Effects of biodiesel on emissions of a bus diesel engine. *Bioresource technology*, 99(4), pp.863-873.
- Kennedy, I.M., 1997. Models of soot formation and oxidation. *Progress in Energy and Combustion Science*, 23(2):95-132.
- Kitamura, T., Ito, T., Senda, J., Fujimoto, H., 2001. *Detailed chemical kinetic modeling of diesel spray combustion with oxygenated fuels* (No. 2001-01-1262). SAE Technical Paper.
- Kitamura, T., Ito, T., Senda, J., Fujimoto, H., 2002. Mechanism of smokeless diesel combustion with oxygenated fuels based on the dependence of the equivalence ration and temperature on soot particle formation. *International Journal of Engine Research*, 3(4), pp.223-248.
- Kittelson D.B., 1998. Engines and nanoparticles: a review. *J Aero Sci*, 29:575-588. doi:10.1016/S0021-8502(97)10037-4.
- Khan, I.M., Wang, C.H.T. and Langridge, B.E., 1971. Coagulation and combustion of soot particles in diesel engines. *Combustion and Flame*, 17(3), pp.409-419.

- Knothe, G., 2006. Analyzing biodiesel: standards and other methods. *Journal of the American Oil Chemists' Society*, 83(10), pp.823-833.
- Köhler, M., Geigle, K.P., Blacha, T., Gerlinger, P. and Meier, W., 2012. Experimental characterization and numerical simulation of a sooting lifted turbulent jet diffusion flame. *Combustion and Flame*, 159(8), pp.2620-2635.
- Kong, S.C., Sun, Y. and Rietz, R.D., 2007. Modeling diesel spray flame liftoff, sooting tendency, and NO_x emissions using detailed chemistry with phenomenological soot model. *Journal of Engineering for Gas Turbines and Power*, 129(1), pp.245-251.
- Kouremenos, D.A., Rakopoulos, C.D. and Hountalas, D., 1990. Thermodynamic analysis of indirect injection diesel engines by two-zone modeling of combustion. *Journal of engineering for gas turbines and power*, 112(1), pp.138-149.
- Krahl, J., Munack, A., Schröder, O., Stein, H. and Bünger, J., 2003. Influence of biodiesel and different designed diesel fuels on the exhaust gas emissions and health effects (No. 2003-01-3199). SAE Technical Paper.
- Kuti, O.A., Xiangang, W.G., Zhang, W., Nishida, K., Huang, Z.H., 2010. Characteristics of the ignition and combustion of biodiesel fuel spray injected by a common-rail injection system for a direct-injection diesel engine. *Proceedings of the Institution of Mechanical Engineers, Part D: Journal of Automobile Engineering*, 224(12), pp.1581-1596.
- Lai, J.Y., Lin, K.C. and Violi, A., 2011. Biodiesel combustion: advances in chemical kinetic modeling. *Progress in Energy and Combustion Science*, 37(1), pp.1-14.
- Lapuerta, M., Armas, O. and Rodriguez-Fernandez, J., 2008. Effect of biodiesel fuels on diesel engine emissions. *Progress in energy and combustion science*, 34(2), pp.198-223.
- Lapuerta, M., Rodriguez-Fernandez, J., Oliva, F., 2010. Determination of enthalpy of formation of methyl and ethyl esters of fatty acids. *Chem. Phys. of Lipids*. 163, 172-181.
- Lauder, B.E., and Spalding, D.B., 1974. The numerical computation of turbulent flows. *Computer Methods in Applied Mechanics and Engineering*, 3(2), 269-289.
- Lee, Y., Huh, K.Y., 2013. Numerical study on spray and combustion characteristics of diesel and soy-based biodiesel in a CI engine. *Fuel*, 113, pp.537-545.
- Lee, K.B., Thring, M.W. and Beer, J.M., 1962. On the rate of combustion of soot in a laminar soot flame. *Combustion and Flame*, 6, pp.137-145.
- Leung, K.M., Lindstedt, R.P. and Jones, W.P., 1991. A simplified reaction mechanism for soot formation in nonpremixed flames. *Combustion and flame*, 87(3), pp.289-305.
- Li, Y.H. and Kong, S.C., 2008. Diesel combustion modelling using LES turbulence model with detailed chemistry. *Combustion theory and modelling*, 12(2), pp.205-219.
- Liu, F., Guo, H., Smallwood, G.J. and Gülder, Ö.L., 2003. Numerical modelling of soot formation and oxidation in laminar coflow non-smoking and smoking ethylene diffusion flames. *Combustion Theory and Modelling*, 7(2), 301-315.

- Lindstedt, R.P. and Skevis, G., 1994. Detailed kinetic modeling of premixed benzene flames. *Combustion and Flame*, 99(3), pp.551-561.
- Lindstedt, R.P. and Skevis, G., 1997. Chemistry of acetylene flames. *Combustion Science and Technology*, 125(1-6), pp.73-137.
- Liu, S., Hewson, J.C., Chen, J.H. and Pitsch, H., 2004. Effects of strain rate on high-pressure nonpremixed n-heptane autoignition in counterflow. *Combustion and flame*, 137(3), pp.320-339.
- Luo, Z., Plomer, M., Lu, T., Som, S., Longman, D.E., Sarathy, S.M. and Pitz, W.J., 2012. A reduced mechanism for biodiesel surrogates for compression ignition engine applications. *Fuel*, 99, pp.143-153.
- Ma, F. and Hanna, M.A., 1999. Biodiesel production: a review. *Bioresource technology*, 70(1), pp.1-15.
- Machacon, H.T.C., Shiga, S., Karasawa, T., and Nakamura, H. 2001b. Performance and emission characteristics of a diesel engine fueled with coconut oil-diesel fuel blend. *Biomass and Bioenergy* 20:63–69.
- Magi, V., 1987. REC-87: a new 3-D code for flows, sprays and combustion in reciprocating and rotary Engines. *Department of Mechanical and Aerospace Engineering, Princeton University, Princeton, NJ*.
- Magi, V., and Abraham, J., 2001. The k- ϵ Model and Computed Spreading Rates in Round and Plane Jets. *Numerical Heat Transfer, Part A: Applications*, 40(4), 317–334. doi:10.1080/104077801753238130.
- Majewski, W.A., Khair, M.K., 2006. Diesel Emissions and Their Control, SAE Int. Warrendale, PA.
- Mancaruso, E., Sequino, L., Vaglieco, B.M., 2011. First and second generation biodiesels spray characterization in a diesel engine. *Fuel*. 90, 2870-2883.
- McCormick, R.L., Alvarez, J.R. and Graboski, M.S., 2003. NO_x solutions for biodiesel. *NREL Final Report, SR-510-31465*.
- Mehta, P.S. and Das, S., 1992. A correlation for soot concentration in diesel exhaust based on fuel-air mixing parameters. *Fuel*, 71(6), pp.689-692.
- Minetti, R., Carlier, M., Ribaucour, M., Therssen, E. and Sochet, L.R., 1995. A rapid compression machine investigation of oxidation and auto-ignition of n-heptane: measurements and modeling. *Combustion and Flame*, 102(3), pp.298-309.
- Ministry of Infrastructure and the Environment, Climate change: how does the Netherlands take action? <http://climateagenda.minienv.nl/>, last access 16th Dec 2015.
- Moss, J.B., Stewart, C.D. and Young, K.J., 1995. Modeling soot formation and burnout in a high temperature laminar diffusion flame burning under oxygen-enriched conditions. *Combustion and Flame*, 101(4), pp.491-500.

Mueller, C.J., Boehman, A.L., Martin, G.C., 2009. An experimental investigation of the origin of increased nox emissions when fueling a heavy-duty compression-ignition engine with soy biodiesel. *SAE Technical Paper*, 2009-01-1792.

Mukhopadhyay, S., 2011. Ignition and early flame development in stratified-charge mixtures. PhD Thesis, Purdue University.

Mukhopadhyay, S. and Abraham, J., 2012. Evaluation of an unsteady flamelet progress variable model for autoignition and flame development in compositionally stratified mixtures. *Physics of Fluids*, 24(7),75-115.

Murphy, M.J., Taylor, J.D. and McCormick, R.L., 2004. *Compendium of experimental cetane number data* (pp. 1-48). Golden, CO: National Renewable Energy Laboratory.

Nagle, J. and Strickland-Constable, R.F., 1962. Oxidation of Carbon between 1000-2000 C. In *Proceedings of the fifth carbon conference* (Vol. 1, No. 1, p. 154). New York: Pergamon.

Nerva, J., Genzale, C.L., Kook, S., Garcia-Oliver, J.M., Pickett, L.M., 2012. Fundamental spray and combustion measurements of soy methyl-ester biodiesel. *Int. J. Engine Research*. 14, 373-390.

NIST Chemistry Webbook, webbook.nist.gov/chemistry/, last access 20th Nov 2015.

Ng, J.H., Ng, H.K. and Gan, S., 2012. Characterisation of engine-out responses from a light-duty diesel engine fuelled with palm methyl ester (PME). *Applied Energy*, 90(1), pp.58-67.

O'Rourke, P. J. (1981). *Collective Drop Effects on Vaporizing Liquid Sprays*. Princeton University.

O'Rourke, P., and Bracco, F. (1980). Modelling of drop interactions in thick sprays and a comparison with experiments. *Proceedings of the Institution of Mechanical Engineers*.

Odeh, I.O., Tan, D.K. and Ancev, T., 2011. Potential suitability and viability of selected biodiesel crops in Australian marginal agricultural lands under current and future climates. *Bioenergy Research*, 4(3), pp.165-179.

Pacala, S., Socolow, R., 2004. Stabilization wedges: solving the climate problem for the next 50 years with current technologies. *Science*, 304(5686), 968-972.

Peng, C., Yang, H., Lan, C., Chien, S., 2007. Effects of the biodiesel blend fuel on aldehyde emissions from diesel engine exhaust. *Atmospheric Environment*, 42(5), 906-915.

Peters, N. (1984). Laminar diffusion flamelet models in non-premixed turbulent combustion. *Progress in Energy and Combustion Science*, 10(3), 319-339. doi:10.1016/0360-1285(84)90114-X.

Peters, N. (1986). Laminar flamelet concepts in turbulent combustion. In: *Twenty-First Symposium (International) on Combustion*, The Combustion Institute, 1231-1250.

- Peters, N., Paczko, G., Seiser, R. and Seshadri, K., 2002. Temperature cross-over and non-thermal runaway at two-stage ignition of n-heptane. *Combustion and Flame*, 128(1), pp.38-59.
- Pickett, L.M., Siebers, D.L. and Idicheria, C.A., 2005. *Relationship between ignition processes and the lift-off length of diesel fuel jets* (No. 2005-01-3843). SAE technical paper.
- Pitz, W.J. and Mueller, C.J., 2011. Recent progress in the development of diesel surrogate fuels. *Progress in Energy and Combustion Science*, 37(3), pp.330-350.
- Raheman, H. and Phadatare, A.G., 2004. Diesel engine emissions and performance from blends of karanja methyl ester and diesel. *Biomass and Bioenergy*, 27(4), pp.393-397.
- Reaction Design, 2010. Chemkin-Pro 15101. *Reaction Design, San Diego, CA*.
- Richter, H. and Howard, J.B., 2000. Formation of polycyclic aromatic hydrocarbons and their growth to soot—a review of chemical reaction pathways. *Progress in Energy and Combustion science*, 26(4), pp.565-608.
- Sales-Cruz, M., Aca-Aca, G., Sanchez-Daza, O., Lopez-Arenas, T., 2010. Predicting critical properties, densities and viscosity of fatty acids, triacylglycerols and methyl esters by group contribution methods. In: 20th European Symposium on Computer Aided Process Engineering, Naples, Italy.
- Sarathy, S.M., Thomson, M.J., Pitz, W.J. and Lu, T., 2011. An experimental and kinetic modeling study of methyl decanoate combustion. *Proceedings of the Combustion Institute*, 33(1), pp.399-405.
- Scheepers, P.T., Vermeulen, R.C., 2012. Diesel engine exhaust classified as a human lung carcinogen. How will this affect occupational exposures? *Occupational and environmental medicine*, 69, 691-693.
- Schlichting, H., Gersten, K. and Gersten, K., 2000. *Boundary-layer theory*. Springer Science and Business Media.
- Seiser, R., Pitsch, H., Seshadri, K., Pitz, W.J. and Gurrán, H.J., 2000. Extinction and autoignition of n-heptane in counterflow configuration. *Proceedings of the Combustion Institute*, 28(2), pp.2029-2037.
- Senosiain, J.P. and Miller, J.A., 2007. The Reaction of n- and i-C₄H₅ Radicals with Acetylene. *The Journal of Physical Chemistry A*, 111(19), pp.3740-3747.
- Seshadri, K., Lu, T., Herbinet, O., Humer, S., Niemann, U., Pitz, W.J., Seiser, R. and Law, C.K., 2009. Experimental and kinetic modeling study of extinction and ignition of methyl decanoate in laminar non-premixed flows. *Proceedings of the Combustion Institute*, 32(1), pp.1067-1074.
- Sharp, C.A., Howell, S.A. and Jobe, J., 2000a. *The effect of biodiesel fuels on transient emissions from modern diesel engines, part I regulated emissions and performance* (No. 2000-01-1967). SAE Technical Paper.

- Sharp, C.A., Howell, S.A. and Jobe, J., 2000b. *The effect of biodiesel fuels on transient emissions from modern diesel engines, part II unregulated emissions and chemical characterization* (No. 2000-01-1968). SAE Technical Paper.
- Sheehan, J., Camobreco, V., Duffield, J., Shapouri, H., Graboski, M. and Tyson, K.S., 2000. *An overview of biodiesel and petroleum diesel life cycles*(No. NREL/TP-580-24772). National Renewable Energy Lab., Golden, CO (US).
- Shen, H.P.S., Steinberg, J., Vanderover, J. and Oehlschlaeger, M.A., 2009. A shock tube study of the ignition of n-heptane, n-decane, n-dodecane, and n-tetradecane at elevated pressures. *Energy and Fuels*, 23(5), pp.2482-2489.
- Shukla, B., Koshi, M., 2012. A novel route for PAH growth in HACA based mechanisms. *Combustion and Flame*, 159(12), pp.3589-3596.
- Siebers, D.L. and Higgins, B., 2001. *Flame lift-off on direct-injection diesel sprays under quiescent conditions* (No. 2001-01-0530). SAE Technical Paper.
- Siebers, D.L., 1998. *Liquid-phase fuel penetration in diesel sprays* (No. 980809). SAE technical paper.
- Siebers, D.L., Higgins, B. and Pickett, L., 2002. *Flame lift-off on direct-injection diesel fuel jets: oxygen concentration effects* (No. 2002-01-0890). SAE Technical Paper.
- Siegmann, K., Scherrer, L. and Siegmann, H.C., 1998. Physical and chemical properties of airborne nanoscale particles and how to measure the impact on human health. *Journal of Molecular Structure: THEOCHEM*,458(1), pp.191-201.
- Singh, V.N., Parthasarathy, R.N., Gollahalli, S.R. and Aldana, C., 2013. Radiation and Emission Characteristics of Laminar Partially-Premixed Flames of Petroleum Diesel-Canola Methyl Ester Blends. *Journal of Petroleum Science Research*.
- Smith, G.P., Golden, D.M., Frenklach, M., Moriarty, N.W., Eiteneer, B., Goldenberg, M., Bowman, C.T., Hanson, R.K., Song, S., Gardiner Jr, W.C. and Lissianski, V.V., 1999. GRI-Mech 3.0.
- Som, S. and Longman, D.E., 2011. Numerical study comparing the combustion and emission characteristics of biodiesel to petrodiesel. *Energy and Fuels*, 25(4), pp.1373-1386.
- Som, S., Longman, D.E., Ramirez, A.I., Aggarwal, S.K., 2010. A comparison in injector flow and spray characteristics of biodiesel with petrodiesel. *Fuel*. 89, 4014-4024.
- Song, J., Alam, M., Boehman, A.L. and Kim, U., 2006. Examination of the oxidation behavior of biodiesel soot. *Combustion and flame*, 146(4), pp.589-604.
- Speizer, F.E., Ferris, B. Jr., Bishop, Y.M., Spengler, J., 1980. Respiratory disease rates and pulmonary function in children associated with NO₂ exposure. *The American review of respiratory disease*, 121, 3-10.
- Stanmore, B.R., Brillhac, J.F. and Gilot, P., 2001. The oxidation of soot: a review of experiments, mechanisms and models. *Carbon*, 39(15), pp.2247-2268.

- Sukumaran, S., Van Huynh, C. and Kong, S.C., 2013. Numerical modeling of soot emissions in diesel sprays based on detailed fuel and PAH chemistry. *Combustion Science and Technology*, 185(11), pp.1696-1714.
- Sun, J., Caton, J.A., Jacobs, T.J., 2010. Oxides of nitrogen emissions from biodiesel-fuelled diesel engines. *Prog. Energy Combust. Sci.*, 36, 677-695.
- Szybist, J.P., McFarlane, J. and Bunting, B.G., 2007. Comparison of simulated and experimental combustion of biodiesel blends in a single cylinder diesel HCCI engine (No. 2007-01-4010). SAE Technical Paper.
- Tao, F., Reitz, R.D., Foster, D.E. and Liu, Y., 2009. Nine-step phenomenological diesel soot model validated over a wide range of engine conditions. *International Journal of Thermal Sciences*, 48(6), pp.1223-1234.
- Tesner, P.A. and Tsibulevsky, A.M., 1967. Kinetics of dispersed carbon gasification in diffusion flames of hydrocarbons. *Combustion and Flame*, 11(3), pp.227-233.
- Tornqvist, H., Mills, N.L., Gonzalez, M., Miller, M.R., Robinson, S.D., Megson, I.L., MacNee, W., Donaldson, K., Soderberg, S., Newby, D.E., Sandstrom, T., Blomberg, A., 2007. Persistent endothelial dysfunction in humans after diesel exhaust inhalation. *Am J Resp Crit Care Med*;176:395-400. doi:10.1164/rccm.200606-872OC.
- Turns, S.R., 1996. *An introduction to combustion*. New York: McGraw-hill.
- U.S. Energy Information Administration, 2013. North America leads the world in production of shale gas, <http://www.eia.gov/todayinenergy/detail.cfm?id=13491>, last access 21st Dec 2015.
- U.S. Energy Information Administration, 2014. U.S. natural gas production by source, http://www.eia.gov/energy_in_brief/article/shale_in_the_united_states.cfm, last access 21st Dec 2015.
- U.S. Energy Information Administration, 2015. Total Biofuels Production (Thousand Barrels Per Day), <https://www.eia.gov/cfapps/ipdbproject/IEDIndex3.cfm?tid=79andpid=79andaid=1>, last access 19th Nov 2015.
- Venugopal, R., Abraham, J., 2007. A numerical investigation of flame lift-off in diesel jets. *Combust Sci Technol*, 179(12), pp.2599-2618.
- Vishwanathan, G. and Reitz, R.D., 2008. *Numerical predictions of diesel flame lift-off length and soot distributions under low temperature combustion conditions* (No. 2008-01-1331). SAE Technical Paper.
- Vishwanathan, G. and Reitz, R.D., 2010. Development of a practical soot modeling approach and its application to low-temperature diesel combustion. *Combustion Science and Technology*, 182(8), pp.1050-1082.
- Wang, H., and Frenklach, M., 1994. Calculations of rate coefficients for the chemically activated reactions of acetylene with vinylic and aromatic radicals. *J. Phys. Chem.* 1994, 98, 11465-11489.

- Wang, H., Frenklach, M., Calculations of rate coefficients for the chemically activated reactions of acetylene with vinylic and aromatic radicals. *J. Phys. Chem.*, 98, 11465-11489.
- Wang, Y., Rutland, C.J., 2005. Effects of temperature and equivalence ratio on the ignition of n-heptane fuel spray in turbulent flow. *Proceedings of the Combustion Institute*, 30(1), pp.893-900.
- Wang, X., Huang, Z., Kuti, O.A., Zhang, W., Nishida, K., 2010. Experimental and analytical study on biodiesel and diesel spray characteristics under ultra-high injection pressure. *Int. J. Heat and Fluid Flow*, 31, 659-666.
- Westbrook, C.K., 2000. Chemical kinetics of hydrocarbon ignition in practical combustion systems. *Proceedings of the Combustion Institute*, 28(2), pp.1563-1577.
- Westbrook, C.K. and Dryer, F.L., 1984. Chemical kinetic modeling of hydrocarbon combustion. *Progress in Energy and Combustion Science*, 10(1), pp.1-57.
- Westbrook, C.K., Naik, C.V., Herbinet, O., Pitz, W.J., Mehl, M., Sarathy, S.M. and Curran, H.J., 2011. Detailed chemical kinetic reaction mechanisms for soy and rapeseed biodiesel fuels. *Combustion and Flame*, 158(4), pp.742-755.
- Westbrook, C.K., Pitz, W.J., Herbinet, O., Curran, H.J. and Silke, E.J., 2009. A comprehensive detailed chemical kinetic reaction mechanism for combustion of n-alkane hydrocarbons from n-octane to n-hexadecane. *Combustion and Flame*, 156(1), pp.181-199.
- White, E., Fell, M., Smith, L. and Keep, M., 2014. Shale gas and fracking. *Parliamentary Briefing, London: The Stationary Office*, 201.
- Williams, F. A. (1985). *Combustion Theory*. Benjamin/Cummings Publishing Co., Menlo Park, CA.
- Wu, Y., Huang, R., Lee, C.F., Huang, C., 2011. Effects of the exhaust gas recirculation rate and ambient gas temperature on the spray and combustion characteristics of soybean biodiesel and diesel. *Proc. Inst. Mech. Eng: Part D*, 226,372-384.
- Xu, F., Sunderland, P.B. and Faeth, G.M., 1997. Soot formation in laminar premixed ethylene/air flames at atmospheric pressure. *Combustion and Flame*, 108(4), pp.471-493.
- Yang, C.Y., Fang, Z., Li, B. and Long, Y.F., 2012. Review and prospects of Jatropha biodiesel industry in China. *Renewable and Sustainable Energy Reviews*, 16(4), pp.2178-2190.
- Yen M, Abraham J. Soot and nitric oxide modeling in reacting diesel jets with an unsteady flamelet progress variable model. *Proc Inst Auto Engineers: Part D* 2015; doi:10.1177/0954407015587404.
- Yen, M., and Abraham, J. (2014). Computations of Soot and NO in Lifted Flames under Diesel Conditions. *SAE Technical Paper*, 2014-02-11. doi:10.4271/2014-01-1128.
- Yoshihara, Y., Kazakov, A., Wang, H. and Frenklach, M., 1994, December. Reduced mechanism of soot formation—Application to natural gas-fueled diesel combustion. In *Symposium (International) on Combustion* (Vol. 25, No. 1, pp. 941-948). Elsevier.

Yuan W., Hansen, A.C., Zhang, Q., 2003. Predicting the physical properties of biodiesel for combustion modelling. *American Society of Agricultural Engineers*. 46(6), 1487-1493.

Yuan W., Hansen, A.C., Zhang, Q., 2005. Vapor pressure and normal boiling point predictions for pure methyl esters and biodiesel fuels. *Fuel*. 84, 943-950.

Zeldovich, Y.B., 1946. The oxidation of nitrogen in combustion and explosions. *Acta Physicochim. URSS*, 21(4), pp.577-628.

Zhang, J., Fang, T., 2011. Spray combustion of biodiesel and diesel in a constant volume combustion chamber. *SAE Technical Paper*, 2011-01-1380.

Zhang, S., Broadbelt, L.J., Androulakis, I.P. and Ierapetritou, M.G., 2012. Comparison of biodiesel performance based on HCCI engine simulation using detailed mechanism with on-the-fly reduction. *Energy and Fuels*, 26(2), pp.976-983.

Appendix A: Combustion Characteristics of Surrogate Fuels

Some of the important combustion characteristics of the surrogate fuels will be presented below. These include the adiabatic flame temperature (T_{ad}), laminar flame speed (S_L), as well as scalar dissipation rate (χ) at the limit phenomena of ignition (χ_{ign}) and extinction (χ_{ext}).

Adiabatic Flame Temperature

The adiabatic flame temperature (T_{ad}) is the temperature of the products of combustion when there is no heat loss in the reactor. The temperature can be defined at constant pressure for an open system and constant volume for a closed system. Its value depends on the initial temperature and composition of the reactants. Recall that n-heptane is the surrogate for petrodiesel and a tri-component blend of n-heptane, methyl deaconate, and methyl decenoate (TBS) is the surrogate for biodiesel. Table A.1 shows the T_{ad} of n-heptane, and two TBS oxidation mechanisms at 1 atm and an initial temperature of 298 K. The n-heptane simulation is run with the 160-species n-mechanism. The n-heptane adiabatic flame temperature is close to the values of a previous study (Hoffman and Abraham, 2009). The adiabatic flame temperature of TBS 115 is generally higher than that of n-heptane at all ϕ , except for $\phi = 1$. The temperature of the TBS211 is lower by up to 17 K relative to TBS115 for ϕ of 1.5 or lower but has the same value for higher ϕ . The differences between the surrogates are, however, within 23 K for the range of ϕ considered. Figure A.1 shows the T_{ad} plotted as a function of ϕ for the surrogates, showing both mechanisms for TBS. The figure emphasizes the point that the T_{ad} for the two surrogates are close to each other. Conditions representative of compression-ignition engines will now be considered. Table A.2 shows the T_{ad} at 42 atm and initial temperature of 1000 K. Considering the two TBS mechanisms, the TBS211 mechanism predicts slightly lower temperature than the TBS115 mechanism. The differences in temperature between the surrogates are within 31 K. Figure A.2 shows the T_{ad} plotted as a function of ϕ . The differences are noticeable but small.

Table A.1: Adiabatic flame temperature (K) at 1 atm for reactant temperature of 298 K.

ϕ	Heptane 160	TBS 115	TBS 211
0.5	1855	1862	1852
1	2658	2654	2637
1.5	2428	2434	2433
2	2036	2047	2047

2.5	1678	1696	1696
3	1354	1377	1377

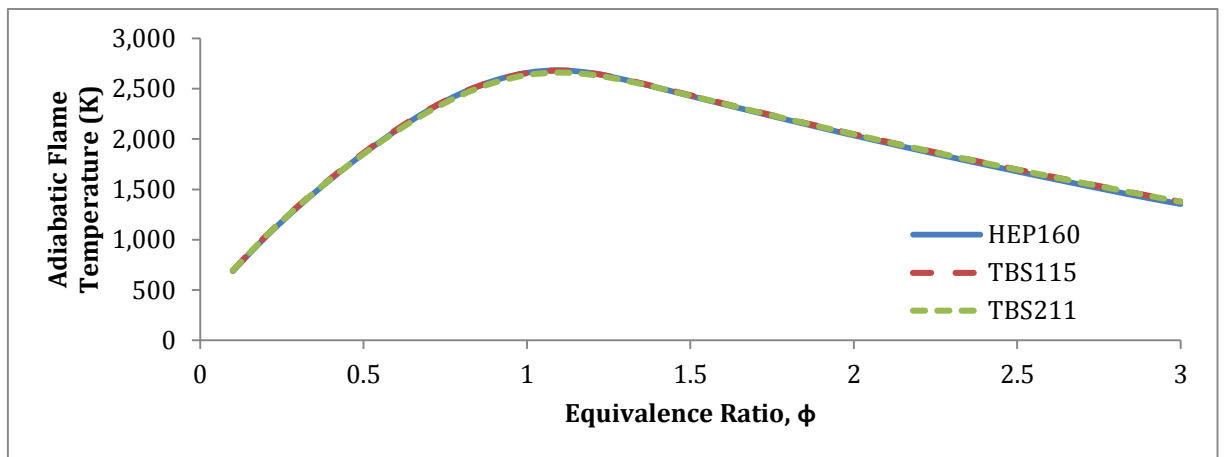


Figure A.1: Adiabatic flame temperature (K) at 1 atm and initial temperature of 298 K.

Table A.2: Adiabatic flame temperature (K) at 40 atm for reactant temperature of 1000 K.

EQ	Heptane 160	TBS 115	TBS 211
0.5	2104	2082	2371
1	2774	2751	3071
1.5	2546	2578	2957
2	2266	2299	2615
2.5	2056	2089	2293
3	1911	1920	2003

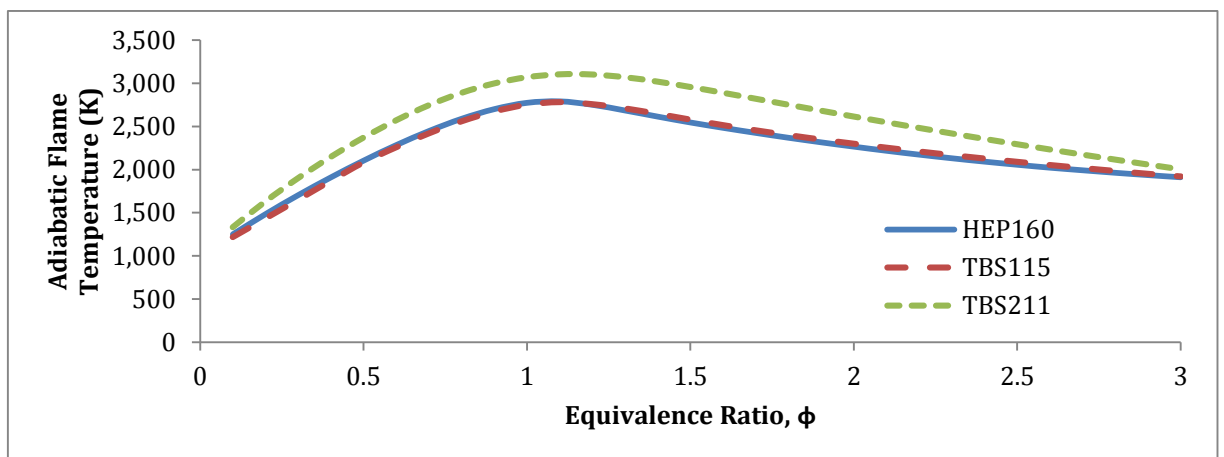


Figure A.2: Adiabatic flame temperature (K) at 40 atm and initial temperature of 1000 K.

Laminar Flame Speed

Temperature rise in a premixed flame occurs through a preheat zone where the rise is on account of heat diffusion from the hotter region of the flame and chemical reactions are slow,

and the reaction zone where chemical reactions are fast resulting in the generation of heat and rise in temperature. The classical understanding is that as the temperature rises with distance in the preheat zone, an ignition temperature is reached and chemical reactions accelerate. The speed at which unburnt gases flow into flame front in the normal direction is defined as the laminar flame speed (S_L) (Heywood, 1988). The S_L is a property of the fuel and is related to the flame thickness (δ_L), mean thermal conductivity (k) and specific heat at constant pressure (\bar{c}_p) as:

$$S_L = \frac{4.6\bar{k}}{\bar{c}_p \rho_u \delta_{L,ph}}, \quad (\text{A.1})$$

Figure A.3 shows the S_L of n-heptane and TBS at 1 atm and 298 K with respect to ϕ . The S_L increases with ϕ and peaks at an ϕ of just above unity before it decreases again. This is expected as the adiabatic flame temperature peaks just above unity as well. It can be clearly seen that the S_L of n-heptane is higher than TBS.

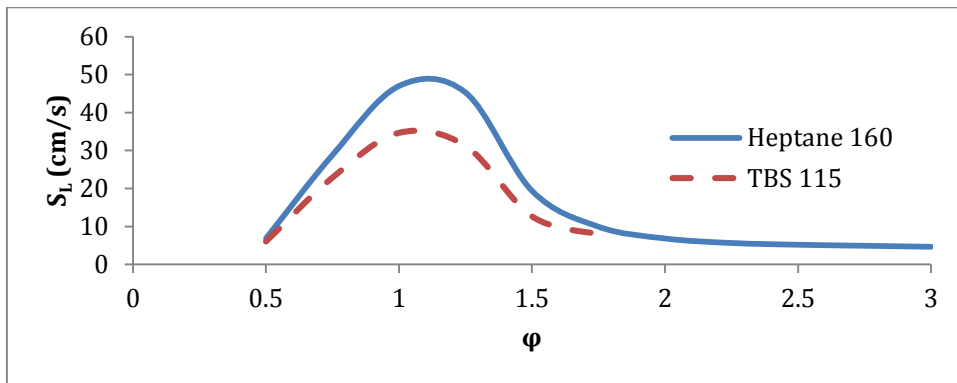


Figure A.3: S_L (cm/s) of the diesel and biodiesel fuel surrogates with respect to ϕ at 1 atm and initial temperature of 298 K.

Figure A.4 shows the S_L with respect to ϕ at engine conditions of 42 atm and 1000 K. The laminar flame speed increases with ϕ steadily from about 200 cm/s at $\phi = 0.5$ to around 1000 cm/s at $\phi = 3$ for n-heptane. The TBS speed is greater than the n-heptane speed by about 100 cm/s. These results may appear surprising at first, but they reflect the fact that under these conditions, n-heptane and TBS auto-ignite. The tendency for auto-ignition is greater at higher values of ϕ (Mukhopadhyay and Abraham, 2011). As a result of this tendency, the speed that is shown in Fig. 8 is most likely that of an ignition front rather than of a flame front. This influence is likely to exist even at the conditions of 1 atm and 298 K where auto-ignition in the preheat zone may increase the flame speed for one fuel more than another. This suggests that flame speed may not be an appropriate property to characterise these fuels. Instead, adiabatic flame temperature, ignition delay, and ignition and extinction strain rates are more appropriate.

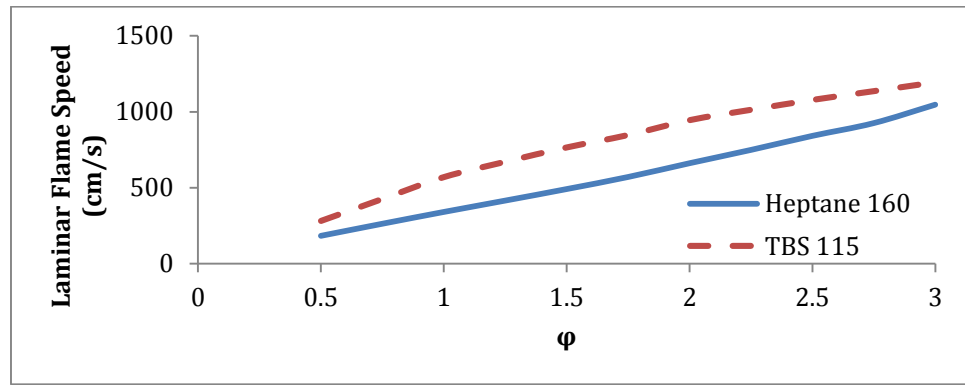


Figure A.4. S_L (cm/s) of the diesel and biodiesel fuel surrogates with respect to ϕ at 40 atm and initial temperature of 1000 K.

Appendix B: Extra Species in the 304-Species TBS Mechanism

The following are the extra species added to the 115-species TBS mechanism (Luo et al., 2012) from the 160-species n-heptane mechanism (Seiser et al., 2000) that also appear in the detailed TBS biodiesel mechanism (Herbinet et al., 2010).

CH₂OH C₂H PC₂H₄OH CH₃CO CH₃CHO C₃H₅-S C₃H₄-P
C₃H₄-A CH₃CHCO C₃H₅-T IC₃H₇ C₃H₈ C₅H₉-11 C₄H₇ SC₄H₉
CH₃COCH₃ C₂H₅CO C₅H₁₀-1 C₅H₁₁-1 C₅H₁₁-2 C₂H₅O C₃H₆O₁-2
C₂H₄O₂H C₃H₆O_{OH}1-2 C₃H₆O_{OH}2-1 NC₃H₇O IC₃H₇O CH₂(S)
IC₃H₇O₂ C₂H₅O₂ C₄H₇O C₄H₈O_{OH}1-3O₂ C₄H₈O_{OH}1-3
NC₄KET13 C₄H₈O_{OH}1-2 C₄H₈O₁-3 PC₄H₉O₂ C₃H₃ HOCHO C₃H₂
NC₃H₇CHO NC₃H₇CO C₃H₆CHO-2 C₂H₃O CH₂CH₂COCH₃ NC₃H₇COCH₂
NC₄H₉CHO NC₄H₉CO HOCH₂O C₆H₁₃-1 C₇H₁₅-1 C₇H₁₅-3 C₇H₁₅-4
C₇H₁₄-1 C₇H₁₄-2 C₇H₁₄-3 C₇H₁₃ C₇H₁₅O₂-1 C₇H₁₅O₂-3
C₇H₁₅O₂-4 C₇H₁₄O_{OH}1-2 C₇H₁₄O_{OH}1-3 C₇H₁₄O_{OH}1-4
C₇H₁₄O_{OH}2-3 C₇H₁₄O_{OH}2-5 C₇H₁₄O_{OH}3-1 C₇H₁₄O_{OH}3-2
C₇H₁₄O_{OH}3-4 C₇H₁₄O_{OH}3-5 C₇H₁₄O_{OH}3-6 C₇H₁₄O_{OH}4-2
C₇H₁₄O_{OH}4-3 C₇H₁₅O-1 C₇H₁₅O-2 C₇H₁₅O-3 C₇H₁₅O₂H-3
C₇H₁₄O_{OH}1-3O₂ C₇H₁₄O_{OH}2-3O₂ C₇H₁₄O_{OH}2-5O₂
C₇H₁₄O_{OH}3-1O₂ C₇H₁₄O_{OH}3-2O₂ C₇H₁₄O_{OH}3-4O₂ C₇H₁₄O_{OH}3-5O₂
C₇H₁₄O_{OH}4-2O₂ C₇H₁₄O_{OH}4-3O₂ NC₇KET23
NC₇KET25 NC₇KET43 NC₇KET34 NC₇KET35 NC₇KET36 NC₇KET42
C₇H₁₄O_{OH}3-6O₂ NC₇KET31 NC₇KET32 NC₇KET13

Biography

Gary Cai was born in Pontiac, MI, USA on the 17th May, 1988. He graduated from Jurong Junior College, Singapore, in 2006. He attended the University of Adelaide from July 2007 to December 2011. Initially starting in a Bachelor of Science degree, he switched to Bachelor of Mechanical Engineering after one semester, in Jan 2008. His internship at Dadanco Pty Ltd with Mr. Yi Li inspired him to pursue the track of computational fluid dynamics. Introduced by Dr. Zhao Tian, he joined the post-graduate research program at the University of Adelaide, supervised by Prof. John Abraham, Prof. Bassam Dally, Dr. Zhao Tian, and Dr. Emmanuel Motheau. Working with Prof. Abraham in the study of biodiesel combustion, he has authored four journal publications and three conference papers. He has also held a tutoring position at the School of Mechanical Engineering, teaching CFD from Jan 2013 to Dec 2015.

He and Chengyu Chang have been happily married since June 2014.

List of Publications

Journal

Cai G, Abraham J. A Comparison of Biodiesel Feedstocks and their Effect on Soot Emissions. *Renewable Energy*; submitted, Dec 2015, under review.

Cai G, Abraham J. Multidimensional Simulations of Non-Reacting and Reacting Petrodiesel and Biodiesel Jets. *Energy*; submitted, Dec 2015, under review.

Cai G, Yen M, Abraham J. Predictions of Soot in Reacting Diesel Sprays with semi-empirical and kinetic models. *Proc. IMechE Part D: J. Auto Eng*; submitted, Nov 2015, under review.

Cai G, Abraham J. On formulating a simplified soot model for diesel and biodiesel combustion. *Chem Engineering Sci*; accepted for publication, doi:10.1016/j.ces.2016.01.039.

Conference

Cai G, Abraham J. Toward developing simplified models for diesel/biodiesel engine pollutant emissions. In: *IEEE 9th Conference on ICIEA*, 9 – 11 June 2014, Hangzhou, China.

Cai G, Abraham J. Simulation of Biodiesel and Petrodiesel Pollutant Kinetics. In: *29th Int Congress on Modelling and Simulation*, Adelaide, Australia, 1 – 6 December, 2013.

Cai G, Abraham J. Reaction Pathways to Soot Formation in Petrodiesel and Biodiesel Combustion. In: *Proc Australian Combustion Symposium*, Perth, WA, 6 – 8 November, 2013.